Development of High Performance RE-Fe-B Hot-deformed Magnets

Xin Tang

February 2018

Development of High Performance RE-Fe-B Hot-deformed Magnets

Xin Tang
Doctoral Program in Materials Science and Engineering

Submitted to the Graduate School of
Pure and Applied Sciences
in Partial Fulfillment of the Requirements
for the Degree of Doctor of Philosophy in
Engineering

at the
University of Tsukuba

Contents

Chapter 1: Introduction

1.1 General introduction

Permanent Magnets have wide application in renewable energy technologies, such as wind turbines, hydroelectric power generators and traction motors [1,2].

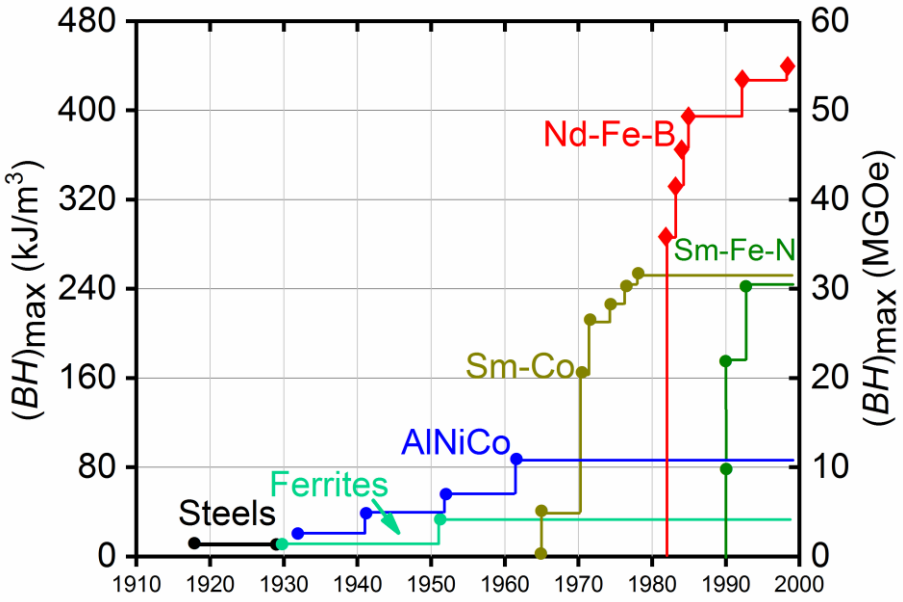

Fig. 1 The development in energy density of permanent magnets in 20th century [1].

Fig. 1 shows the development in energy density of permanent in 20th century. It is seen that the first magnetic materials is martensitic steel with the coercivity smaller than 16 kA/m and maximum energy product smaller than 8 kJ/m^3, which was replaced by AlNiCo in 1950. Because of its good thermal stability, AlNiCo now still occupies 1% in world market [1]. Hereafter, the invention of $CaCu_5$-type $SmCo_5$ magnetic powders with $(BH)_{max}$= 40 KJ/m^3 reported by K. J. Strnat *et al* [3,4], remarked as first-generation rare earth (RE)-based magnet. By tuning the atomic ratio between Sm and Co, Sm_2Co_{17}-type magnet with super high magnetocrystalline anisotropy filed was invented. Further optimization of composition in Sm-Co-based magnet, a $(BH)_{max}$=238.8 kJ/m^3 can be achieved in $Sm(Co,Cu,Fe,Zr)_{7.2}$ [5,6], remarked as second-generation permanent

magnets. In 1983, J. Croat and M. Sagawa [7,8] independently reported $Nd_2Fe_{14}B$-based magnets processed by powder metallurgy with high energy density (286.6 kJ/m^3), remarked as third-generation RE-based permanent magnets. Since its highest energy density and rapid development of efficient energy technologies, the demand for Nd-Fe-B magnets have been rapidly increasing, which makes Nd-Fe-B magnet become a dominant product in the market of permanent magnet, capturing 62 % market share in 2010 [1].

1.2 RE-Fe-B-type permanent magnets

1.2.1 Crystal structure and intrinsic properties of RE-Fe-B permanent magnet

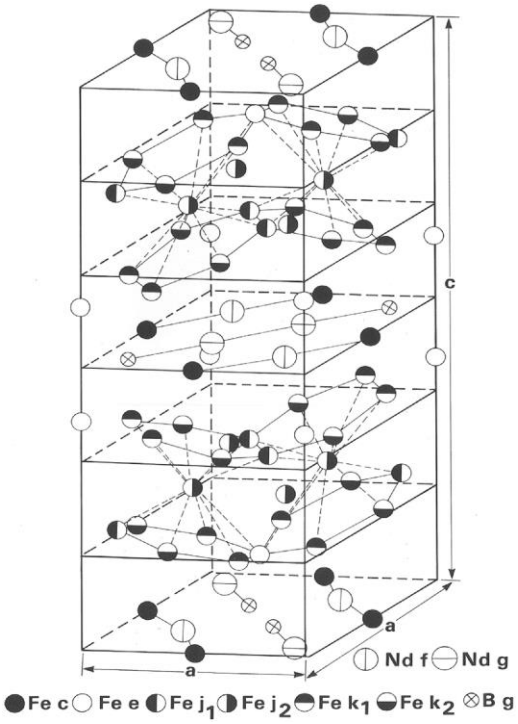

Fig. 2 Unit cell of $Nd_2Fe_{14}B$ [9].

To develop high performance Nd-Fe-B magnets, magnetism and crystal structure must be fully understood. $Nd_2Fe_{14}B$ adopts tetragonal structure (*P4$_2$/mnm*) a=0.882 nm, c=1.224 nm. As shown in Fig. 2 [9], one unit cell of $Nd_2Fe_{14}B$ has 68 atoms. Specifically, 8 Nd atoms occupy 4f and 4g sites while 56 Fe atoms occupy 16k$_1$、16k$_2$、8j$_1$、8j$_2$、4e and 4c sites and 4 B atom seats in 4g site. The intrinsic properties, such as anisotropy field, saturation magnetization and Curie temperature are determined by crystal structure of Nd-Fe-B.

Due to the asymmetric distribution of atoms, Nd-Fe-B has a large anisotropy field. The anisotropy field ($\mu_0 H_A$) is measured to be ~ 6.7 T at room temperature. The moment of Fe atoms mainly contributes to saturation magnetization ($\mu_0 M_s$) of $Nd_2Fe_{14}B$, which is determined to be ~ 1.61 T at room temperature. While the Curie temperature is strongly depended on the exchange interaction of moments between Fe and Fe, which is measured to be ~ 585 K.

1.2.2 Extrinsic properties of RE-Fe-B permanent magnets

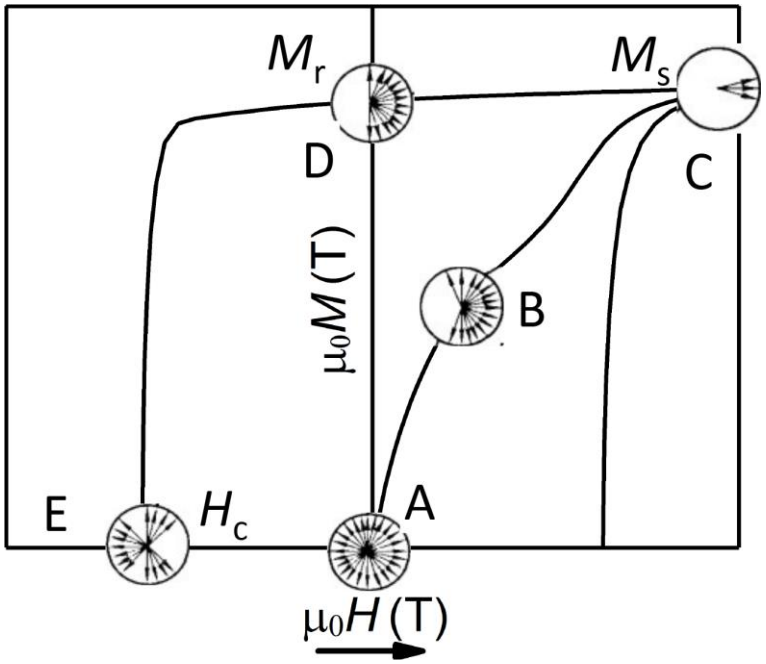

Fig. 3 Magnetization at different stages in an external field.

By testing a piece of RE-Fe-B magnet in magnetic field, a hysteresis loop can be obtained as shown in Fig. 3. In the demagnetization state (A), all the moments are randomly distributed and 0 net magnetization can be obtained in this stage. With increasing external field, the moments are gradually aligned with same direction of magnetic filed until saturation (C). Hereafter, the remanent magnetization state (D) can be achieved with decreasing field to 0. Further applying the reverse field, the magnet will be demagnetized at point E. Here, there are three important values on this hysteresis loop, coercivity (H_c), remanent magnetization (M_r), and maximum energy product, $(BH)_{max}$. Specifically, the value of point D shows the remanent magnetization (M_r), which was the magnetization in a sample after an external magnetic field is removed. The remanent

magnetization is depended on saturation magnetization, volume fraction of magnetic phase and degree of grain alignment.

Further reducing the field, when the magnetization of sample equals 0, the value of external field (point E) defined as coerciviy, which shows the ability of sample resist demagnetization. The coercivity is influenced by anisotropy field, chemical composition in grain boundary phase and grain size and aspect ratio of grains.

The $(BH)_{max}$ is calculated from BH curves, where B=(H+M). Maximizing the value of B× H under the second quadrant of BH curves. It shows the how large the energy density the magnet can generate. Theoretical value of $(BH)_{max}$ is determined by the following equation:

$$(BH)_m = \frac{1}{4}(\mu_0 M_s)^2$$

This value is larger than experimental value because that B_r is smaller than $\mu_0 M_s$. The value of $(BH)_{max}$ is widely applied to denote grade. For example, a grade 48 Nd-Fe-B magnet generally has a $(BH)_{max}$ of 48 MGOe.

1.2.3 Processing routes of anisotropic RE-Fe-B permanent magnets

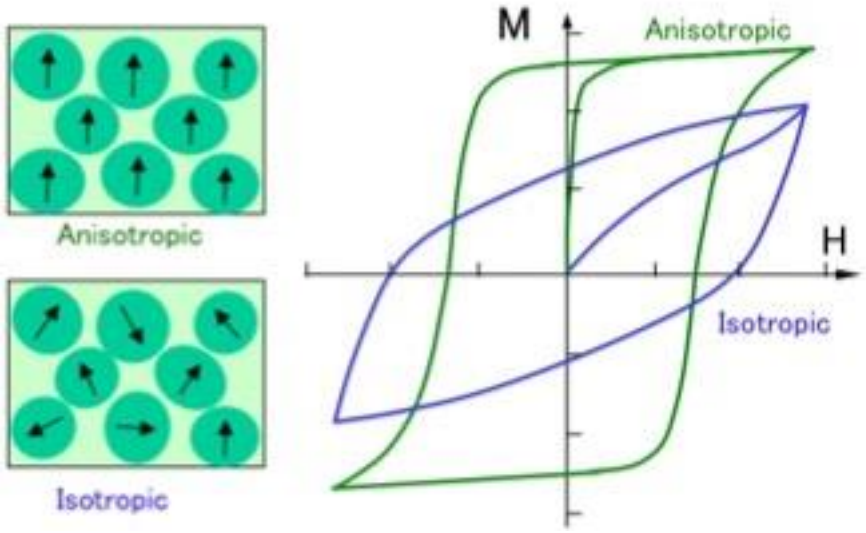

Fig. 4 Schematic of isotropic and anisotropic magnets. Courtesy by K. Hono.

As shown in Fig. 4, depending on degree of alignment of grains, the magnets are generally divided into two groups: isotropic and anisotropic magnets. In general, higher remanent magnetization and $(BH)_{max}$ can be obtained in anisotropic magnets than those in isotropic magnets.

One type of commercial isotropic magnets is bonded Nd-Fe-B magnets produced by bonding melt-spun powders and polymer, whereas there are two commercial types of anisotropic magnet available on market: hot-deformed and sintered magnets.

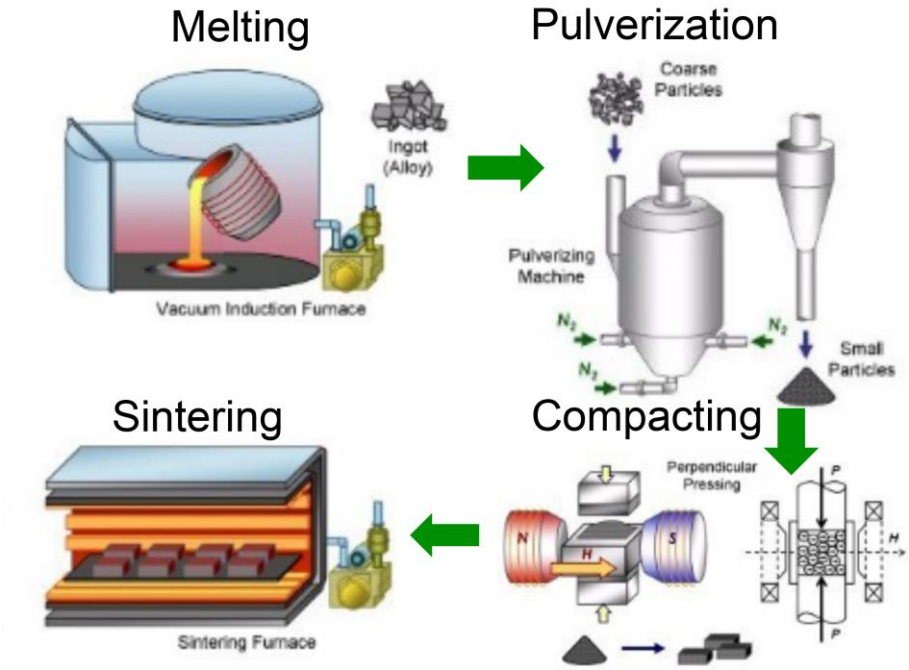

Fig. 5 Schematic of sintering process of Nd-Fe-B magnets [10].

The processing route for sintering magnet is shown in Fig. 5 [10]. It consists of 4 steps, such as melting, pulverization, compaction, and sintering. Specifically, the strip cast alloy is obtained firstly by melting raw alloys or elements at 1400 °C and casting on Cu wheel at 4-5 m/s. Hereafter, the strip cast alloys is subjected to hydrogen decrepitation followed by jet milling under protection of Ar or N_2. The single-grained size Nd-Fe-B particles with 2-5 μm are obtained. Then the as-milled Nd-Fe-B particles are aligned under 2-5 T to get anisotropic green compact. Subsequently, the green compacts are sintering at above 1000 °C for 2-10 hours, to get anisotropic sintered magnet with full density.

In contrast, it is seen in fig. 6 fabrication of anisotropic hot-deformed magnets mainly comprises of induction melting, melt-spinning, hot-pressing and hot-deformation. In specific, alloy ingots are produced by induction melting high-purity constituent elements and casting to low carbon steel book mold. The ingots are subjected to melt-spinning at a wheel speed of 20-40 m/s under Ar protection to obtain amorphous or nanocrystalline melt-spun ribbon. Hereafter, the

magnetic powders with small particle size are obtained from crushing melt-spun ribbons and the powders are compacted with 300-400 MPa at 600-650 °C in vacuum to obtain the hot-pressed magnets with ~98% of full density, followed by deformation at 700-850°C until 70-80% height reduction is achieved. During the hot-deformation, the isotropic magnets are developed into anisotropic magnets by grain boundary sliding, grain rotation and preferential growth under uniaxial pressure [11–15].

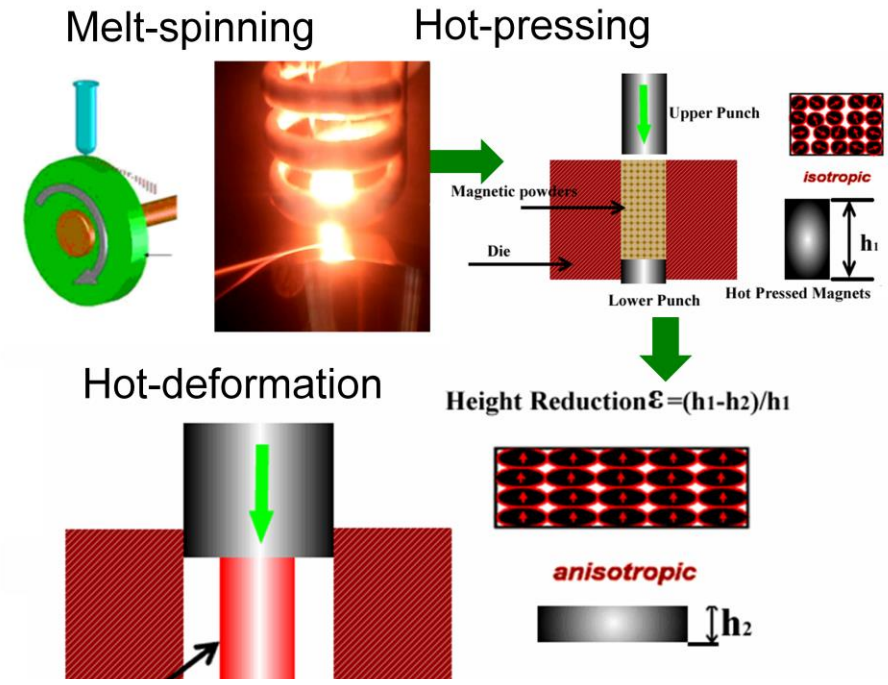

Fig. 6 Schematic of processing Nd-Fe-B hot-deformed magnets.

Fig. 7 [16,17] shows the typical microstructure of sintered and hot-deformed magnet. It is seen that grain size in sintered magnets varies from 2 to 5 μm. In comparison, the grain size (~400 nm) in hot-deformed magnets is much smaller than that of sintered magnets. Note that single domain size of the $Nd_2Fe_{14}B$ phase is ~260 nm, which is comparable with the grain size of hot-deformed magnets. Hence, in comparison with sintered magnets, the hot-deformed magnets are believed to have greater potential to achieve higher coercivity, which recommends hot-deformed magnets as a promising candidate for the development of high-coercivity Dy-free Nd-Fe-B permanent magnets. In this thesis, hot-deformation processing route is employed to produce anisotropic magnets because of their greater potential to achieve higher coercivity in hot-deformed magnets.

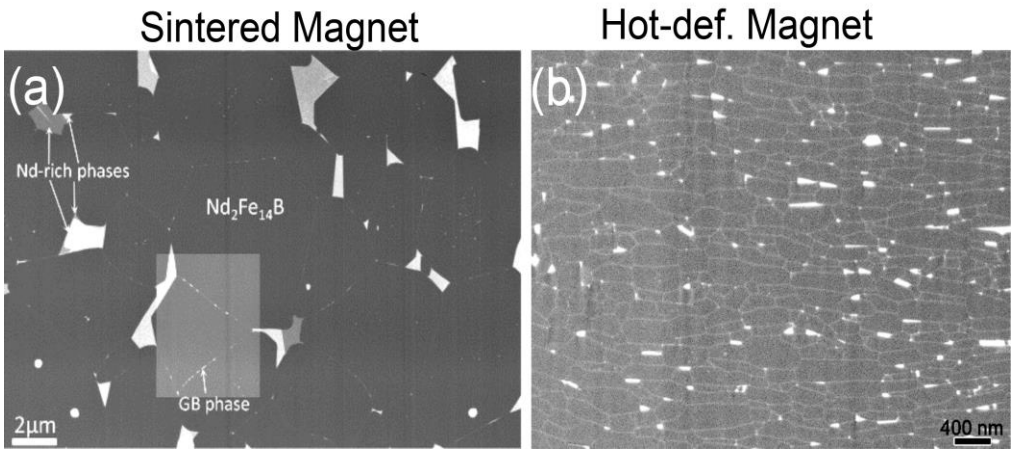

Fig. 7 Microstructures of (a) sintered and (b) hot-deformed magnets [16-17].

1.3 Coercivity mechanism in RE-Fe-B permanent magnets

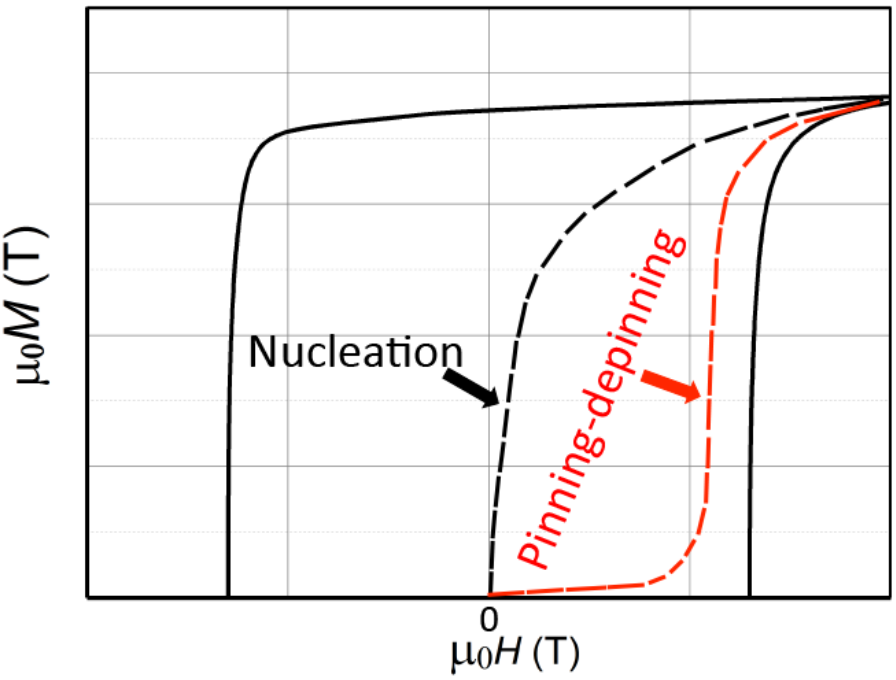

Fig. 8 Schematic of two kinds of coercivity mechanism in RE-based magnets.

To improve the coercivity of RE-Fe-B permanent magnet, mechanism of coercivity in permanent magnets should be well understood. The external field required to demagnetize a piece of magnet is defined as coercivity. In general, the magnetization reversal takes place as follow: the reversed magnetic domains is nucleated at sites with lowered magnetic anisotropy field, such as defects, followed by propagation of reversed magnetic domain with help of inverse magnetic field. Because of imhomogeneity in magnets, the propagation of reversed magnetic domains would be pinned at imhomogeneous sites (such as grain boundaries). Further increase in inverse external field leads to overcome the pinning energy caused by the imhomogeneities. Once depinning occurs, reversed magnetic domains propagate through whole magnet. Hence, the mechanism of coercivity is divided into two types: nucleation type and pinning-depinning type.

The coercivity can be phenomenologically expressed by

$$H_c = \frac{2K_1}{\mu_0 M_s}\alpha_k\alpha_\varphi - N_{\text{eff}}M_s \quad (1)$$

where K_1 and M_s are first-order magnetocrystalline anisotropy constants and saturation magnetization, α_k and α_ψ show the lowered anisotropy field resulted from defects (its type and dimension) and effect of angular dependence of the coercivity, and N_{eff} describe the effective demagnetizing factor [18]. When width of defect, d, is much smaller than domain wall width δ, the defect with minimum anisotropy field becomes the nucleation site and the magnetization reversal process is governed by nucleation; whereas, when width of defect, d, is comparable with domain wall width δ, domain walls propagate through the entire sample come across with different pinning sites, the site giving strongest pinning force determines the coercivity of the magnets. In this case, the magnetization reversal process is dominated by pinning-depinning process[18–20]. According to the description above, there should be some difference in susceptibilities of initial curves between these two types of coecivity mechanism-governed magnets. For nucleation-governed initial curve, the susceptibility is higher at the beginning and magnetization is gradually saturated with increasing external magnetic field, as shown in Fig. 8. In contrast, the susceptibility in initial magnetization curve is quite low in the pining-depinning model, because of magnetic domain wall pinned by defects. After increasing field to depinning field, the susceptibility increases dramatically and the magnetization further increases to saturation magnetization with increasing magnetic field as shown in Fig. 8. These two types of initial curves can be evidenced in magnetization measurements in sintered Nd-Fe-B magnets and Sm-Co-based magne, respectively,

indicating that coercivity mechanism of sintered Nd-Fe-B magnet is governed by nucleation while the magnetization reversal process in Sm-Co-based is dominated by pinning-depinning process.

In the other words, to improve the coercivity in RE-based permanent magnets, it is necessary to remove the nucleation sites with lowered anisotropy field and strengthen the pinning force against reversed magnetic domain displacement in grain boundaries.

1.3.1 Influences of size and aspect ratio of grains and chemical composition in grain boundary phases on coercivity in Nd-Fe-B permanent magnets

The coercivity, as extrinsic property, is sensitive to microstructure, such as size and aspect ratio of grains and chemical compositions in grain boundaries.

1, Effects of size and aspect ratio of grains on coercivity

Grain size reduction is one well-known method to improve the coercivity in sintered magnet. From Fig. 9 [16], one can see that with reduction in grain size, the coercivity is increased with some deviations. In general, the underlying coercivity mechanism in sintered Nd-Fe-B-type magnets is governed by nucleation. Specifically, the facile domain wall displacement within multi-domain sized grains gives rise to initial high susceptibility and no pining force can be obtained in sintered magnets with multi-domain sized grains. When grain size is refined to comparable size of single domain, the domain wall is located and pinned at the grain boundaries to enhance the coercivity, this can be experimentally confirmed [21]. The grain size in sintered magnets is heavily depended on the particle size produced by jet milling. Numerous works has done to achieve higher coercivity by reducing grain size [22–24]. However, it is technically difficult to reduce the grain size to 1 μm, because of less resistant to oxygen in smaller particles. Une *et al* [25] have successfully reduced grain size in sintered magnet by jet milling strip cast under protection of helium, with average grain size reducing from 3 μm to 1 μm, the coercivity is enhanced from 1.5 T to 1.9 T. The other method to reduce grain size is trace additions of high melting temperature transition elements such as Zr and Nb, which were reported to be effective additives for refining the grain size of melt-spun, HDDR-processed and sintered Nd-Fe-B alloys [26–30]. The high melting temperature transition element reacts with Fe and B and precipitates at grain boundaries, thus hindering grain boundary migration and refined grains are yielded in the additive-added sample. Consequently, the coercivity is enhanced. This grain size effect can be also demonstrated in hot-deformed magnet, Liu *et al* reported that the hot-deformed magnets with different grain size

can be obtained by hot-deformation at different temperatures, with reducing grain size from ~970 nm to ~210 nm, the coercivity can be enhanced from ~ 1.46 T to ~ 1.91 T [31].

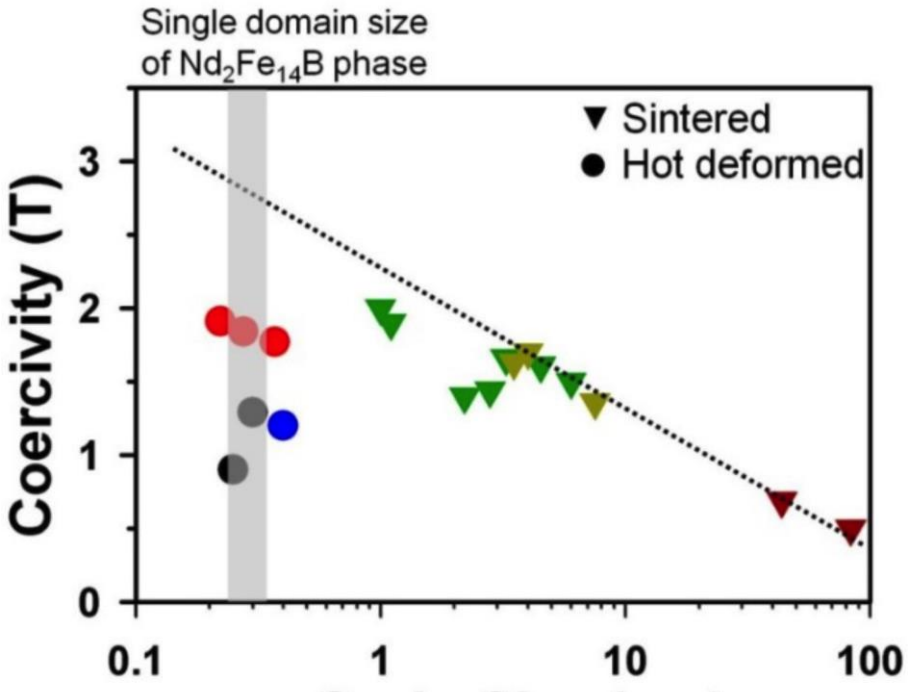

Fig. 9 Dependency of grain size on coercivity [16].

The coercivity can be phenomenologically expressed by $H_c(T)= \alpha H_A(T)-N_{eff}M_s(T)$; where H_A(T) and M_s(T) are the magnetocrystalline anisotropy field and saturation magnetization at various temperatures, α reflects the lowered anisotropy field resulted from defects near grain boundaries, and N_{eff} is the effective demagnetizing factor [32]. Smaller N_{eff} is beneficial to higher coercivity. To reduce the N_{eff}, reducing the aspect ratio of grains is one of approaches. For typical hot-deformed magnets, even grain size is much smaller than that of sintered magnet, the N_{eff} is as high as 0.75, one reason is that the grains are platelet-like shaped in hot-deformed magnet, the aspect ratio of grains in hot-deformed magnet as high as 3.5, responsible for low coercivity in as-deformed magnets. Note that aspect ratio of the grains is defined as ratio between size along the *c*-plane and the size perpendicular to the *c*-plane. Sepheri-Amin *et al* reported that the coercivity is enhanced with decreasing the aspect ratio of grains because of lower larger stray field [33].

Up to dates, it should be noted that all the hot-deformed magnets are processed from melt-spun powders. By optimization of processing and composition, it is possible to control the grain size in melt-spun precursors as well as hot-deformed magnets.

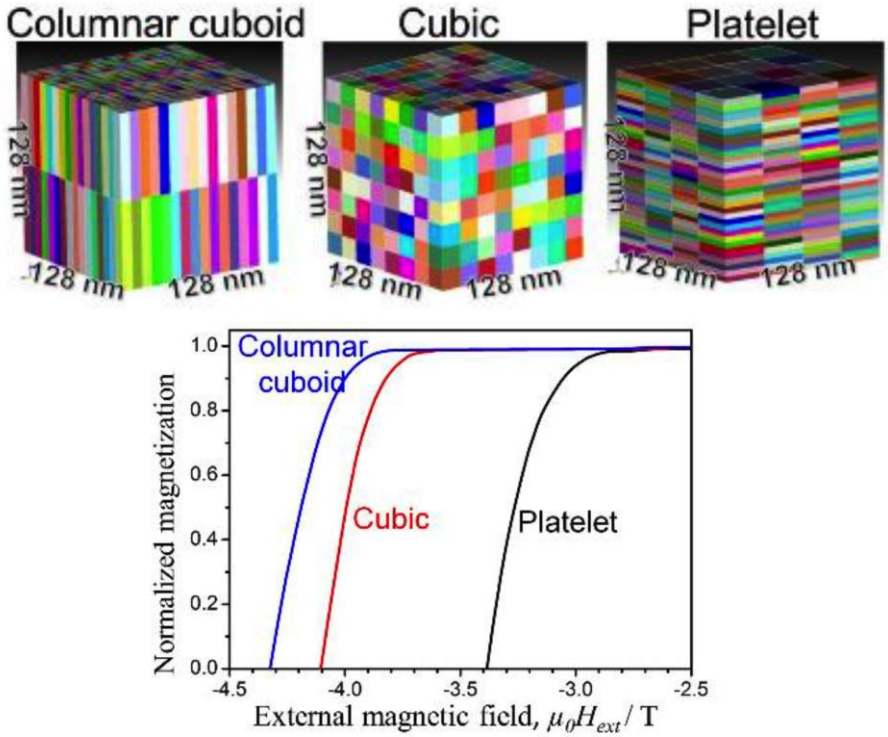

Fig. 10 Micromagnetic simulation of effect of grain shape on coercivity [33].

2, Effect of chemical composition in grain boundary phase on coercivity

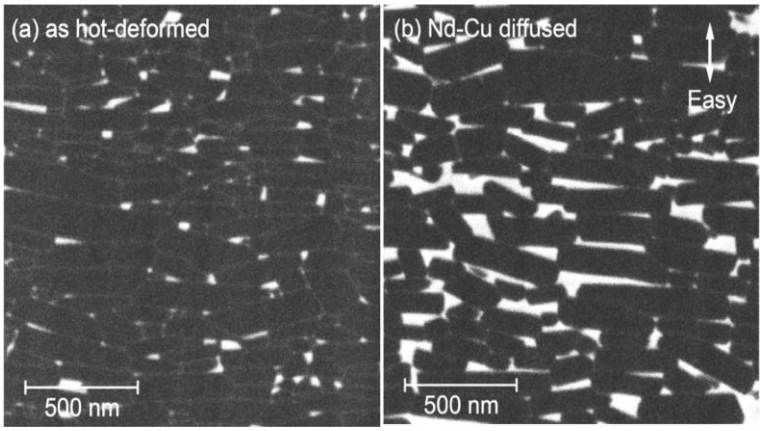

Fig. 11 Microstructures of as-deformed and diffusion-processed magnets [44].

The composition in grain boundary phase is another factor contributing to coercivity. Additions of Ga and Cu are reported to enhance the coercivity in sintered magnets, the enrichment

of Ga and Cu in grain boundary phase reduces melting-point of intergranular phases and improve the wettability of grain boundary phase.

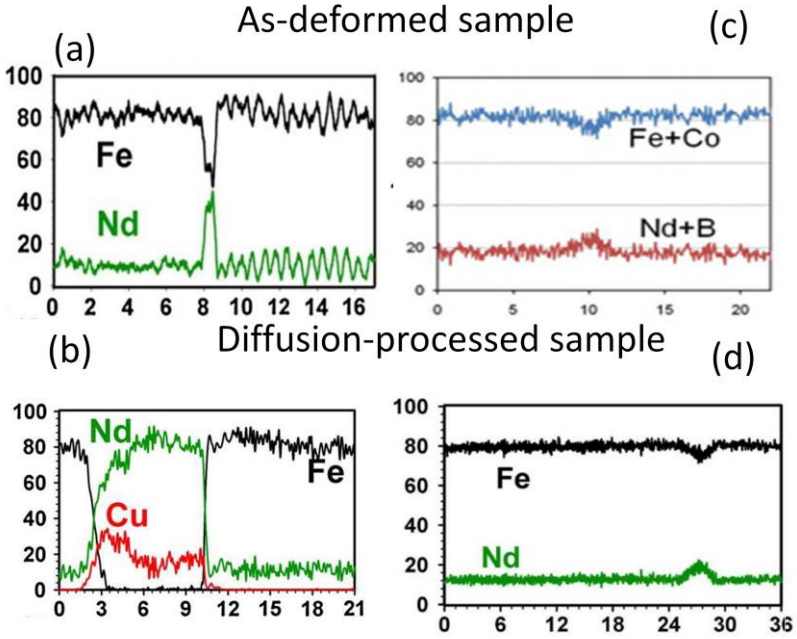

Fig. 12 Composition in grain boundary phase of *c*-plane (a) and side-plane (c) of as-deformed sample and *c*-plane (b) and side-plane (d) of diffusion-processed sample [36].

Recently, grain boundary infiltration of eutectic RE-based alloys with low melting point, which were proposed by Sepehri-Amin *et al* has widely applied to enhance the coercivity in HDDR, nanocomposite, sintered and hot-deformed magnets [34–43]. Fig. 11 [44] shows changes in microstructure after grain boundary diffusion in one example of grain boundary diffusion of Nd-Cu in hot-deformed Nd-Fe-B magnet. It is seen that volume fraction of Nd-rich phase increases and more misaligned grains can be observed. In the mean time, composition of grain boundary phases after grain boundary diffusion was changed. One can see that the composition of Fe is reduced significantly from 60 at.% to 0 at.% in the *c*-plane grain boundary phase after grain boundary diffusion of Nd-Cu, while composition in side-plane kept almost unchanged after grain boundary diffusion. Consequently, the grain boundary phase in *c* planes is transformed from ferromagnetic one to non-ferromagnetic one by dilution of concentration of Fe in grain boundary phase and the stronger pinning force against reversed magnetic domains as well as higher coercivity can be hence yielded. Besides, according to formula (1), by measuring the coercivities

at various temperatures, α and N_{eff} can be calculated by plotting H_c/M_s against H_A/M_s at different temperatures followed by fitting the data linearly. α was increased from 0.61 in as-deformed magnets to 0.69 in diffusion-processed magnets, while N_{eff} was reduced from 1.37 in hot-deformed magnet to 1.16 in diffusion-processed sample, indicating that the defects at grain boundary are suppressed and stray field is reduced by grain boundary engineering, leading to an enhancement of coercivity. However, the remanent magnetization was substantially reduced to ~1.1 T because of the larger volume fraction of RE-rich phases and the degradation of texture in diffusion processed hot-deformed magnets. To increase the remanent magnetization, Akiya *et al*. [44] proposed constrained expansion diffusion process to reduce the loss of remanent magnetization after eutectic alloys diffusion process, by which the coercivity can be increase to ~1.9 T while keeping remanence at ~1.35 T. Many multi-component eutectic alloys were employed to enhance the coercivity; however, coercivity enhancements were always accompanied by the reduction of remance [39,45,46]. To obtain high coercivity while keeping a reasonable remanence after grain boundary diffusion of eutectic alloys, it is necessary to produce the high remanence hot-deformed magnets with optimized microstructure.

1.4 Low cost Ce-containing hot-deformed magnets

In general, Nd-Fe-B- based magnets are comprised of ~30-33 wt.% of rare earth elements, such as Nd, Pr and Dy. With increasing demand on Nd-Fe-B-based magnets, the cost of Nd-Fe-B-based has been rising. To reduce the cost of Nd-Fe-B-based magnet, one approach is to replace Nd, Pr and Dy with light rare earth elements such as La, Ce or Y [47–59]. Fig. 13 [60] shows the abundance of rare earth elements in the earth crust. It is seen that La and Ce are most abundant elements in the family of rare earth elements except for Nd. Table 1 [61] shows the intrinsic properties of RE-Fe-B and cost of rare earth elements. For examples, the price of La is as low as 11 % of Nd. The intrinsic properties of $La_2Fe_{14}B$ are $\mu_0 M_s$=1.38 T and $\mu_0 H_A$ =2 T. Previous work [62] on La-Fe-B melt-spun ternary alloys showed that the hard magnetic $La_2Fe_{14}B$ (2:14:1) phase is difficult to obtain in the ternary alloy. The α-Fe and La-rich phases coexist in the melt-spun ribbons, with increasing Nd substitution for La, 2:14:1 phases gradually appears with suppression of secondary phases. However, with 40 % Nd substitution for La, the coercivity is as low as 0.12 T even in nanocrystalline melt-spun ribbons. Further first-principle study revealed that the substitution energies of La in 2:14:1 are positive (0.41 eV/atom), indicating that La tends to be

rejected from 2:14:1 phase to Nd-rich grain boundary phase [63]. A composition of $(La_{0.35}Ce_{0.65})_xFe_{14}B$ was used to study phase formation and magnetic properties in melt-spun ribbons, in the range of x from 2.0 to 4.0, the phases comprises of 2:14:1 phase and La-Ce-rich phase, the optimal coercivity was achieved to be 0.55 T for x=0.4 [52]. A. M. Gabay *et al* [64] attempted to produced hot-deformed magnets from La-Ce-Fe-B ribbons, no practically viable magnetic properties can be obtained in Nd-free alloys, further blending the Nd-La-Ce-Fe-B ribbons with Nd-Cu powders followed by hot-pressing and hot-deformation, even with 10 wt% addition of Nd-Cu, the coercivity can not be enhanced to above 1 T. It is preliminary conclusion that La substitution for Nd does not only lead to formation of the undesirable secondary phase but also result in degradation in intrinsic properties.

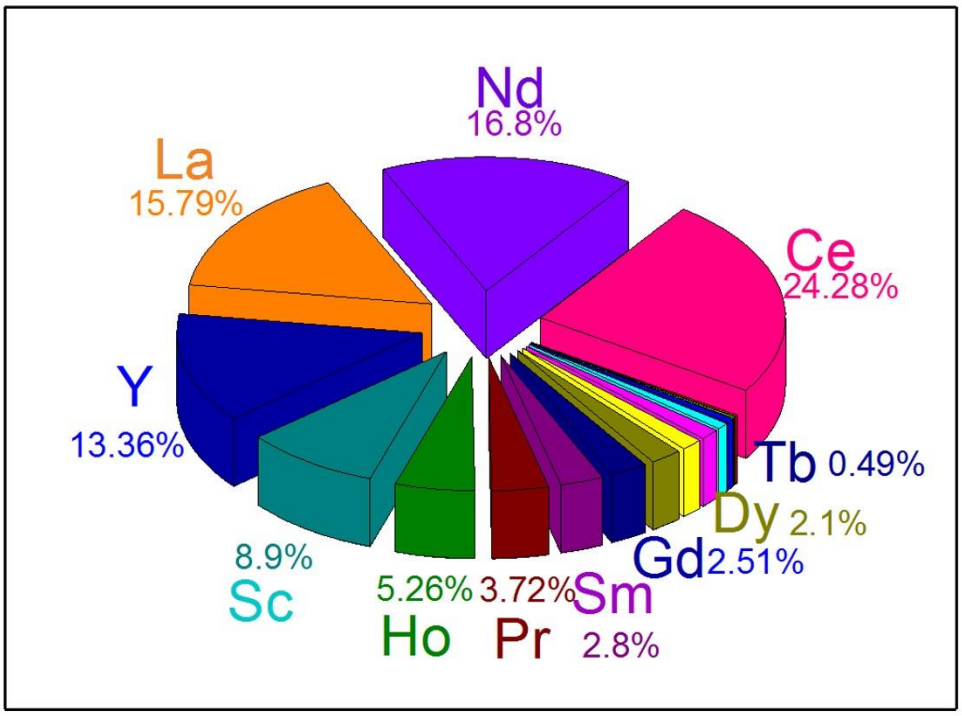

Fig. 13 The abundance of rare earth elements in earth crust [60].

In contrast, the price of Ce is as cheap as 12 % of Nd, which is comparable with La. The intrinsic hard magnetic properties of $Ce_2Fe_{14}B$, μ_0M_s=1.17 T and μ_0H_A =3 T [61]. The anisotropy field of Ce-Fe-B is higher than that of La-Fe-B. Yan *et al* [50] reported that the magnetic properties are degraded with increasing Ce substitution in $(Nd_{1-x}Ce_x)_2Fe_{14}B$ with a abnormal jump in coercivity for x=0.24. Hard magnetic properties of the Ce-substituted sintered magnet with x=0.25

were further optimized to ~$\mu_0 H_c$=1.21 T and $\mu_0 M_r$=1.33 T by using a two alloy method [56]. Apart from studies in Ce-substituted sintered magnets, there are considerable studies on optimization of melt-spun ribbon for hot-deformation. Pathak *et al* and Pei *et al* [51,65] reported that there is an abnormal jump in coercivity to around ~ 1 T in melt-spun ribbon of $(Nd_{1-x}Ce_x)_2Fe_{14}B$ for x= 0.25 accompanied by the formation of the $CeFe_2$ phase. By further optimizing the composition, coercivity of ~1.7 T was reported for melt-spun Ce-substituted isotropic ribbons; however, this value is deteriorated to ~0.94 T in hot-deformed anisotropic magnets. Further increase in x leads to a substantial reduction of coercivity [66], and only a very low coercivity of ~7 $\times 10^{-4}$ T was reported for hot-deformed Ce-Fe-B magnets, in which the 2:14:1 phase and $CeFe_2$ coexist. Given the relatively high anisotropy field of the $Ce_2Fe_{14}B$ phase (~3 T), the coercivity value reported for the hot-deformed Ce-Fe-B magnet is too low.

Table1. Intrinsic properties of $RE_2Fe_{14}B$ compounds at room temperature [61].

$RE_2Fe_{14}B$	J_s (T)	H_A (T)	T_c (°C)	Relative cost to Nd
$Nd_2Fe_{14}B$	1.61	6.7	310	100%
$La_2Fe_{14}B$	1.38	2	257	11%
$Ce_2Fe_{14}B$	1.17	3	149	12%
$Y_2Fe_{14}B$	1.41	2	298	79%

In summary, the price of La is comparable with that of Ce, while the anisotropy field of $Ce_2Fe_{14}B$ is superior to that of $La_2Fe_{14}B$. Moreover, the $La_2Fe_{14}B$ phase is very difficult to form, this is a barrier to use La to substitute Nd in 2:14:1 phase. Compared to La, Ce is much more promising to substitute Nd in 2:14:1 to achieve high performance magnet.

1.5 Fabrication of high performance Nd-Fe-B and low cost Ce-containing RE-Fe-B hot-deformed magnets

The coercivity of ~1.2 T with remanence of ~1.4 T is reported in a typical Nd-Fe-B sintered magnets, which is not large enough for the high temperature applications such as wind turbine and traction motors for (hybrid) electric vehicles. To be applicable at elevated operating temperature around 180°C, the coercivity of Nd-Fe-B sintered magnets is supposed to be around ~ 3.0 T at room temperature. One approach to increase the coercivity is to increase the anisotropy field in

2:14:1 phase by partial replacement of Nd with Dy due to the fact that $Dy_2Fe_{14}B$ has larger anisotropy field compared to $Nd_2Fe_{14}B$ [67]. However, because of anti-ferromagnetic coupling between Fe and Dy, the degradation in magnetization is inevitably caused in Dy-substituted Nd-Fe-B magnets. In addition, Dy is much scarcer in earth crust and the cost of Dy has been rising due to surging demand for high coercivity (NdDy)-Fe-B type permanent magnets. Hence, it is of great industrial interests to develop Dy-free high-coercivity Nd-Fe-B magnets.

Initially proposed by Lee et al., hot-deformation is another process to fabricate anisotropic Nd-Fe-B-type magnets with ultra-fine grain sized microstructure from the melt-spun ribbons [68,69]. One distinguishing merit obtained from hot-deformed magnets is the small grain size (~400 nm) in hot-deformed magnets, which is significantly smaller than that (~2-5 μm) of sintered magnets. Note that single domain size of the $Nd_2Fe_{14}B$ phase is ~260 nm, which is comparable with the grain size of hot-deformed magnets. Hence, in comparison with sintered magnets, the hot-deformed magnets are believed to have greater potential to achieve higher coercivity, which recommends hot-deformed Nd-Fe-B-type magnets as a promising candidate for the development of high-coercivity Dy-free permanent magnets. Based on relationship between grain size and coercivity in sintered magnets [16], the coercivity of the hot-deformed magnets is expected to be ~2.5 T, which is much higher than that experimentally reported coercivity (~1.5 T).

The coercivity, as extrinsic properties, is highly sensitive to microstructure, such as chemistry of grain boundary phase, grain size and grain shape. The microstructure is heavily depended on processing conditions. For instance, the grain size can be reduced from ~1000 nm to ~200 nm by decreasing hot-deformation from 900°C to 750°C [31]. Further microstructure characterization indicated that RE-rich grain boundary phase and small grain size contributes to higher coercivity. To exploit potential of coercivity in hot-deformed magnets, further optimizing processing condition is required.

The other key issue in hot-deformed magnet is inhomogeneous microstructure in hot-deformed magnet. Specifically, in the typical microstructure of the hot-deformed magnets, two kinds of distinguishable regions are observed: one is well-textured platelet-like grains within ribbons and the other is coarse non-oriented grains (surface crystallites) at the interface of stacked ribbons [70]. The former contributes to high remanent magnetization or high energy density in hot-deformed magnets and the latter causes reduced remanent magnetization and lower nucleation field. Extensive attempts have been made to achieve uniform microstructure in the hot-deformed

magnets. Recently, Mouri *et al* [71] reported that these coarse and isotropic grains could be inhibited by two-stage hot deformation. Blending WC hard nanoparticles with MQU-F powders was also reported to suppress the coarse grain growth due to the compressive stress induced by localized WC nanoparticles on the surface of ribbons, thus resulted in increase of both remanence and coercivity in hot-deformed magnets [72]. It should be noteworthy that all the hot-deformed magnets were processed from melt-spun ribbons and these localized non-aligned surface crystallites should be closely related to inhomogeneous microstructure in the melt-spun ribbons. By tuning the composition of the ribbons, it should be feasible to eliminate the surface crystallites to achieve optimized microstructures in melt-spun ribbons and hot-deformed magnets.

Coupling with supply restriction and increasing demand of these critical elements (such as Nd, Pr, Dy), the price of these critical elements has been rising. On the other hand, the other rare earth element with low cost, such as La and Ce, left unexplored. However, the hot-deformed Ce-Fe-B magnets showed a very low coercivity of ~7 $\times 10^{-4}$ T [66]. Given the relatively high anisotropy field of the $Ce_2Fe_{14}B$ phase (~3 T), the coercivity value reported for the hot-deformed Ce-Fe-B magnet is too low. The eutectic grain boundary diffusion process has widely been applied to enhance the coercivity in HDDR, nanocomposite and hot-deformed magnets [34,36–38]. Recently, Ito *et al*. reported that the coercivity of Ce-Fe-B hot-deformed magnets is enhanced by the infiltration of an eutectic Nd-Cu alloy [73]. After infiltration of Nd-Cu, the core-shell structure can be well formed in 2:14:1 phase. Even the Nd-rich shell in 2:14:1 phase would increase magnetocrystalline anisotropy as well as coercivity, but the coercivity is not enhanced as much as expected. Further fundamental work needs to be done to clarify the mechanism of coercivity in Nd-Cu diffusion processed Ce-Fe-B sample.

On the other hand, to explore the potential application of Ce-substituted magnets, the hard magnetic properties of Ce-substituted magnets should be superior or at least comparable to Nd-Fe-B counterparts. Up to dates, there are no reports on Ce-substituted magnets with comparable magnetic properties of Nd-Fe-B magents. Recent researches on single crystalline $(Nd_{1-x}Ce_x)_2Fe_{14}B$ compounds have demonstrated that anisotropy field is well preserved up to x~0.3 and further density functional theory calculations [74,75] have shown that there is no phase separation up to x~0.3. It indicates that high performance Ce-containing sample can be achieved by controlling the microstructure.

In this thesis, the optimization of processing condition and composition in melt-spun ribbons is carried out. Specifically, varying the cool rate by changing the wheel speed during melt-spinning to obtain different grain size in melt-spun ribbons. Hereafter, magnetic properties and microstructure of hot-deformed magnets processed from amorphous and crystalline melt-spun powders are systematically compared to obtain optimal processing route for hot-deformed magnets. This will be shown in chapter 3. Chapter 4 will show that further optimizing composition in melt-spun ribbons leads to suppression of surface crystallites and obtaining uniform microstructure. The coercivity enhancement in Ce-Fe-B by grain boundary diffusion of Nd-Cu will be included in chapter 5. Hereafter, chapter 6 will demonstrate fabrication of high-performance Ce-substituted Nd-Fe-B hot-deformed magnet by doping Co, in which the magnetic properties of hot-deformed magnet with 10 at.% Ce substitution are superior to those of Ce-free Nd-Fe-B hot-deformed magnets.

Reference

[1] O. Gutfleisch, M.A. Willard, E. Brück, C.H. Chen, S.G. Sankar, J.P. Liu, Adv. Mater. 23 (2011) 821–842.

[2] S. Sugimoto, J. Phys. Appl. Phys. 44 (2011) 064001.

[3] K. Strnat, G. Hoffer, W. Ostertag, J.C. Olson, J. Appl. Phys. 37 (1966) 1252–1253.

[4] E.A. Nesbitt, J.H. Wernick, E. Corenzwit, J. Appl. Phys. 30 (1959) 365–367.

[5] T. Ojima, S. Tomizawa, T. Yoneyama, T. Hori, IEEE Trans. Magn. 13 (1977) 1317–1319.

[6] T. Ojima, S. Tomizawa, T. Yoneyama, T. Hori, Jpn. J. Appl. Phys. 16 (1977) 671–672.

[7] M. Sagawa, S. Fujimura, N. Togawa, H. Yamamoto, Y. Matsuura, J. Appl. Phys. 55 (1984) 2083–2087.

[8] J.J. Croat, J.F. Herbst, R.W. Lee, F.E. Pinkerton, J. Appl. Phys. 55 (1984) 2078–2082.

[9] J.F. Herbst, J.J. Croat, F.E. Pinkerton, W.B. Yelon, Phys. Rev. B 29 (1984) 4176–4178.

[10] http://www.shinetsu-rare-earth-magnet.jp/e/masspro/.

[11] R.K. Mishra, E.G. Brewer, R.W. Lee, J. Appl. Phys. 63 (1988) 3528–3530.

[12] R.K. Mishra, T.-Y. Chu, L.K. Rabenberg, J. Magn. Magn. Mater. 84 (1990) 88–94.

[13] L. Li, C.D. Graham, J. Appl. Phys. 67 (1990) 4756–4758.

[14] L. Li, C.D. Graham, IEEE Trans. Magn. 28 (1992) 2130–2132.

[15] X. Tang, R. Chen, W. Yin, J. Wang, X. Tang, D. Lee, A. Yan, J. Alloys Compd. 623 (2015) 386–392.

[16] K. Hono, H. Sepehri-Amin, Scr. Mater. 67 (2012) 530–535.

[17] X. Tang, H. Sepehri-Amin, T. Ohkubo, K. Hioki, A. Hattori, K. Hono, Acta Mater. 123 (2017) 1–10.

[18] D. Givord, M.F. Rossignol, D.W. Taylor, J. Phys. IV 02 (1992) C3-95-C3-104.

[19] D. Givord, P. Tenaud, T. Viadieu, IEEE Trans. Magn. 24 (1988) 1921–1923.

[20] D. Givord, A. Lienard, P. Tenaud, T. Viadieu, J. Magn. Magn. Mater. 67 (1987) L281–L285.

[21] H. Sepehri-Amin, Y. Une, T. Ohkubo, K. Hono, M. Sagawa, Scr. Mater. 65 (2011) 396–399.

[22] D.W. Scott, B.M. Ma, Y.L. Liang, C.O. Bounds, J. Appl. Phys. 79 (1996) 5501.

[23] P. Nothnagel, K.-H. Müller, D. Eckert, A. Handstein, J. Magn. Magn. Mater. 101 (1991) 379–381.

[24] K. Uestuener, M. Katter, W. Rodewald, IEEE Trans. Magn. 42 (2006) 2897–2899.

[25] Une Y., Sagawa M., J. Jpn. Inst. Met. 76 (2012) 12–16.

[26] M. Leonowicz, J. Magn. Magn. Mater. 83 (1990) 211–213.

[27] S. Pandian, V. Chandrasekaran, G. Markandeyulu, K.J.L. Iyer, K.V.S. Rama Rao, J. Appl. Phys. 92 (2002) 6082–6086.

[28] Y. Zhang, J. Han, S. Liu, F. Wan, H. Tian, X. Zhang, C. Wang, J. Yang, Y. Yang, Scr. Mater. 110 (2016) 57–60.

[29] R.J. Pollard, P.J. Grundy, S.F.H. Parker, D.G. Lord, IEEE Trans. Magn. 24 (1988) 1626–1628.

[30] Y.Q. Wu, D.H. Ping, X.Y. Xiong, K. Hono, J. Appl. Phys. 91 (2002) 8174.

[31] J. Liu, H. Sepehri-Amin, T. Ohkubo, K. Hioki, A. Hattori, T. Schrefl, K. Hono, Acta Mater. 82 (2015) 336–343.

[32] H. Kronmüller, Phys. Status Solidi B 130 (1985) 197–203.

[33] H. Sepehri-Amin, T. Ohkubo, K. Hono, Mater. Trans. 57 (2016) 1221–1229.

[34] H. Sepehri-Amin, T. Ohkubo, T. Nishiuchi, S. Hirosawa, K. Hono, Scr. Mater. 63 (2010) 1124–1127.

[35] H. Sepehri-Amin, J. Liu, T. Ohkubo, K. Hioki, A. Hattori, K. Hono, Scr. Mater. 69 (2013) 647–650.

[36] H. Sepehri-Amin, T. Ohkubo, S. Nagashima, M. Yano, T. Shoji, A. Kato, T. Schrefl, K. Hono, Acta Mater. 61 (2013) 6622–6634.

[37] X. Tang, R. Chen, W. Yin, J. Wang, X. Tang, D. Lee, A. Yan, Appl. Phys. Lett. 102 (2013) 072409.

[38] X. Tang, R. Chen, W. Yin, J. Wang, X. Tang, D. Lee, A. Yan, Scr. Mater. 88 (2014) 49–52.

[39] L. Liu, H. Sepehri-Amin, T. Ohkubo, M. Yano, A. Kato, T. Shoji, K. Hono, J. Alloys Compd. 666 (2016) 432–439.

[40] L. Liu, H. Sepehri-Amin, T. Ohkubo, M. Yano, A. Kato, N. Sakuma, T. Shoji, K. Hono, Scr. Mater. 129 (2017) 44–47.

[41] U.M.R. Seelam, T. Ohkubo, T. Abe, S. Hirosawa, K. Hono, J. Alloys Compd. 617 (2014) 884–892.

[42] U.M.R. Seelam, L. Liu, T. Akiya, H. Sepehri-Amin, T. Ohkubo, N. Sakuma, M. Yano, A. Kato, K. Hono, J. Magn. Magn. Mater. 412 (2016) 234–242.

[43] K. Loewe, D. Benke, C. Kübel, T. Lienig, K.P. Skokov, O. Gutfleisch, Acta Mater. 124 (2017) 421–429.

[44] T. Akiya, J. Liu, H. Sepehri-Amin, T. Ohkubo, K. Hioki, A. Hattori, K. Hono, Scr. Mater. 81 (2014) 48–51.

[45] H.-R. Cha, K.-W. Jeon, J.-H. Yu, H.-W. Kwon, Y.-D. Kim, J.-G. Lee, J. Alloys Compd. 693 (2017) 744–748.

[46] Y.I. Lee, H.W. Chang, G.Y. Huang, C.W. Shih, W.C. Chang, IEEE Trans. Magn. 53 (2017) 1–4.

[47] W.C. Chang, S.H. Wu, B.M. Ma, C.O. Bounds, J. Magn. Magn. Mater. 167 (1997) 65–70.

[48] W. Chang, D. Chiou, B. Ma, C. Bounds, J. Magn. Magn. Mater. 189 (1998) 55–61.

[49] J.M.D. Coey, IEEE Trans. Magn. 47 (2011) 4671–4681.

[50] C. Yan, S. Guo, R. Chen, D. Lee, A. Yan, IEEE Trans. Magn. 50 (2014) 1–5.

[51] A.K. Pathak, M. Khan, K.A. Gschneidner, R.W. McCallum, L. Zhou, K. Sun, K.W. Dennis, C. Zhou, F.E. Pinkerton, M.J. Kramer, V.K. Pecharsky, Adv. Mater. 27 (2015) 2663–2667.

[52] M. Zhang, Z. Li, B. Shen, F. Hu, J. Sun, J. Alloys Compd. 651 (2015) 144–148.

[53] M. Hussain, L.Z. Zhao, C. Zhang, D.L. Jiao, X.C. Zhong, Z.W. Liu, Phys. B Condens. Matter 483 (2016) 69–74.

[54] M. Hussain, J. Liu, L.Z. Zhao, X.C. Zhong, G.Q. Zhang, Z.W. Liu, J. Magn. Magn. Mater. 399 (2016) 26–31.

[55] Z. Li, M. Zhang, B. Shen, F. Hu, J. Sun, Mater. Lett. 172 (2016) 102–104.

[56] X. Fan, S. Guo, K. Chen, R. Chen, D. Lee, C. You, A. Yan, J. Magn. Magn. Mater. 419 (2016) 394–399.

[57] X. Fan, K. Chen, S. Guo, R. Chen, D. Lee, A. Yan, C. You, Appl. Phys. Lett. 110 (2017) 172405.

[58] Y. Zhang, T. Ma, J. Jin, J. Li, C. Wu, B. Shen, M. Yan, Acta Mater. 128 (2017) 22–30.

[59] B. Peng, T. Ma, Y. Zhang, J. Jin, M. Yan, Scr. Mater. 131 (2017) 11–14.

[60]https://www.revolvy.com/main/index.php?s=Abundance%20of%20elements%20in%20Earth%27s%20crust&item_type=topic

[61] J.F. Herbst, Rev. Mod. Phys. 63 (1991) 819–898.

[62] Z.Y. Zhang, L.Z. Zhao, J.S. Zhang, X.C. Zhong, W.Q. Qiu, D.L. Jiao, Z.W. Liu, Mater. Res. Express 4 (2017) 086503.

[63] X.B. Liu, Z. Altounian, M. Huang, Q. Zhang, J.P. Liu, J. Alloys Compd. 549 (2013) 366–369.

[64] A.M. Gabay, G.C. Hadjipanayis, IEEE Trans. Magn. 53 (2017) 1–4.

[65] K. Pei, X. Zhang, M. Lin, A. Yan, J. Magn. Magn. Mater. 398 (2016) 96–100.

[66] R.-Q. Wang, X. Shen, Y. Liu, J. Li, IEEE Trans. Magn. 52 (2016) 1–6.

[67] M. Sagawa, S. Fujimura, H. Yamamoto, Y. Matsuura, K. Hiraga, IEEE Trans. Magn. 20 (1984) 1584–1589.

[68] R. Lee, E. Brewer, N. Schaffel, IEEE Trans. Magn. 21 (1985) 1958–1963.

[69] R.W. Lee, Appl. Phys. Lett. 46 (1985) 790–791.

[70] J. Liu, H. Sepehri-Amin, T. Ohkubo, K. Hioki, A. Hattori, K. Hono, J. Appl. Phys. 115 (2014) 17A744.

[71] T. Mouri, M. Kumano, H.Y. Yasuda, T. Nagase, R. Kato, Y. Nakazawa, H. Shimizu, Scr. Mater. 78–79 (2014) 37–40.

[72] X. Zheng, M. Li, R. Chen, F. Lei, C. Jin, Z. Wang, J. Ju, W. Yin, D. Lee, A. Yan, Scr. Mater. 132 (2017) 49–52.

[73] M. Ito, M. Yano, N. Sakuma, H. Kishimoto, A. Manabe, T. Shoji, A. Kato, N.M. Dempsey, D. Givord, G.T. Zimanyi, AIP Adv. 6 (2016) 056029.

[74] M.A. Susner, B.S. Conner, B.I. Saparov, M.A. McGuire, E.J. Crumlin, G.M. Veith, H. Cao, K.V. Shanavas, D.S. Parker, B.C. Chakoumakos, B.C. Sales, J. Magn. Magn. Mater. 434 (2017) 1–9.

[75] A. Alam, M. Khan, R.W. McCallum, D.D. Johnson, Appl. Phys. Lett. 102 (2013) 042402.

Chapter 2: Experimental procedure

2.1 Sample Processing procedures

To produce hot-deformed samples, there are at least four steps comprising of induction melting, melt-spinning, hot-pressing and hot-deformation. Alloy ingots are produced by induction melting from raw elements or compounds. The as-melt ingots were subjected to melt-spinning under proper conditions. Subsequently, the melt-spun ribbons are compacted to get green compacts under optimized condition, followed by hot-deformation at elevated temperature. The hot-deformed magnets with different compositions and processing conditions are thus obtained.

2.1.1 Induction Melting Furnace

Induction melting has widely applied to melt raw materials to get uniform ingot. In general, induction melting furnace comprises of vacuum system and heating system. The vacuum system is equipped with rotatory pump and diffusion pump to be capable of evacuating to a background pressure of ~10^{-3} pa. The heating system consists of a nonconductive crucible (Al_2O_3) holding the charge of metal to be melted, surrounded by a coil of copper wire. A powerful alternating current flows through the copper wire, generating a rapidly reversing magnetic field that penetrates the metal. Then the eddy current is induced, which flows through bulk metal with electrical resistance, the bulk materials is heated by joule heating. Once melted, the eddy currents cause vigorous stirring of the molten alloys, assuring homogeneous mixing. The raw elements and compounds with total mass of around 200 gram are place into an Al_2O_3 crucible. After vacuum reaches 4×10^{-3} Pa, Ar is introduced into chamber until chamber pressure reaches to 4×10^{4} Pa. The current increases gradually to avoid vaporization of volatile elements. After all the elements melt, holding for 5 minutes to make sure homogeneous mixing, followed by casting on a low-carbon steel mold.

2.1.2 Melt-spinning

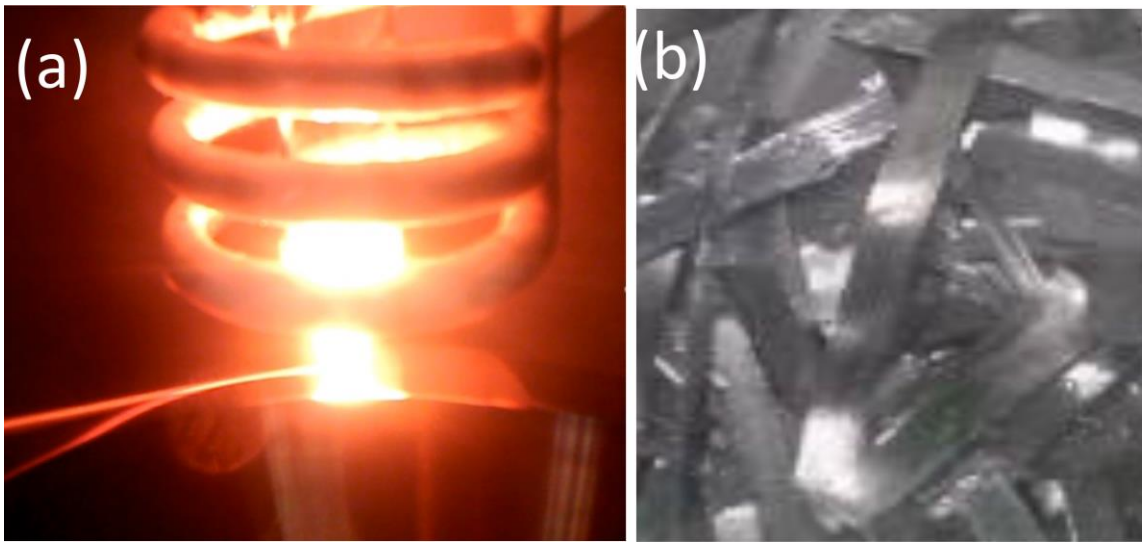

Fig.1 (a) the image taken during melt-spinning and (b) the ribbons obtained from melt-spinning.

Melt spinning is a commonly-used technique to obtain the rapidly-solidified ribbon. The ingots are placed into a quartz tube with a nozzle heated by copper coil, the molten alloy is ejected through a narrow nozzle, then a thin stream of liquid is then dripped onto the rotating copper wheel and cooled, causing rapid solidification. By using melt-spinning technique, a extremely high cooling rate at the order of 10^4–10^7 K/s can be achieved. By adjusting the wheel speed, cooling rate can be tunable and different grain sizes yield in melt-spun ribbon. In this experiment, with speed of 20 m/s, grains with average size of 30 nm can be obtained in nanocrystalline ribbons and with increasing the speed to 40 m/s, amorphous ribbons is achieved after melt-spinning. The nozzle diameter and chamber pressure are optimized to be 0.75 mm and 3×10^4 Pa, respectively.

2.1.3 Hot-pressing and hot-deformation

The hot-pressing and hot-deformation are carried out on the same machine using different moulds. The hot-pressing machine is equipped with vacuum system, pressure system and heating system. The vacuum system makes sure hot working is carried out under oxygen-free atmosphere while pressure system with maximum pressure of 100 KN can meet any requirement of pressure during the hot-pressing and hot-deformation system. The heating system with controlling program

can heat up the sample to 1000 °C within several minutes by induction heating. The melt-spun ribbons are placed into WC die with 10 mm diameter, which is rapidly heated up to 650 °C in 4 minutes. By application of pressure of 28 KN for 10 seconds, the densification is accomplished and hot-pressed magnet with density of above 7.50 g/cm^3 is obtained. The green compact with 10 mm diameter is subsequently placed into an oversized die with a diameter of 20 mm. Then the sample is rapidly heated up to 850 °C in 4 minutes to avoid excessive grain growth, followed by 30 s holding time to ensure homogeneous temperature distribution. Hereafter, a pressure is gradually applied to keep a constant deformation speed. After height reduction achieve 75%, the deformation process is accomplished.

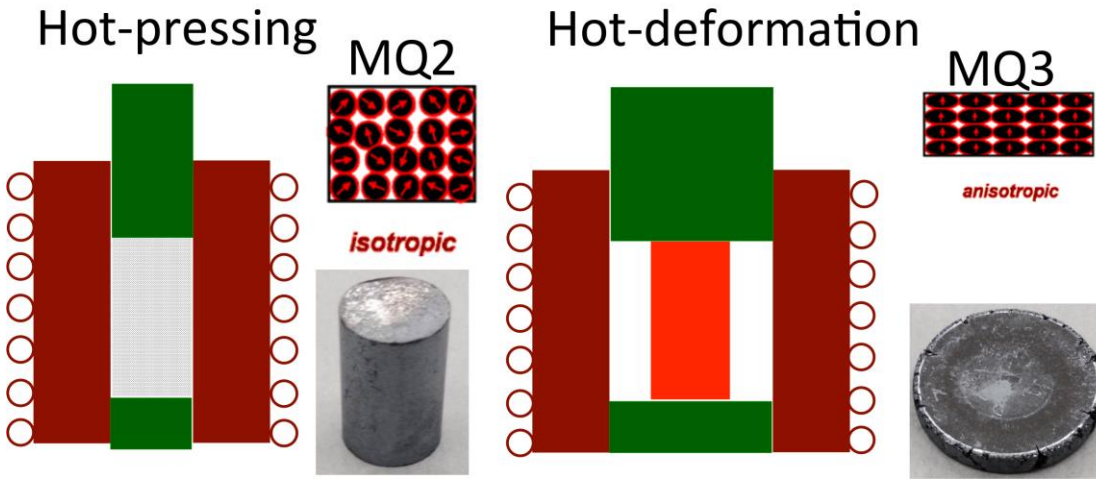

Fig.2. Schematics of hot-pressing and hot-deformation.

2.1.4 Grain boundary diffusion

The grain boundary diffusion of RE-based eutectic alloys, which is detailed in ref. [1], has widely applied to increase coercivity of Nd-Fe-B magnets. As illustrated in Fig. 3, the magnet is covered with RE-based eutectic alloys and then heat-treated at above eutectic point for few hours under vacuum in a furnace. It is seen that grain boundary is thickening after grain boundary, indicating that the RE-based eutectic alloys was melting and infiltrated through the grain boundaries from the surface of magnet into the inside of magnet. In this thesis, the diffusion source of $Nd_{70}Cu_{30}$ alloys was prepare from melt-spinning. The melt-spun ribbons is crushed into powders and then the hot-deformed Ce-Fe-B magnets covered by the $Nd_{70}Cu_{30}$ ribbons are heat-treated at

700°C for 6 h. Ce-Fe-B magnets infiltrated with 10 wt.% and 40 wt.% $Nd_{70}Cu_{30}$ are fabricated by controlling the amount of diffusion source.

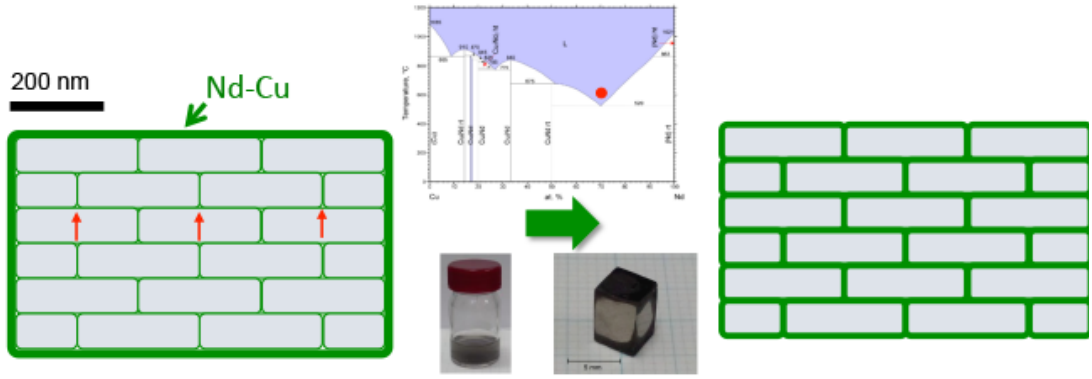

Fig.3. Schematics of grain boundary diffusion of Nd-Cu. Courtesy by K. Hono.

2.2 Characterization techniques

2.2.1 BH tracer and superconducting quantum interface device vibrating sample magnetometer (SQUID-VSM)

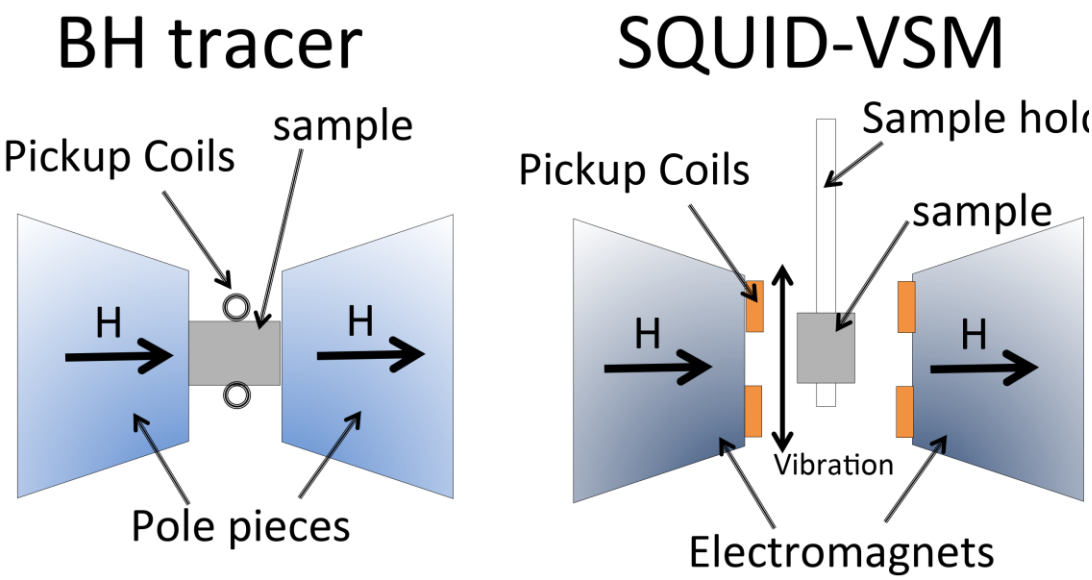

Fig.4. Schematics of BH tracer and SQUID-VSM.

The BH tracer and SQUID-VSM are employed to characterize the magnetic properties in this work. The closed circuited BH tracer has widely applied to test magnetic properties of big-sized permanent magnet. As shown in Fig. 4, the sample wrapped by coil is placed between two

pole pieces of an electromagnet, the change in magnetic flux density of sample with change of external field generated by electromagnets is measured by fluxmeter, the BH loops and magnetic properties can be obtained. Since the sample is physically contacted with pole, No demagnetization corrections need to be taken into considerations. In contrast, a vibrating sample magnetometer (VSM) [2] is operated based on Faraday's Law of Induction, which means that a changing magnetic field will produce an electric field. By measuring electric field, information about the changing magnetic field can be acquired. The VSM is an open-circuited measurement method, the demagnetization correction, depending on sample geometry, needs to be taken into considerations. In general, the sample for BH tracer measurement is much bigger than SQUID-VSM sample while VSM measure is much more time-consuming than BH tracer measurement.

2.2.2 Scanning electron microscopy and focus ion beam (FIB)

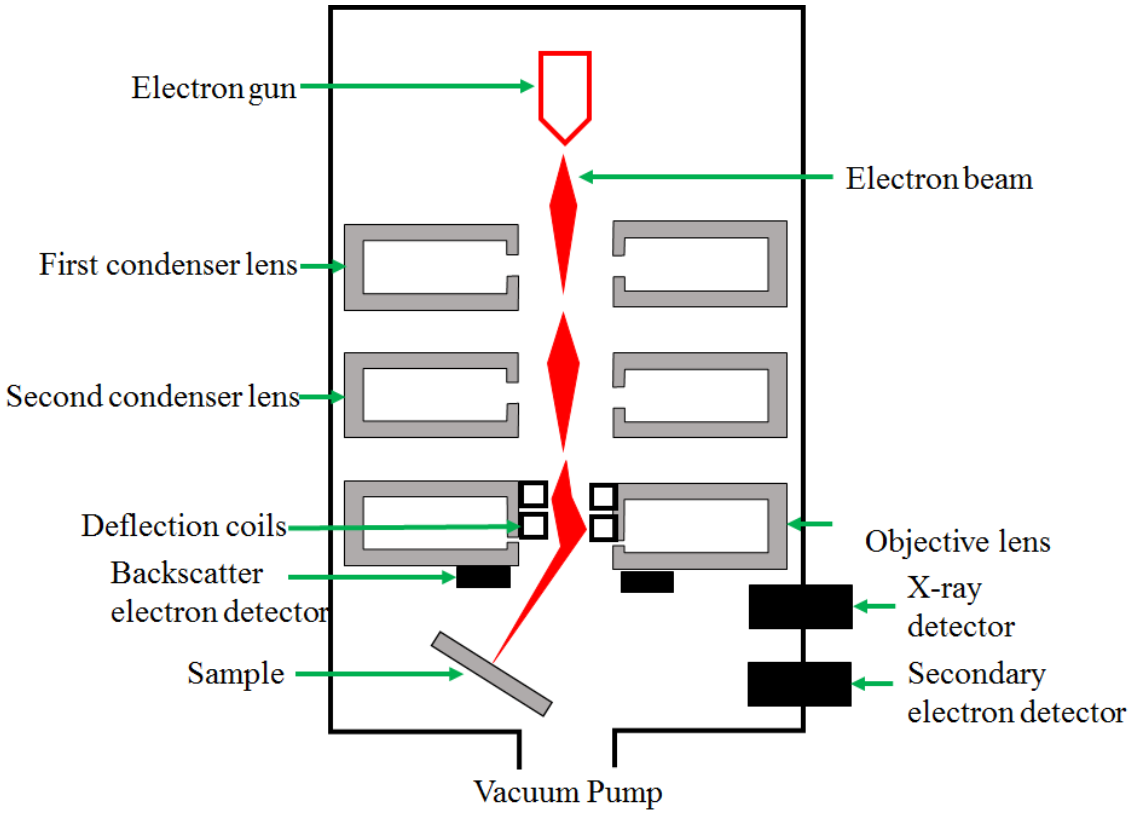

Fig.5. Schematic of a SEM.

Scanning electron microscope (SEM) is a type of electron microscope that can provide microstructure observations. The images of sample are produced by scanning the sample surface with a focused beam of electrons. Fig. 5 shows schematic of an SEM. It is seen that the electron

beam is emitted from a field emission gun (FEG). The electron beam with energy range from 1 keV to 30 keV is focused by one or two condenser lenses to a spot with 0.4 nm to 5 nm in diameter. Then the focused electron beam passes through pairs of deflector plates in the electron column, with which the beam can be deflected in the *x* and *y* axes to scan the sample surface.

When the incident electron beam hit the sample surface, a interaction volume as shown in Fig. 6 is generated, which penetrates into sample with penetration depth of approximately 5 μm into the surface. The interaction between the incident beam and sample surface give rises to various signals as shown in Fig. 6. By collecting these signals using different types of detectors, information about the sample's surface topography and composition can be obtained [3]. An image containing information of topography of the surface is produced by scanning the sample surface and collecting the emitted secondary electrons. Due to the fact the electrons are back scattered more strongly by heavier elements, the areas enriched with heavier element show brighter contrast in a back scattered SEM image. The areas with different chemical compositions can be obtained by backscattered electrons (BSE) images. For examples, in Nd-Fe-B magnets, the grain boundaries enriched with heavy element, i.e. Nd, show a brighter contrast compared to the 2:14:1 matrix phase. By employing energy-dispersive X-ray spectroscopy (EDS) to collect the characteristic X-rays, the elemental distribution can be acquired. In this thesis, the overall microstructure were investigated on Carl Zeiss CrossBeam1540EsB with a resolution of 1 nm. The sample for SEM observation is roughly polished by abrasive Si paper followed by FIB polishing, which will be explained in detail in following session.

Focused ion beam (FIB), have widely applied to polish the sample or prepare TEM and atom probe samples. Generally, the FIB system is incorporated into a SEM system for micro-fabrications. Instead of using a focused beam of electrons for imaging, focused beam of ions in FIB is used to etch sample. The liquid metal ion sources (LMIS), for example, gallium ion, are used as ion sources in FIB. The heated gallium flows to needle tip, where gallium is ionized and emitted by large electric field. Then ionized gallium source accelerated to an energy of 1–50 keV. Focus ion beam can provide high current density ion beams with very small energy spread. The spot size of focused ion beam is about a few nanometers, which much larger than focused beam of electrons, indicating inferior resolution. Depending on beam size, the resolution of FIB image ranges from 2.5 to 15 nm. After focused ion beam hits the sample surface, generates sputtered ions and secondary electrons, which can be collected to produce an image. Because of the sputtering

capability, the FIB is widely applied to do micro- and nano-machining, for example, polishing the surface of sample for better imaging, prepare thin foil for TEM, or making needle-shaped tip for atom probe analyses.

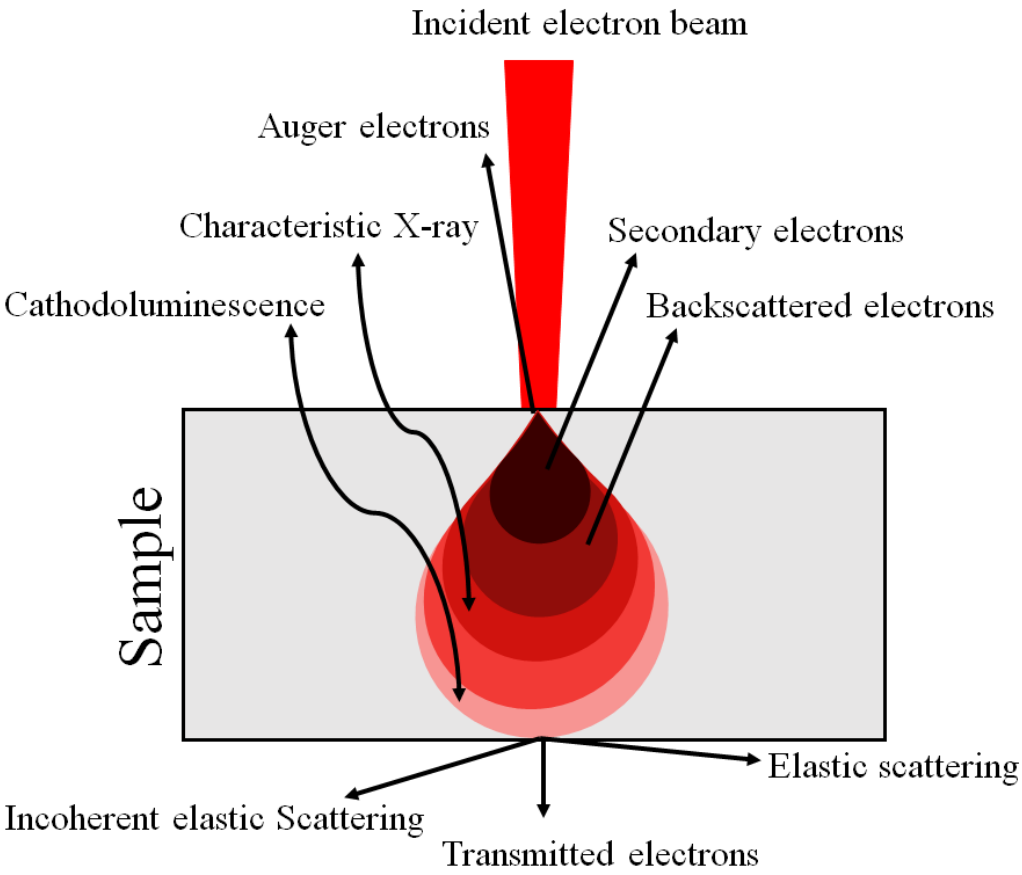

Fig.6. Interaction between electron beam and sample.

2.2.3 Transmission electron microscopy (TEM) and TEM sample preparation

Transmission electron microscopy (TEM) is powerful instrument to conduct nano-scale analysis in various materials, which is capable of capturing very detailed information because of small wavelength of electrons. In a typical TEM [4], it comprises four component: (1) an electron gun, providing the electron source; (2) condenser system, focusing the beam and deflecting the beam onto the sample; (3) the image-producing and recording system, converting the electron image to perceptible image; and (4) ultra-high vacuum system. Fig. 7 shows the schematic of a TEM. The electron beam is emitted from electron gun placed on the top of column of microscope, travels through in vacuum and focused into a thin beam by several sets of electromagnetic lenses.

Then pass through the TEM specimen, some electron are scattered and disappear from the beam. The unscattered electrons hit a fluorescent screen, forming a “shadow image” followed by image-processing system, the perceptible image can be produced.

(a) Conventional TEM: bright field and dark field imaging

The bright field imaging is the most common mode for TEM operation. Depending on sample thickness or density, different contrast can be documented in bright field image. Specifically, the more electrons are blocked by thicker region and denser area with heavier atoms, showing a dark contrast in an image, while the thinner area, lower density and lower atomic number regions appear to be bright. The bright field imaging model normally gives information of grain size and grain morphology. In contrast, the dark field imaging model contains the information about diffracted electrons. In dark field (DF) imaging, the direct beam is blocked by the aperture while one or more diffracted beams are allowed to pass the objective aperture. The electrons scattered at relatively large angles are collected to construct dark-field image, which contains various information, e.g., about orientation of crystals, planar defects or stacking faults. By using selected area diffraction (SAD) or nanobeam electron beam diffraction (NEBD), the phase in microstructure can be identified by analyzing the diffraction patterns.

(b) Dark field imaging STEM-HAADF

In a conventional TEM, the images are produced by electron beam traveling through a thin sample. In contrast, the focused electron beam is scanned over the sample in a raster in STEM, which makes it suitable for many analytical techniques, such as high angle annular dark field imaging, elemental mapping by energy dispersive X-ray spectroscopy (EDS) or electron energy loss spectroscopy (EELS). These data can be acquired in parallel. In a STEM, by collecting high angle scattered electrons using an annular dark-field detector, a high angle annular dark field (HAADF) image is generated. Since the high angle scattered electrons are strongly influenced by variations in the atomic number (Z) of atoms of the sample, the contrast in HAADF image comes from the Z contrast. For example, in a HAADF image obtained from Nd-Fe-B magnets, the grain boundaries enriched with heavier elements (Nd) are more brightly imaged. HAADF imaging is also commonly performed in parallel with energy dispersive X-ray spectroscopy acquisition to obtain elemental maps in sample or analyze the composition in grain boundaries.

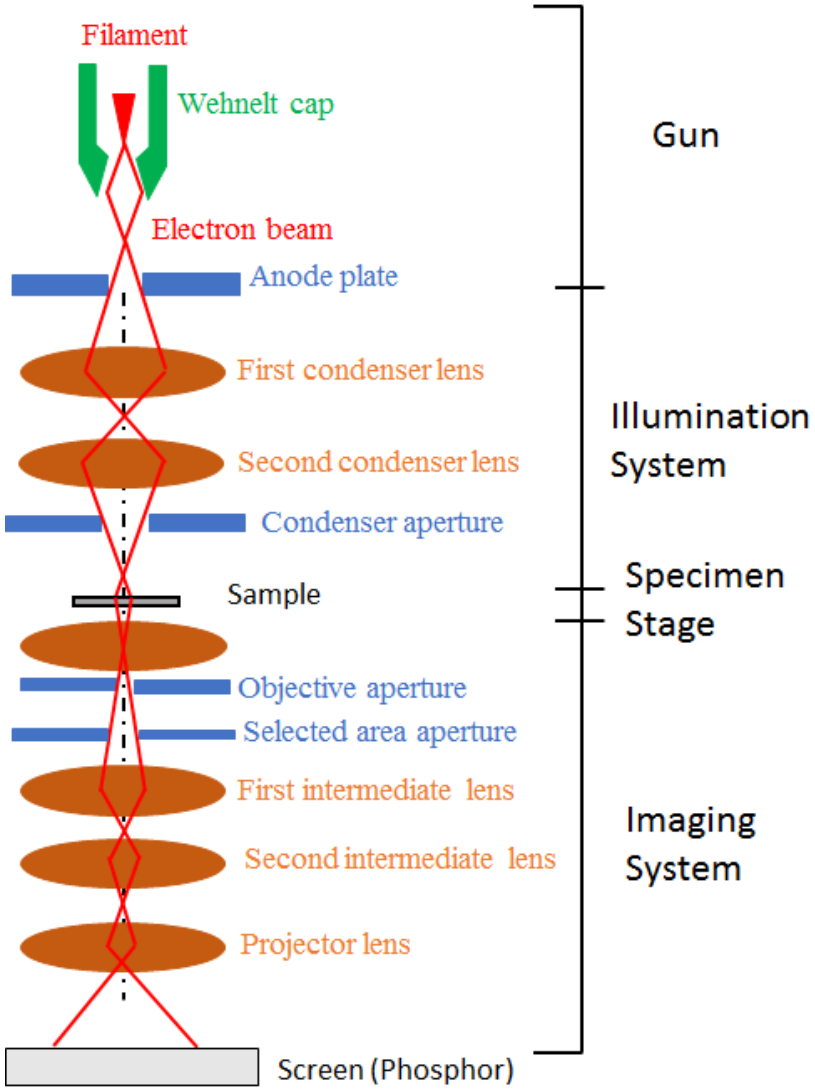

Fig.7. Schematic of a TEM.

(c) Sample preparation

The TEM sample is prepared on the dual beam SEM system (Helios 650) by FIB method, which is comprised of three steps: (i) the deposition of the protective material, (ii) specimen lift-out and pasting on sample holder and (iii) thinning the TEM specimen and final cleaning. First, during the FIB micromachining, the surface of the selected area has to be protected from ion impacts and from the redeposit of sputtered materials, Pt is commonly used as protective materials. After deposition of Pt, cut out specimen using FIB and lift out sample using omoni-probe then paste the specimen on sample holder. Hereafter, thinning specimen step by step by gradually

reducing the voltage and current of FIB, once the thickness of specimen reaches 30-50 nm, cleaning it using very small voltage and current (5 kV, 40 pA). Now, the specimen is ready for TEM observations, which is described in detail in ref. [5].

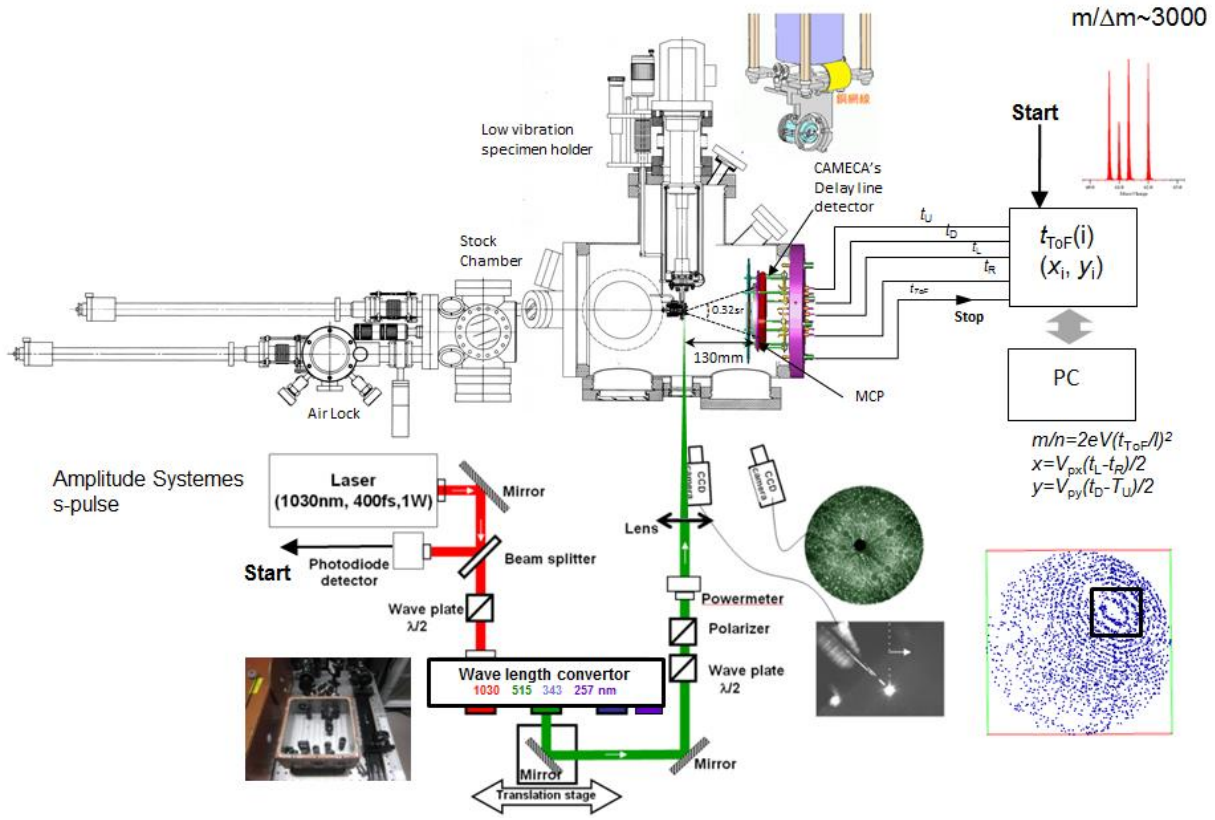

Fig.8. Schematic of an atom probe tomography. Courtesy by K. Hono.

2.2.4 Atom probe tomography

Atom probe tomography (APT) is a powerful instrument to give both 3D imaging and chemical composition measurements at the atomic scale. Compared to compositional analysis by EDS on TEM, atom probe tomography is much more quantitatively reliable, especially for analyzing light elements such as H, B. Inspired by Field Ion Microscopy (FIM), APT technique has been used to analyze conductive materials and further applied for analysis of non-conductive materials by implementation of pulsed laser to assist field evaporation [6–9]. It is shown in Fig. 8, the needle-shaped tip is placed in the high vacuum analysis chamber, the laser beam is focused and deflected by several set of lens and projected onto the sample for assisting the evaporation. The needle's outermost atoms become ionized after applying voltage pulses, flying from the tip

onto the 2D detector following a trajectory in ultrahigh vacuum. The mass-to-charge state of each atom can be recorded by measuring the time of flight (TOF). With the relative position on detector and TOF, the atom can be identified. Successive ionization of atom layer by layer, the information of a three dimension elemental map can be acquired. The acquired data is reconstructed and analyzed by commercially available IVAS software. The atom probe study in this thesis was carried out using a locally build laser-assisted three-dimensional atom probe under ultrahigh vacuum in a flux range of 0.003–0.01 atom per pulse using a femtosecond Yb:KGd $(WO_4)_2$ laser with a third harmonic generator (λ = 343 nm) and a laser power of 0.1 μJ $pulse^{-1}$. The atom probe sample is prepared on the dual beam SEM system (Helios 650) by FIB method. Firstly, the sample is lifted out using omoni-probe then pasted on sample holder. Hereafter, the diameter of specimen was reduced step by step and the final apex diameter of tip was less than 80 nm as shown in Fig. 9(b). More details about 3DAP sample preparation are reported in ref. [10–13].

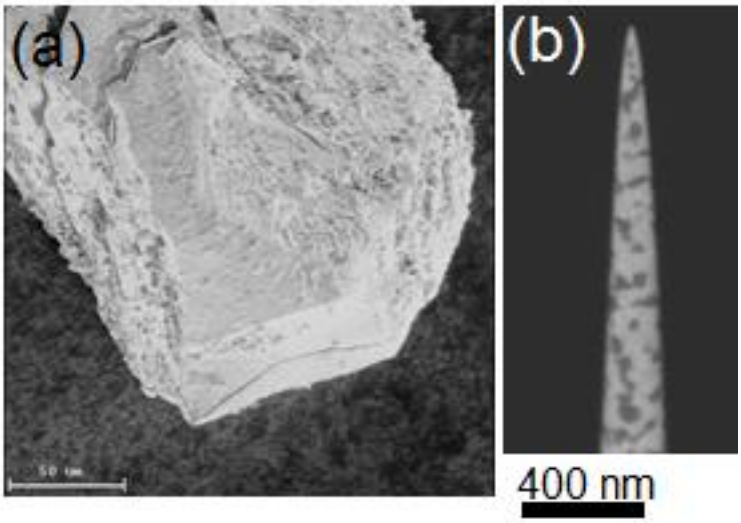

Fig.9. (a) sample (b) finalized the atom probe sample [9]

Reference

[1] H. Sepehri-Amin, T. Ohkubo, T. Nishiuchi, S. Hirosawa, K. Hono, Scr. Mater. 63 (2010) 1124–1127.

[2] https://en.wikipedia.org/wiki/Vibrating-sample_magnetometer

[3] https://en.wikipedia.org/wiki/Scanning_electron_microscope

[4] D. B.Williams, C. B. Carter, Transmission Electron Microscopy, Springer, 2009.

[5] M. Jublot, M. Texier, Micron 56 (2014) 63–67.

[6] K. Hono, Prog. Mater. Sci. 47 (2002) 621–729.

[7] D. Blavette, T. Al Kassab, E. Cadel, A. Mackel, F. Vurpillot, M. Gilbert, O. Cojocaru, B. Deconihout, Int. J. Mater. Res. 99 (2008) 454–460.

[8] T.F. Kelly, M.K. Miller, Rev. Sci. Instrum. 78 (2007) 031101.

[9] Y.M. Chen, T. Ohkubo, M. Kodzuka, K. Morita, K. Hono, Scr. Mater. 61 (2009) 693–696.

[10] K. Thompson, D. Lawrence, D.J. Larson, J.D. Olson, T.F. Kelly, B. Gorman, Ultramicroscopy 107 (2007) 131–139.

[11] M. Kodzuka, T. Ohkubo, K. Hono, F. Matsukura, H. Ohno, Ultramicroscopy 109 (2009) 644–648.

[12] M.K. Miller, K.F. Russell, G.B. Thompson, Ultramicroscopy 102 (2005) 287–298.

[13] H. Sepehri-Amin, T. Ohkubo, T. Nishiuchi, S. Hirosawa, K. Hono, Ultramicroscopy 111 (2011) 615–618.

Chapter 3: Coercivities of hot-deformed magnets processed from amorphous and nanocrystalline precursors

3.1 Introduction

Initially reported by Lee et al., hot-deformation is another process to fabricate textured Nd-Fe-B magnets with ultra-fine grain sized microstructure from the melt-spun ribbons [1,2]. Other than sintered magnets, the grain size of hot-deformed magnets is reported to be ~400 nm, which is much smaller than that (~2-5 μm) in sintered magnets, suggesting the hot-deformed magnets are supposed to have greater potential to achieve higher coercivity. To develop high-coercivity Dy-free permanent magnets, the hot-deformed magnets are promising candidates.

One approach to improve coercivity of Dy-free hot-deformed magnets is to apply grain boundary diffusion of RE-TM (where RE corresponds to the rare earth elements and TM stands for transition metal) on as-deformed hot-deformed magnets to reduce the concentration of ferromagnetic elements (such as Fe, Co) in grain boundary phases to weaken the intergranular exchange coupling [3–9]. Using Nd-Cu as diffusion source to infiltrate into the sample, the coercivity was increases to ~2.4 T with a reduction in remanent magnetization to ~1.1 T, because of the larger volume fraction of non-magnetic Nd-rich phases and degraded alignment of grains.

The other approach to increase the coercivity in hot-deformed magnet is to optimize the microstructures in hot-deformed magnets. Depending on processing conditions, the microstructures of hot-deformed magnets such as size and aspect ratio of grains (aspect ratio defined as ratio between the length along *c* plane and the length along *ab* plane: D_c/D_{ab}), chemistry of the intergranular phases change. Liu *et al* [10] reported that the grain size can be reduced to ~200 nm by deforming the sample at low temperature and the coercivity is enhanced to ~1.9 T. It should be noteworthy that the hot-deformed sample are generally prepared from nanocrystalline ribbons, by increasing the wheel speed in the melt-spinning process, amorphous ribbon can be obtained. In this chapter, we reported that the coercivity can be enhanced by produce hot-deformed magnets from amorphous precursors. Hereafter, the microstructures of hot-deformed magnets produced from nanocrystalline and amorphous melt-spun ribbons were systematically compared and investigated.

3.2 Experimental procedure

The ingots were prepared by induction melting out of the composition of $Nd_{28.4}Pr_{0.06}Fe_{66.57}Co_{3.41}Ga_{0.53}Al_{0.06}B_{0.97}$ (wt.%) or $Nd_{12.73}Pr_{0.03}Fe_{77.07}Co_{3.74}Ga_{0.49}Al_{0.14}B_{5.8}$ (at.%). The alloy ingots were melt-spun at 20m/s and 40 m/s, then nanocrystalline and amorphous melt-spun ribbons. Subsequently, these powders were subjected to hot-pressing and hot-deformation. The hot-pressed magnet processed from nanocrystalline powders (denoted as HPM-C) and that processed from amorphous powders (HPM-A) were obtained, while the hot-deformed magnets processed from the amorphous and nanocrystalline powders were denoted as HDM-A and HDM-C, respectively. The overall structures of the samples were identified by X-ray diffraction (XRD) with Cu K_α radiation. The detailed microstructures were investigated using a scanning electron microscope (SEM), transmission electron microscope (TEM).

3.3 Results

3.3.1 X-ray diffraction patterns and magnetic properties

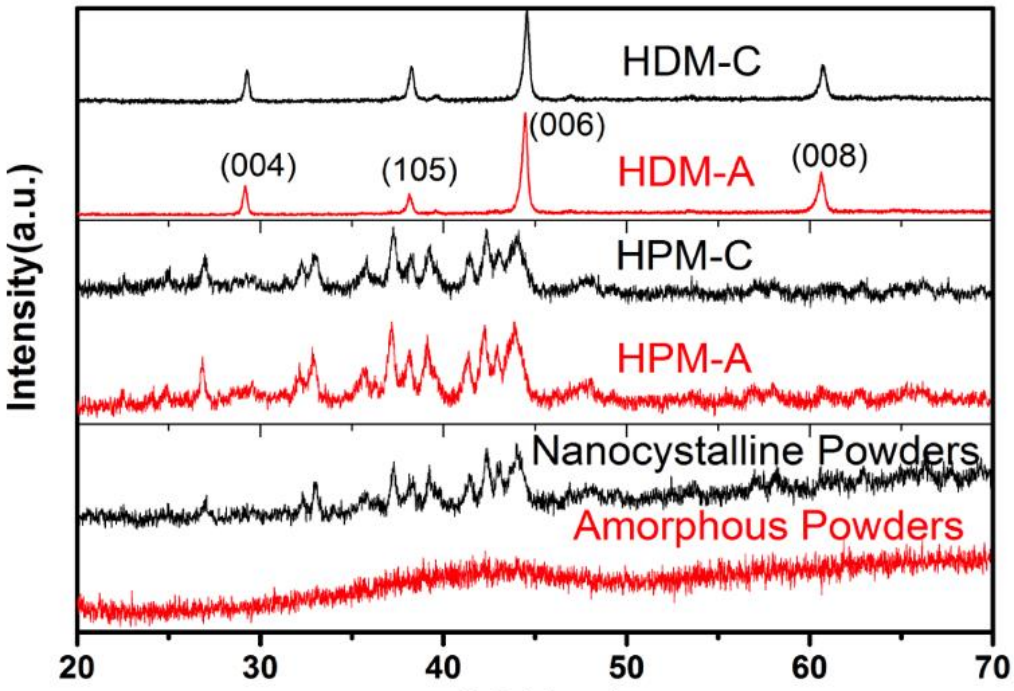

Figure 1. X-ray diffraction patterns of melt-spun powders, hot-pressed magnets and hot-deformed magnets.

Fig. 1 shows the X-ray diffraction patterns of initial magnetic powders, HPM and HDM processed from amorphous and nanocrystalline powders. There are no visible characteristic peaks from 2:14:1 phase observed in the XRD pattern of the amorphous powders. In comparison, the crystalline peaks from 2:14:1 phase appear in the diffraction pattern of the nanocrystalline powders. After hot-pressing, the amorphous phase is crystallized during hot-pressing and the sharp peaks can be indexed from the 2:14:1 phase in the HPM-A sample. The crystallization temperature of 2:14:1 phase is around 550 ℃, which is determined by DSC, much lower than hot-pressing temperature of 650℃. Consequently, the XRD patterns for HPM-A and HPM-C are similar and show random distributions of grains in the hot-pressed state. After hot-deformation at 850℃, the relative intensities of diffraction peaks of (004), (006) and (008) increases substantially, suggesting that a crystallographic texture along (001) has been achieved in hot-deformed magnets.

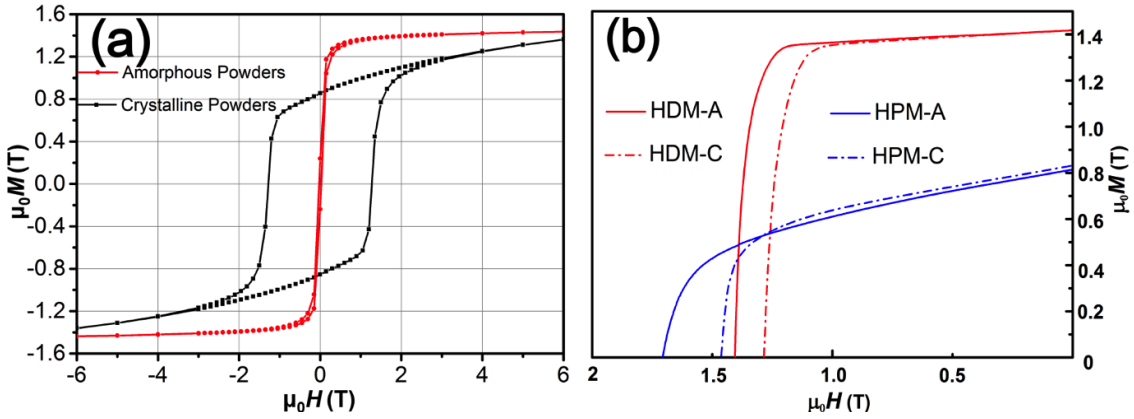

Figure 2. Magnetic properties of initial powders (a) and hot-pressed (HPM-C, HPM-A) and hot-deformed magnets (HDM-C. HDM-A) (b).

Fig. 2 shows magnetic properties of initial magnetic powders, HPM and HDM. It is seen in Fig. 2(a) that the coercivity ($\mu_0 H_c$) and remanence ($\mu_0 M_r$) of amorphous powders are determined to be ~0.029 T and ~0.21 T, respectively. In contrast, a coercivity of ~1.27 T with $\mu_0 M_r$ = 0.85 T is obtained in nanocrystalline powders due to presence of the hard magnetic 2:14:1 phase as shown in XRD patterns. After hot-pressing, the coercivity is significantly enhanced to ~1.67 T with a substantial increase of remanence to 0.8 T in hot-pressed magnet from amorphous powders. This is because that the crystallization process occurs during hot pressing process. In contrast, the coercivity slightly increase from ~1.27 to 1.46 T, which is smaller than that of HPM-A. After deforming at elevated temperature (850℃), the remanences are increased to ~1.42 T in both HDM-

C and HDM-A, while the coercivity is reduced to ~1.28 T in HDM-C and ~1.4 T in HDM-A, due to the development of a crystallographic texture after the process of hot-deformation [11], which is in agreement with the XRD results. Note that the remanent magnetization for hot-pressed magnets and hot-deformed magnets fabricated from nanocrystalline powders is almost the same as their counterparts processed from amorphous powders; however, the coercivity of HPM-A and HDM-A is higher than those of their counterparts processed from nanocrystalline powders. Hereafter, the microstructure characterization was carried out to clarify the relationship between microstructure and coercivity.

3.3.2 TEM study of melt-spun powders

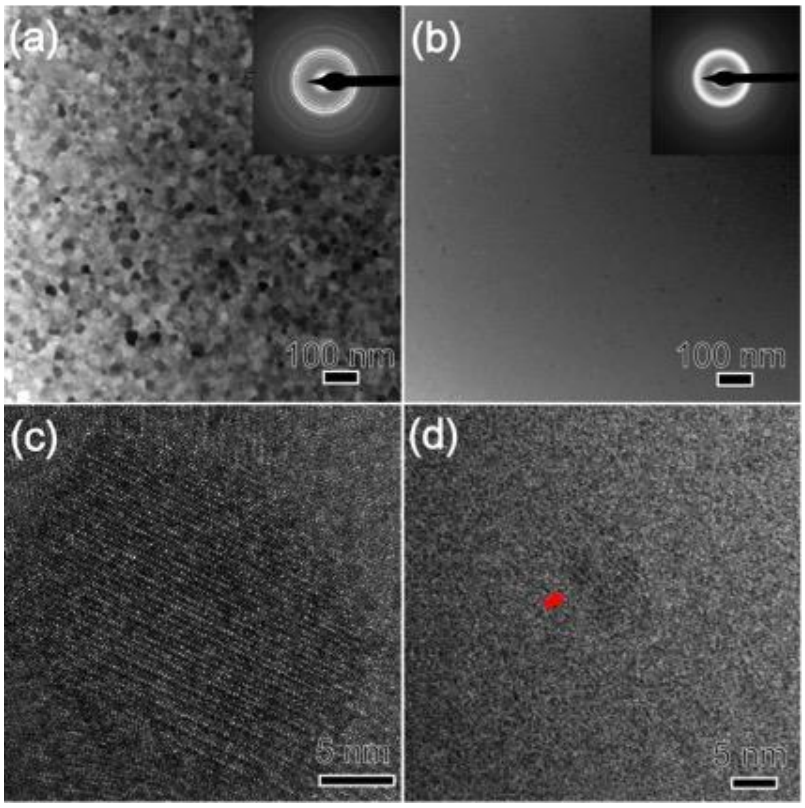

Figure 3. Low magnification TEM images (a) nanocrystalline and (b) amorphous powders; HRTEM images for (c) nanocrystalline and (d) amorphous powders. The inset images showed the SADPs.

Fig. 3 shows the detailed TEM images of nanocrystalline and amorphous melt-spun powders. Based on Fig. 3(a), the average grain size is calculated to be ~24.9 nm. The selected area diffraction

pattern (SADP) in the inset of Fig. 3(a) shows dense ring-type patterns, suggesting the grains are randomly oriented in the nanocrystalline powders. The high-resolution TEM (HRTEM) image shown in Fig. 3(c) presents that nanocrystals of around ~20 nm with equaxied grain shape. Fig. 3(b) shows an amorphous matrix, in which is embedded with ultrafine nanocrystallites with diameter of ~ 5 nm. Consequently, a typical diffused halo ring of diffraction pattern is obtained in the inset SADP of Fig. 3(b). The detailed HRTEM image presented in Fig. 3(d) shows nanometer-scale (~5 nm) primary $Nd_2Fe_{14}B$ nanocrystallite (shown by red arrow) with clear lattice fringes embedded in an amorphous matrix.

3.3.3 Detailed Microstructure characterization on hot-pressed magnets

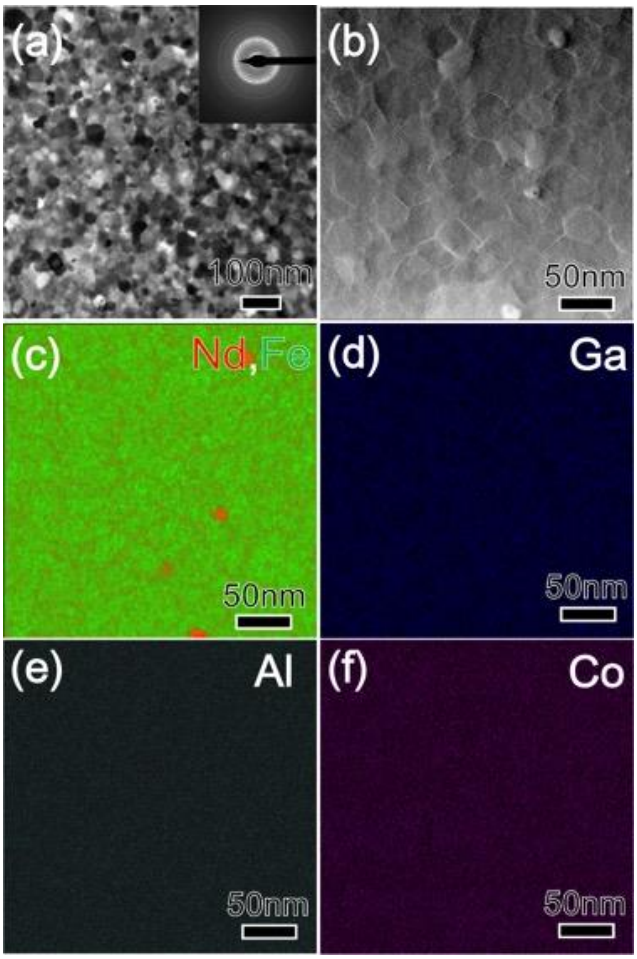

Figure 4. (a) low magnification TEM image and inset SADP, (b) HAADF image of HPM-C and EDS elemental maps for (c) Nd+Fe, (d) Ga, (e) Al and (f) Co from the same region as (b).

Fig. 4 shows the low magnification TEM and STEM-EDS images for hot-pressed magnets processed from nanocrystalline powders. In Fig. 4(a), equiaxed grains show spherical morphology, which is similar to that of melt-spun ribbons. This appears different from the grain shape reported by Liu *et al* [12], in which the elongated shape of grains of the 2:14:1 phase was observed in hot-pressed magnets, this discrepancy may result from higher hot-pressing temperature in ref. [12]. The grain size ranges from ~10 to ~70 nm and the mean grain size is estimated to be ~33.6 nm, which is slightly smaller than that (~ 50 nm) in conventional MQ2 magnets [13]. The inset ring-shaped SADP in Fig. 4(a) indicates that the isotropic nature of the microstructure with random distribution of *c*-axes of Nd-Fe-B grains. High-angle annular dark-field (HAADF) image and elemental mappings for Nd+Fe, Ga, Al, Co obtained from the same region are shown in Figs. 4(c)-(f), respectively. The contrast in the HAADF image indicates a heavier element, i.e. Nd is enriched in grain boundaries. This is confirmed by the EDS map in Fig. 4(c), where Nd is segregated in some areas as indicated by red spots. Besides, the thin and blurry grain boundaries can be also observed because of traceable segregation of Nd and depletion of Fe in the intergranular phase. Figs. 3(d)-(f) imply that the distribution of Co, Ga and Al are much more homogeneous compared to Nd and Fe.

To carry out comparative studies, the bright field TEM and the STEM-EDS images for HPM-A is shown in Fig. 5. As seen in Fig. 5(a), equiaxed grains with random *c* axes distribution have a wide grain size distribution ranging from ~10 to ~100 nm and the average grain size is measured to be ~ 42.6 nm, which is larger than that (33.6 nm) of hot-pressed magnet processed from nanocrystalline powders. It is well-known that grain growth is occured with the shrinking of volume fraction of grain boundaries, the volume fraction of grain boundaries in HPM-A containing bigger grains is supposed to be smaller than that in HPM-C. Considering same Nd concentration in these two hot-pressed samples, Nd should be more strongly segregated in grain the boundaries of the HPM-A sample. To confirm this, the EDS mappings of are shown in Figs. 5(c)-(f). The elemental mapping indicated in Fig. 5(c) shows that Nd is more concentrated in the triple junctions and the contrast from the grain boundary phases is stronger and more clear in HPM-A as compared to those in HPM-C shown in Fig. 4(c), implying that the higher Nd concentration can be found in this sample than that in HPM-C. Consequently, weaker intergrain exchange coupling is expected in HPM-A, which is considered to enhance the coercivity [14]. In Fig. 5(d), Ga is observed to segregate in some area where Nd is also concentrated. The elements of Co and Al have

homogeneous distribution in this sample, which is similar to their distribution behaviors in HPM-C.

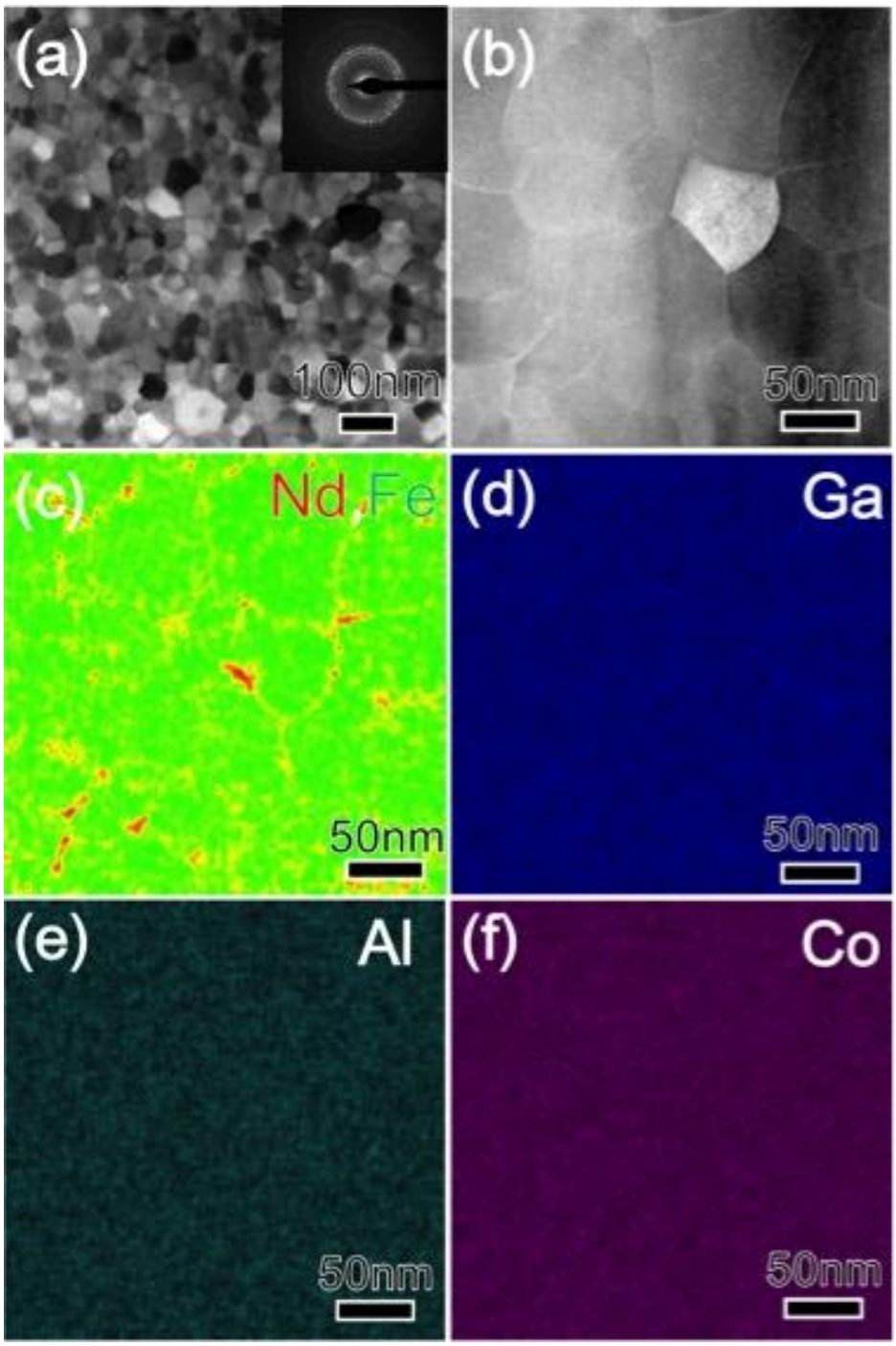

Figure 5. (a) low magnification TEM image and inset SADP, (b) HAADF image of HPM-A and EDS elemental maps for (c) Nd+Fe, (d) Ga, (e) Al and (f) Co from the same region as (b).

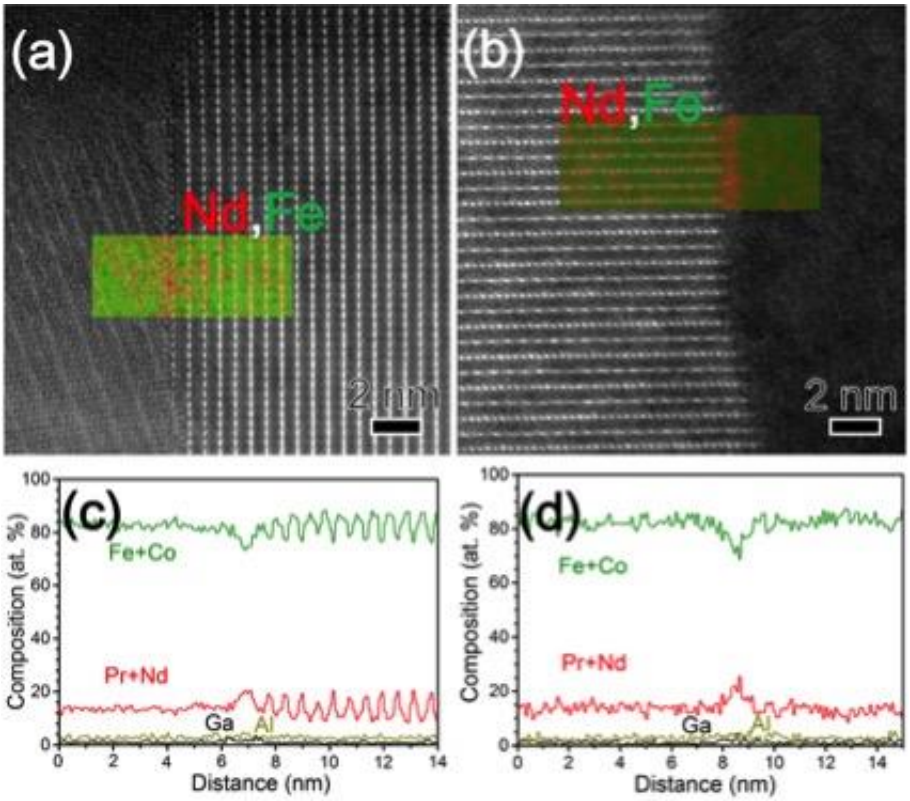

Fig. 6. High-resolution (HR) STEM images and inset EDS map of Nd+Fe of intergranular phases in (a) HPM-C and (b) HPM-A; (c) and (d) line scan chemical profiles taken across the grain boundary phase in (a) and (b), respectively.

To further confirm the composition of the intergranular phase, high-resolution (HR) STEM-HAADF and EDS analyses were performed on the HPM-C and HPM-A samples. Fig. 6 shows the HR-STEM-HAADF images and compositional profiles taken from the interface of two $Nd_2Fe_{14}B$ crystals in the HPM-C and HPM-A samples. As seen in Fig. 6(a), an amorphous Nd-rich phase is observed in the grain boundary in HPM-C. The thickness of grain boundary phase gradually decreases along the grain boundary and two Nd-Fe-B crystals physically contact with each other at the end of grain boundary phase, resulting in exchange coupling between the two Nd-Fe-B grains. Consequently, discontinuous grain boundary phases is documented in Fig. 4(c). The inset EDS map of Nd+Fe in Fig. 6(a) reveals that Nd is traceably segregated in the grain boundary phase. To confirm this, the compositional profile taken across this grain boundary phase is shown in Fig. 6(c), in which indicates ~20.1 at.% of RE concentration is obtained in this grain boundary phase. Fig. 6(b) shows a high resolution TEM image obtained from the interface of two grains in HPM-

A. A typical grain boundary microstructure with a thin grain boundary phase is observed in HPM-A. Fig. 6(d) shows the chemistry of this grain boundary phase. It implies that this grain boundary phase is enriched with ~25 at.% of RE concentration. This value is slightly higher than the RE concentration in the grain boundary phase of HPM-C shown in Fig. 6(c). Hence, stronger and clearer contrast from grain boundary phase can be detected in Nd+Fe EDS mapping as shown in Fig. 5(c). Consequently, the stronger exchange decoupling between 2:14:1 phases can be obtained in HPM-A and the coercivity is thereby enhanced in this sample.

3.3.4 Detailed Microstructure characterization on hot-deformed magnets

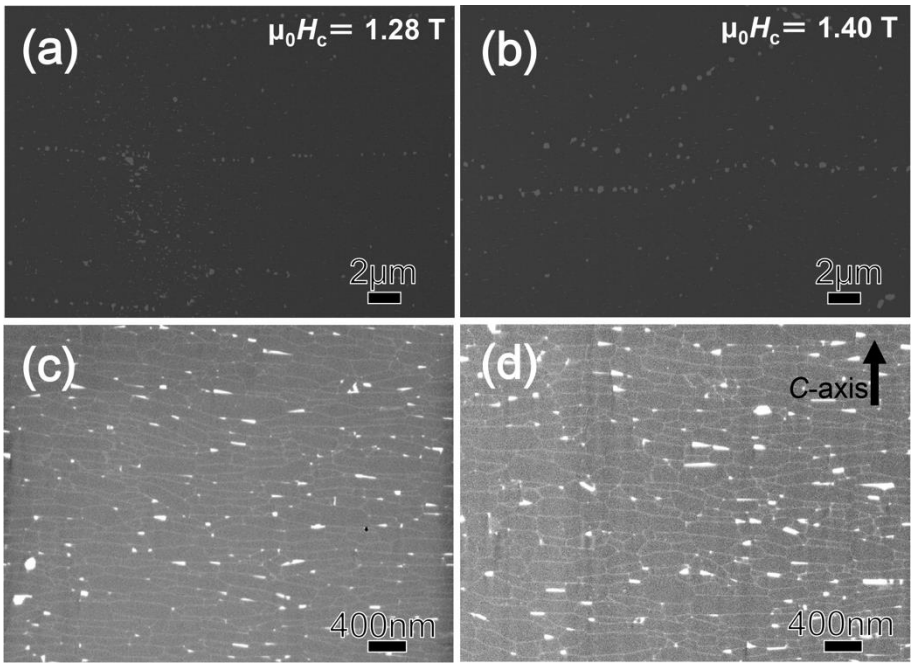

Figure 7. Low magnification back scattered SEM images of (a) HDM-C and (b) HDM-A; Magnified back scattered SEM images of (c) HDM-C and (d) HDM-A.

Fig. 7 shows the microstructure of HDM-C and HDM-A. Figs. 7 (a) and (b) show overall microstructures for hot-deformed magnets processed from crystalline and amorphous melt-spun ribbons, respectively. In Figs.7 (a-b), brightly imaging phase is corresponding to NdO_x formed on the interface of powders and the phase with the grey contrast is $Nd_2Fe_{14}B$ grains [4,14]. The magnified BS SEM images taken from HDM-C and HDM-A are shown in Fig. 7(c) and (d),

respectively. It is seen that the *c*-axes of platelet-like grains are parallel to applied stress direction after hot-deformation and the $Nd_2Fe_{14}B$ grains are well enveloped by thin grain boundary phase with bright contrast. The grain size of each sample is statistically calculated from these two BSE SEM images. In HDM-A, the average size of $Nd_2Fe_{14}B$ grains along the *c*-plane (D_c) is measured to be ~343 nm while the size in the direction perpendicular to the *c*-plane (D_{ab}) is calculated to be ~132 nm. The values of D_c and D_{ab} are measured to be ~375 nm and 106 nm in HDM-C sample. Consequently, the grains in Fig. 7(d) show more feature of rounded shape compared to those in Fig. 7(c), indicating the average aspect ratio (3.54) of grains in HDM-C is bigger than that (2.60) in HDM-A. This may be resulted from different grain size in hot-pressed precursors. The other different feature between these two figures is that the contrast of Nd-rich grain boundary phase is brighter and clearer in Fig. 7(d), especially in the side planes of the elongated grains, which suggests higher Nd concentration in side plane in Fig. 7 (d). This will be demonstrated later. Since the different grain sizes documented in Figs. 7(c-d), the different areal fraction of the grain boundary phases in HDM-C and HDM-A is also documented in table 1, in which is shown to be ~2.58% and ~2.27 %, respectively. The microstructural differences between HDM-C and HDM-A are summarized in detail in table 1.

Table 1 Size and aspect ratio (AR) of grains and areal fraction of grain boundary (AFoGB) in hot-deformed samples.

samples	D_c	D_{ab}	AR of Grains	AFoGB phases
HDM-A	343 nm	132 nm	2.60	2.27%
HDM-C	375 nm	106 nm	3.54	2.58%

Fig. 8 and Fig. 9 show the EDS analyses of HDM-C and HDM-A, respectively. As seen in the STEM-HAADF images (Fig. 8(a) and Fig. 9(a)), the bright contrast in the HAADF images indicates the heavier elements, i.e. Nd are enriched in grain boundaries, which can be further confirmed by EDS maps of Nd in Fig. 8(b) and Fig. 9(b), where Nd is obviously segregated in triple junctions and grain boundaries. In addition, grain size in HDM-A is larger than that in HDM-C. This is consistent with SEM results as shown in Fig. 7. It is shown in table 1 that the areal fraction of grain boundary phase in HDM-C is bigger than that in HDM-A because of coarser grains in HDM-A. Considering the same RE concentration in these two hot-deformed samples, higher RE concentration in grain boundaries, especially in side-plane grain boundaries can be

observed in HDM-A. Hence, it is seen in Fig. 9(b) and Fig. 9(c), the network of grain boundary phases is observed to be more continuous in Nd and Fe maps of HDM-A sample, which is consistent with BS SEM observations in Fig. 7. Ga is also found enriched in these triple junctions in these two hot-deformed samples. The Ga enrichment is reported to improve wettability of Nd-Ga-rich intergranular phase as well as coercivity due to the fact that better magnetic isolation between 2:14:1 phases can be yielded [14–16].

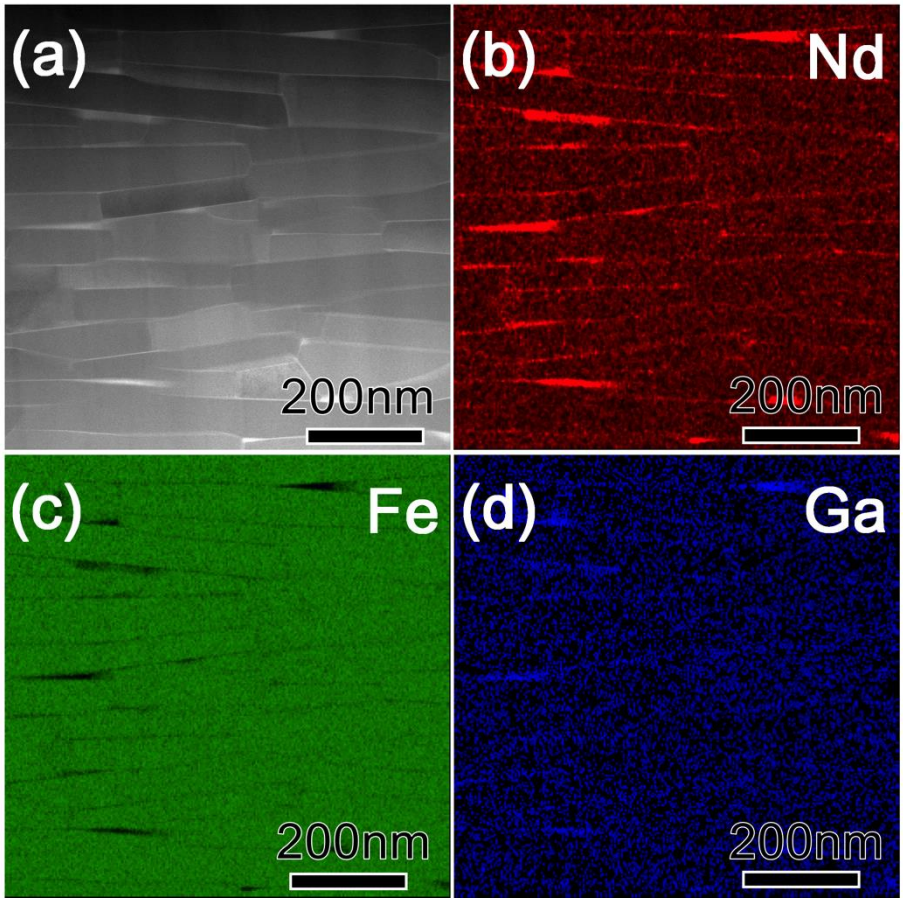

Figure 8. (a) low magnification HAADF image and EDS maps in HDM-C.

Fig. 10 shows the HR-TEM images and chemical compositions obtained from the *c*-plane grain boundary between two 2:14:1 grains in hot-deformed magnets. Figs. 10(d-f) show the chemical compositions in *c*-plane grain boundary phases of HDM-C obtained from inset EDS maps of Figs. 10(a-c), respectively. The superimposed Nd+Fe maps show that the Nd is enriched with depletion of Fe in those *c*-plane intergranular phases. ~50.2 at.%, ~42.5 at.% and ~35.2 at.% of RE (Nd+Pr) concentrations are obtained in these three typical *c*-plane intergranular phases of

HDM-C, while the concentrations of ferromagnetic elements (Fe+Co) were accordingly determined to be ~39.6 at.%, ~50.7 at.% and 53.7 at.% in these three intergranular phases of HDM-C.

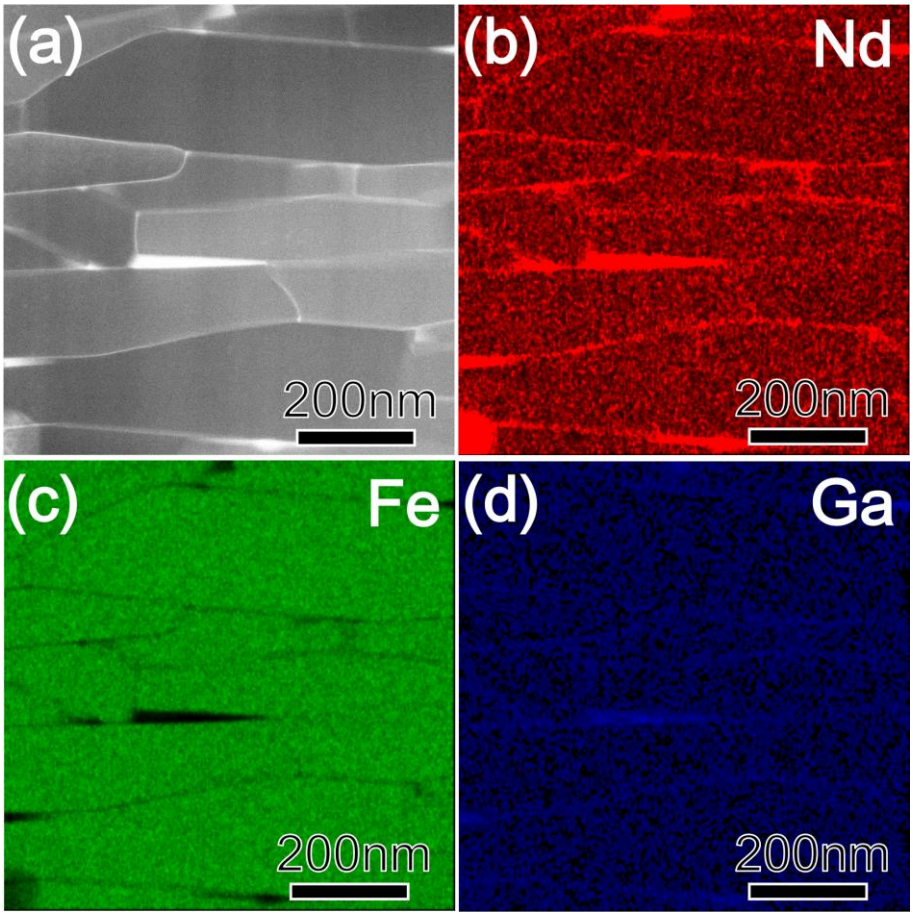

Figure 9. (a) low magnification HAADF image and EDS maps in HDM-A.

Figs. 10(g-i) show the line-scan compositional profiles of three *c*-plane grain boundary phases in HDM-A obtained from superimposed inset EDS maps of Fig. 10(j-l), respectively. It is shown that ~62.9 at.%, ~50.2 at.%, ~50.4 at.% for RE (Nd+Pr) concentrations and ~22.4 at.%, ~41.6 at.%, ~41.4 at.% for Fe+Co concentrations were found in these three intergranular phases, considerably higher RE concentrations in grain boundary phases of HDM-A as compared to those in HDM-C.

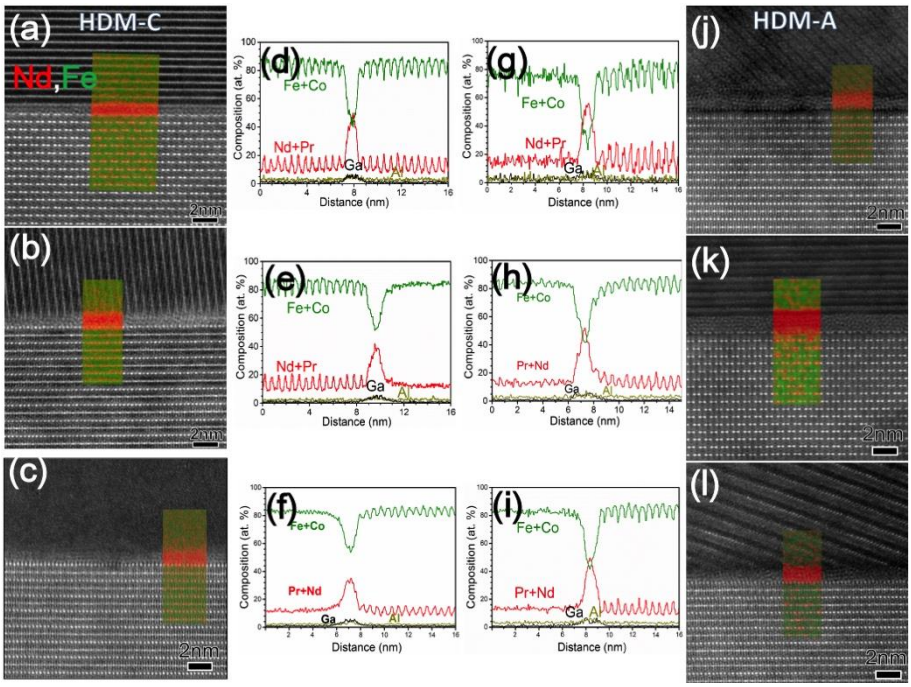

Figure 10. HR-STEM images and inset EDS maps of Nd+Fe taken from *c*-plane interface of HDM-C (a-c) and HDM-A (j-l); (d-f) and (g-h) line scan profiles taken across the interface in (a-c) and (j-l), respectively.

The compositional information in side-plane intergranular phases are also investigated and shown in Fig. 11. Fig. 11(a-c) shows intergranular phases with ~1nm thickness in *ab*-plane grain boundary of HDM-C. In comparison, the weaker intensity of Nd from Nd+Fe EDS map in Fig. 11(a-c) as compared to those in *c*-plane intergranular phases (Fig. 10(a-c)), indicating relatively lower Nd concentration enriched in side-plane grain boundary phases, which is consistent with other work [10]. Fig. 11(d-f) shows the chemical compositions in side-plane grain boundary phases in HDM-C, in which RE concentrations in these side-plane intergranular phase are measured to be ~28.6 at.%, ~29.5 at.% and ~33.1 at.%, while ~61.9 at.%, ~67.1 at.% and ~56.4 at.% of Fe+Co found in these grain boundary phases. Concerning side-plane intergranular phases in HDM-A, the thicker amorphous intergranular phase with more clear contrast is observed in Fig. 11(j-l) and inset EDS maps of Nd+Fe show stronger intensity from Nd as compared to those in Fig. 11(a-c), suggesting relatively higher Nd enriched in these three grain boundary phases, which is further confirmed by the compositional analyses in Fig. 11(g-i), in which RE concentrations are determined to be ~41.3 at.%, ~43.4 at.% and ~35.8 at.%, while ~52.1 at.%, ~42.1 at.%, ~57.5 at.%

of Fe+Co concentrations were obtained in these typical side-plane grain boundary phases of HDM-A.

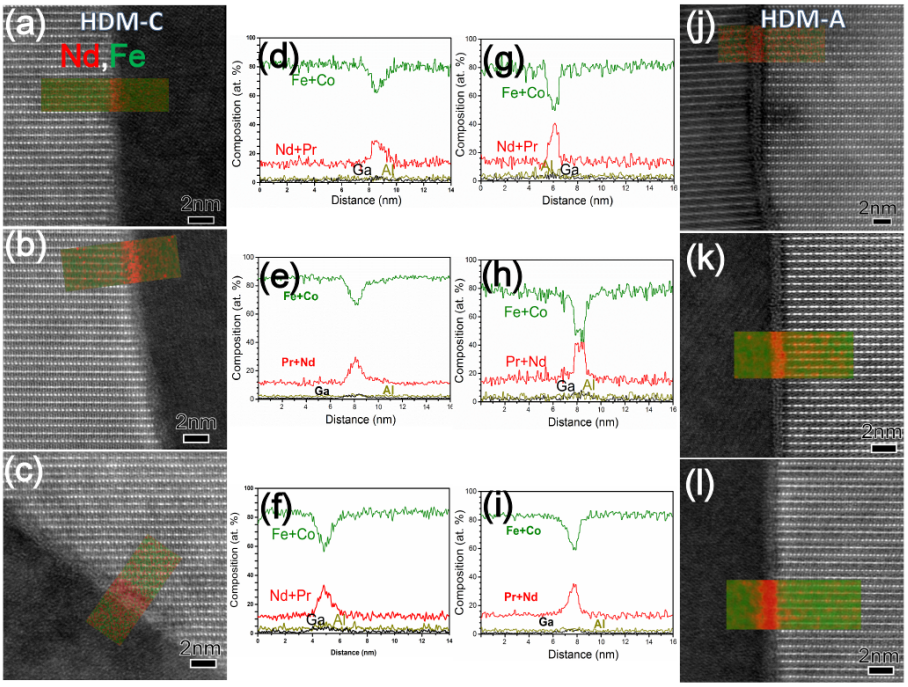

Figure 11. HR-STEM images and inset EDS maps of Nd+Fe taken from side-plane interface of HDM-C (a-c) and HDM-A (j-l); (d-f) and (g-h) line scan profiles taken across the interface in (a-c) and (j-l), respectively.

To be more statistical, at least five compositions of grain boundary phases are obtained to get the chemical compositions in *c*-plane and side-plane intergranular phases in hot-deformed magnets. The results are summarized in Table 2. The RE concentration in *c*-plane grain boundary phases of HDM-C is close to ~39.8 at.% and RE concentration decreases to ~28.2 at.% in the side-plane intergranular phases of HDM-C. The considerable difference in RE concentration between *c*-plane and side-plane intergranular phases is documented. In a typical sintered magnet, the *c*-plane grain boundary phase has a crystalline structure highly enriched with Nd, while side-plane grain boundary phase has an amorphous structure with relatively low Nd concentration [17,18]. In this work, both *c*-plane and side-plane grain boundary phases appear to be amorphous structure but considerable difference in RE concentration between *c*-plane and side-plane intergranular phases. Concerning the RE concentration in the grain boundary phases of HDM-A, ~50.2 at.% and ~34.5 at.% of RE concentrations are found in the *c*-plane and side-plane intergranular phases,

respectively. As compared to the RE concentrations of grain boundary phases in HDM-C, the RE concentration in both *c*-plane and side-plane intergranular phases are considerably higher. This is resulted from smaller areal fraction of grain boundaries in HDM-A containing bigger grains. The pinning force against reversed magnetic domain wall displacement in process of magnetization reversal has been strengthened by higher RE concentration in the grain boundary phases [4,14]. As a result, a higher coercivity in HDM-A can be yielded.

Table 2 Average compositions and width (*d*) of *c*-plane and side-plane grain boundary (GB) phases in hot-deformed samples.

Samples	*c*-Plane GB phases			side-Plane GB phases		
	Pr+Nd	Co+Fe	*d*	Pr+Nd	Co+Fe	*d*
HDM-C	39.8 at.%	51.3 at.%	0.9 nm	28.2 at.%	64.5 at.%	0.88 nm
HDM-A	50.2 at.%	40.1 at.%	1.21 nm	34.5 at.%	57.8 at.%	1.07 nm

3.3 Discussion

There are remarkable differences in microstructure, such as grain size and number density of primary crystals, between amorphous and nanocrystalline powders are observed in Fig. 3. In the amorphous ferromagnets, the low coercivity is resulted from net zero-magnetocrystalline anisotropy [19–21]. Except a few nanocrystallites with size of ~5 nm as shown in Fig. 3(d), the nature of amorphous matrix indicate that the magnetocrystalline anisotropy is average out, which can be explained in detail by the random anisotropy model. In contrast, ultrafine grains with an average grain size of ~24.9 nm was documented in the microstructure shown in Fig. 3(a), the grain size is much larger than the exchange length (l_{ex}~1.9 nm) of the $Nd_2Fe_{14}B$ phase, meaning that the magnetocrystalline anisotropy can't be averaged out. So, the coercivity of amorphous powders is much smaller than that of crystalline melt-spun ribbons.

After hot-pressing, it is shown XRD patterns that both of hot-pressed magnets are fully crystallized because of low crystallization temperature of $Nd_2Fe_{14}B$. The grain sizes of HPM-C and HPM-A are calculated from TEM results to be ~33.6 and 42.6 nm, respectively. Which indicates that the grain size in hot-pressed magnets processed amorphous powders is larger than that in hot-pressed counterpart processed from nanocrystalline powders. This is resulted from the remarkable difference in number density of primary Nd-Fe-B nanocrystals. In Specific, large number density of Nd-Fe-B nanocrystals homogeneously distributed in the nanocrystalline melt-spun powders, while the number density of crystals in amorphous precursors is extremely small. Grain size in hot-pressed magnets is depended on competition between number density of primary nanocrystallites and grain growth. These primary nanocrystals in amorphous melt-spun powders serve a role as nucleation sites in crystallization during the following hot-pressing process, indicating the number density of nucleus is extremely small and grain growth is thus favorable in the amorphous powders during hot-pressing. In addition, the nucleation activation energy E_n for $Nd_2Fe_{14}B$ nanocrystals is determined to be ~ 0.9 eV, which is larger than grain growth activation energy E_g ~0.5 eV, respectively [22], indicating that grain growth of $Nd_2Fe_{14}B$ is kinetically favorable in amorphous melt-spun powders during hot-pressing process. As a result, larger grain size is obtained in HPM-A.

As far as the coercivity in the hot-pressed magnets is concerned, the microstructure-dependent coercivity is determined by grain size, chemical composition of grain boundary phase and aspect ratio of grains. The effect of grain shape on coercivity is not taken into consideration because of isotropic nature in hot-pressed magnets. It is shown in Figs. 3(a) and 4(a) that grain size ~33.6 nm in HPM-C is smaller than that (~42.6 nm) in HPM-A. The strengthened exchange interaction between smaller grains resulted in a decrease in coercivity from ~2.0 T to 1.2 T with reducing grain size from ~50 nm to 15 nm reported in [23-25]. In addition, the less continuous grain boundary phase formed in HPM-C as indicated in Fig. 3(c) and lower Nd concentration in grain boundary phase in Fig. 5 (c), the exchange coupling between 2:14:1 phases is hence stronger in HPM-C and lower coercivity is obtained. It should be noted that the similar tendency of coercivity depending on grain size is found in hot-pressing nanocrystalline powders that with grain size increasing from ~24.9 nm in nanocrystalline powders to ~33.6 nm in HPM-C, the coercivity is enhanced from ~1.27 T to ~1.46 T as shown in Fig. 2.

As for the coercivity in hot-deformed magnets, the process of magnetization reversal occurs as follow: the reversed magnetic domain is initially nucleated at nucleation site with lowered magnetocrystalline anisotropy field and followed by propagation of reversed magnetic domain, some imhomogeneous sites, such as grain boundaries, act as pinning site to stop further propagation of reversed magnetic domain, after depinning by further increase of inverse field, the reversed magnetic domain will easily propagate through the whole magnet. The micromagnetic simulation results [4,14] have unambiguously demonstrated that the nucleation field for reversed domain and the pinning force against reversed domain can be strengthened by an increase in RE concentration in the grain boundary phases. Here, the average RE concentration in the grain boundary phases increases from ~39.8 at.% in HDM-C to 50.2 at.% HDM-A, which are slightly higher than those in sintered magnets and comparable to those of the hot-deformed magnets with 14 at.% Nd [14,26]. Weaker exchange coupling between two grains along *c*-axis in HDM-A resulted from higher RE concentration in the *c*-planes of HDM-A than that of HDM-C leads to in an enhancement in coercivity by producing hot-deformed magnets from amorphous powders. The low RE concentration in the *ab*-plane intergranular phases in both hot-deformed magnets is considered as a barrier to further increase coercivity in hot-deformed magnets, which is demonstrated by micromagnetic simulations [4]. One reason for anisotropic distribution of RE in *c*-plane and side-plane grain boundary is considered to be anisotropic grain shape in hot-deformed magnets. Here, it is found that the aspect ratio was reduced from ~3.54 in HDM-C to ~2.6 in HDM-A, this may reduce the difference in interfacial energy between *ab* plane and *c* plane. Consequently, the RE concentration in *ab*-plane grain boundary phases is increased from ~28.2 at.% in HDM-C to ~34.5 at.% in HDM-A, which also contributes to the higher coercivity in HDM-A.

It is shown in table 1 that the aspect ratio of grains was reduced from 3.54 to 2.60 by producing hot-deformed magnets from amorphous melt-spun ribbons. In order to clarify effect of grain shape on coercivity, the plots of H_c/M_s against H_A/M_s of the HDM-C and HDM-A are shown in Fig. 12. In general, the coercivity can be phenomenologically expressed by $H_c(T)= \alpha H_A(T)-N_{eff}M_s(T)$; where H_A and M_s are the anisotropy field and saturation magnetization, respectively, α shows the lowered anisotropy field resulted from defects at grain boundaries, and N_{eff} known as an effective demagnetization factor [27], reflecting local demagnetization field. α and N_{eff} can be determined by plotting H_c/M_s against H_A/M_s followed by fitting the data linearly. It is shown in Fig. 12 that α was measured to be 0.53 in HDM-C and this value increases to 0.58 by producing

hot-deformed magnets from amorphous powders (HDM-A). Larger α value for HDM-A is resulted from the smaller areal fraction of grain boundaries shown in table1. N_{eff} were calculated to be ~1.27 for HDM-C and ~1.36 for HDM-A. The average thickness of grain boundary phases in both hot-deformed samples indicated in table 2 is smaller than exchange length ~ 1.9 nm, suggesting grains are exchange coupled in HDM-C and HDM-A. Even though the aspect ratio of grains is smaller in HDM-A, the contribution of smaller aspect ratio to coercivity is nullified by strong exchange coupling between 2:14:1 grains. Moreover, the bigger grains in HDM-A shown in table 1 and Fig. 7 results in bigger N_{eff} [10]. Consequently, N_{eff} for HDM-A containing bigger grains shows a larger value than that for HDM-C.

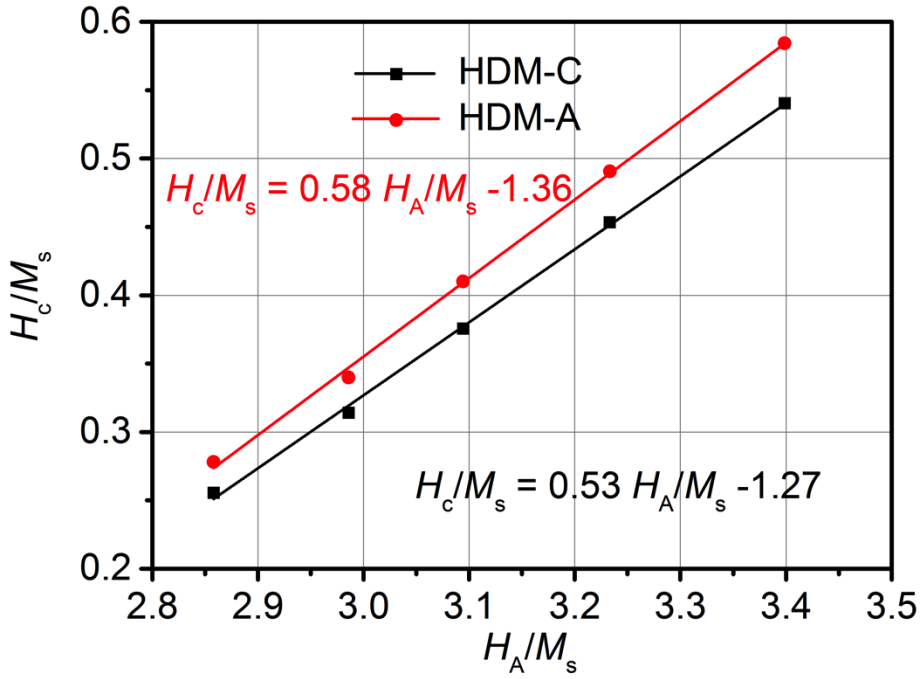

Figure 12. Dependence of H_c/M_s on H_a/M_s of the hot-deformed samples. The slope and intercept of linearly fitted plots are determined to be the parameters α and N_{eff}, respectively.

3.4 Conclusion

To explore the optimum processing condition of hot-deformation, the coercivities and microstructures of hot-deformed magnets produced from amorphous and nanocrystalline powders have been systematically studied. The coercivity of the hot-deformed magnets produced from nanocrystalline melt-spun ribbons was shown to be ~1.28 T, this value increased to ~1.4 T in the

hot-deformed counterpart produced from an amorphous melt-spun powders. Futher microstructure characterization indicated that higher concentration of rare earth elements was obtained in the hot-deformed magnet processed from the amorphous melt-spun ribbons because of bigger grain size and smaller resultant areal fraction of grain boundaries in this sample. This leads to a strengthened pinning force against reversed magnetic domain wall displacement in process of magnetization reversal, and the higher coercivity can thus be yielded in hot-deformed magnets produced from amorphous melt-spun ribbons.

Reference

[1] R. Lee, E. Brewer, N. Schaffel, IEEE Trans. Magn. 21 (1985) 1958–1963.

[2] R.W. Lee, Appl. Phys. Lett. 46 (1985) 790–791.

[3] H. Sepehri-Amin, T. Ohkubo, T. Nishiuchi, S. Hirosawa, K. Hono, Scr. Mater. 63 (2010) 1124–1127.

[4] H. Sepehri-Amin, T. Ohkubo, S. Nagashima, M. Yano, T. Shoji, A. Kato, T. Schrefl, K. Hono, Acta Mater. 61 (2013) 6622–6634.

[5] L. Liu, H. Sepehri-Amin, T. Ohkubo, M. Yano, A. Kato, N. Sakuma, T. Shoji, K. Hono, Scr. Mater. 129 (2017) 44–47.

[6] L. Liu, H. Sepehri-Amin, T. Ohkubo, M. Yano, A. Kato, T. Shoji, K. Hono, J. Alloys Compd. 666 (2016) 432–439.

[7] K. Loewe, D. Benke, C. Kübel, T. Lienig, K.P. Skokov, O. Gutfleisch, Acta Mater. 124 (2017) 421–429.

[8] T. Akiya, J. Liu, H. Sepehri-Amin, T. Ohkubo, K. Hioki, A. Hattori, K. Hono, Scr. Mater. 81 (2014) 48–51.

[9] X. Tang, R. Chen, W. Yin, J. Wang, X. Tang, D. Lee, A. Yan, Appl. Phys. Lett. 102 (2013) 072409.

[10] J. Liu, H. Sepehri-Amin, T. Ohkubo, K. Hioki, A. Hattori, T. Schrefl, K. Hono, Acta Mater. 82 (2015) 336–343.

[11] Y. Matsuura, J. Hoshijima, R. Ishii, J. Magn. Magn. Mater. 336 (2013) 88–92.

[12] J. Liu, H. Sepehri-Amin, T. Ohkubo, K. Hioki, A. Hattori, K. Hono, J. Appl. Phys. 115 (2014) 17A744.

[13] Y.I. Lee, G.Y. Huang, S.T. Chang, C.W. Shih, W.C. Chang, H.W. Chang, Y.J. Chen, IEEE Magn. Lett. 8 (2017) 1–4.

[14] J. Liu, H. Sepehri-Amin, T. Ohkubo, K. Hioki, A. Hattori, T. Schrefl, K. Hono, Acta Mater. 61 (2013) 5387–5399.

[15] H. Sepehri-Amin, W.F. Li, T. Ohkubo, T. Nishiuchi, S. Hirosawa, K. Hono, Acta Mater. 58 (2010) 1309–1316.

[16] I. Ahmad, H.A. Davies, R.A. Buckley, Mater. Lett. 20 (1994) 139–142.

[17] T.T. Sasaki, T. Ohkubo, Y. Une, H. Kubo, M. Sagawa, K. Hono, Acta Mater. 84 (2015) 506–514.

[18] T.T. Sasaki, T. Ohkubo, K. Hono, Acta Mater. 115 (2016) 269–277.

[19] R. Harris, M. Plischke, M.J. Zuckermann, Phys. Rev. Lett. 31 (1973) 160–162.

[20] E. Callen, Y.J. Liu, J.R. Cullen, Phys. Rev. B 16 (1977) 263–270.

[21] R. Alben, J.J. Becker, M.C. Chi, J. Appl. Phys. 49 (1978) 1653–1658.

[22] W. Li, L. Li, Y. Nan, Z. Xu, X. Zhang, A.G. Popov, D.V. Gunderov, V.V. Stolyarov, J. Appl. Phys. 104 (2008) 023912.

[23] A. Manaf, R.A. Buckley, H.A. Davies, M. Leonowicz, J. Magn. Magn. Mater. 101 (1991) 360–362.

[24] A. Manaf, R.A. Buckley, H.A. Davies, J. Magn. Magn. Mater. 128 (1993) 302–306.

[25] T. Schrefl, J. Fidler, H. Kronmüller, Phys. Rev. B 49 (1994) 6100–6110.

[26] W.F. Li, T. Ohkubo, K. Hono, Acta Mater. 57 (2009) 1337–1346.

[27] H. Kronmüller, Phys. Status Solidi B 130 (1985) 197–203.

Chapter 4: Suppression of non-orientated grains in ho-deformed magnets by Nb doping

4.1 Introduction

Since the average grain size of hot-deformed magnets (~400 nm) is an order of magnitude smaller than that of sintered magnets, hot-deformed magnets have greater potential to achieve high-coercivity and better thermal stability of coercivity even without heavy rare earth elements [1]. There are two distinguishable regions in the typical microstructure of the hot-deformed magnets: one is well-textured platelet-like grains within ribbons and the other is coarse non-aligned grains (surface crystallites) at the interfaces of stacked ribbons [2]. The former one contributes to high remanent magnetization as well as high energy density in hot-deformed magnets and the latter one causes reduced remanent magnetization and lower nucleation field. Extensive attempts have been made to achieve both higher coercivity and remanence in the hot-deformed magnets.

Recently, Mouri *et al* [3]reported that these coarse and isotropic grains could be suppressed by two-stage hot-deformation, the enhancement of coercivity with degradation in remanent magnetization could be hence obtained. Blending WC hard nanoparticles with MQU-F powders was also reported to suppress the coarse grain growth due to the compressive stress induced by localized WC nanoparticles on the surface of ribbons, thus resulted in increase of both remanence and coercivity in hot-deformed magnets [4]. Grain boundary diffusion is an effective method to increase the coercivity in hot-deformed magnets, but the enhancement of coercivity was always achieved at the expense of degradation of remanent magnetization. Sepehri-Amin *et al* [5–9] reported a substantial enhancement in coercivity with a considerable degradation in remanent magnetization because of the larger volume fraction of RE-rich intergranular phases and the deterioration of (001)-texture. To minimize the remanence loss after grain boundary diffusion, Akiya *et al* [10] proposed that constraining the expansion of volume along the *c*-axis direction during the eutectic diffusion process can achieve the high coercivity (~1.9 T) with a remanence

keeping ~1.35 T. Note that the existence of coarse non-aligned grains in the diffusion-processed samples, which is inherited from the hot-deformed magnets, appears to inhibit further increase of remanent magnetization. Therefore, the development of hot-deformed magnets with uniform microstructure is of critical importance for achieving both high-coercivity and high remanent magnetization in hot-deformed magnets. Up to dates, it should be noteworthy that all the hot-deformed magnets were produced from melt-spun ribbons and these localized non-aligned surface crystallites should be closely related to inhomogeneous microstructure in the melt-spun ribbons. By tuning the composition of the ribbons, it should be feasible to get rid of the surface crystallites to achieve uniform microstructures in melt-spun ribbons and hot-deformed magnets. Trace additions of high melting temperature transition elements such as Zr and Nb were reported to be effective for refining the grain size of melt-spun Nd-Fe-B alloys [11–15]. In this paper, we investigated the influence of Nb addition on the magnetic properties and microstructures of hot-deformed magnets to elucidate the role of Nb on grain refinement and to examine if trace addition of Nb can influence the coarse surface crystallites on the ribbon interface in the hot-deformed magnets.

4.2 Experimental procedure

Alloy ingots with the composition of $Nd_{12.83}Fe_{76.7}Co_{4.50}Ga_{0.53}B_{5.44}$ (at.%), $Nd_{12.83}Fe_{76.5}Co_{4.50}Ga_{0.53}Nb_{0.2}B_{5.44}$ (at.%) (hereafter, 0.2Nb-doped sample), $Nd_{12.83}Fe_{76.1}Co_{4.50}Ga_{0.53}Nb_{0.6}B_{5.44}$ (at.%) (hereafter, 0.6Nb-doped sample) and $Nd_{12.83}Fe_{76.3}Co_{4.50}Ga_{0.53}Nb_{0.2}$ $Nb_{0.2}B_{5.44}$ (at.%) (hereafter, 0.2Nb0.2Cu-doped sample) were produced by induction melting constituent elements with high purity. The ingots were subjected to melt-spinning with a wheel speed of 30 m/s under Ar protection. Subsequently, the hot-pressed magnets were obtained from compacting the melt-spun ribbons at 650 °C under 400 MPa in vacuum, followed by hot-deformation at 850°C until 75% height reduction was achieved. The magnetic properties were measured using a superconducting quantum interface device vibrating sample magnetometer (SQUID-VSM). The density values of the hot-deformed samples were measured by Gas Displacement Pycnometry System (AccyPyc II 1340 Pycnometer) with helium as the inert gas. The microstructures were studied by a scanning electron microscope (SEM), and a scanning transmission electron microscope (STEM). Three-dimension atom probe (3DAP) was performed on a locally build laser-assisted three-dimensional atom probe under ultrahigh vacuum

in a flux range of 0.003–0.01 atom per pulse using a femtosecond Yb:KGd $(WO_4)_2$ laser with a third harmonic generator (λ = 343 nm) and a laser power of 0.1 μJ pulse^{-1}.

4.3 Results

4.3.1 Magnetic properties in Nb-free and Nb-doped hot-deformed magnets

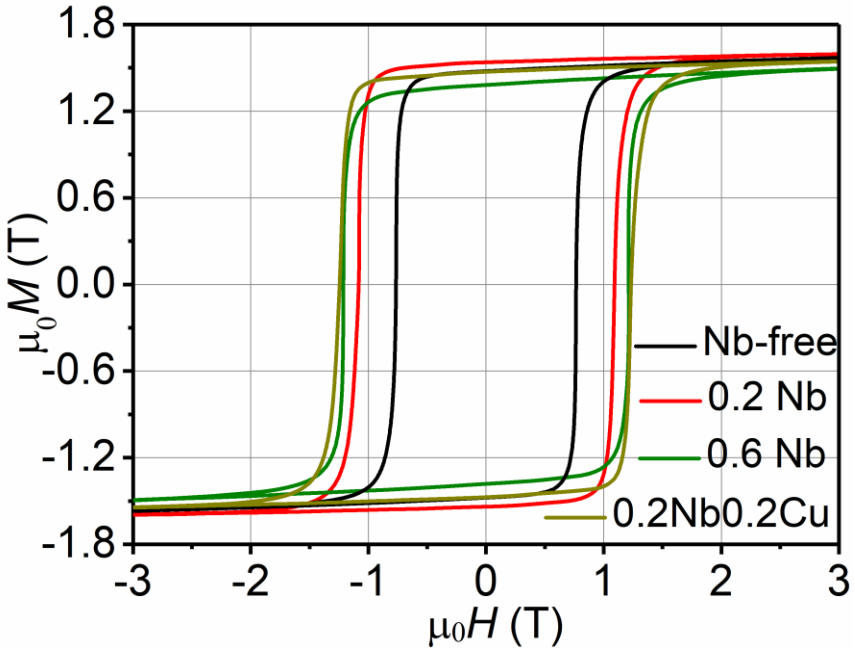

Fig. 1. Hysteresis loops for Nb-free, 0.2 Nb-doped and 0.6 Nb-doped hot-deformed magnets.

Table 1. Magnetic properties of hot-deformed magnets

Samples	$\mu_0 H_c$ (T)	$\mu_0 M_r$ (T)	$\mu_0 M_r/\mu_0 M_s$
Nb-free	0.75	1.45	0.91
0.2Nb-doped	1.04	1.54	0.96
0.6Nb-doped	1.21	1.36	0.87
0.2Nb0.2Cu-doped	1.24	1.45	0.91

Fig. 1 and table 1 shows the magnetic properties of Nb-free and Nb-doped hot-deformed Nd-Fe-B magnets. The coercivity of ~ 0.75 T was obtained with remanent magnetizaton of ~ 1.45 T in the Nb-free hot-deformed magnet. By the 0.2 at.% addition of Nb, the coercivity and remanent

magnetizations were increased to ~1.04 T and ~1.54 T, respectively. Even though the coercivity of Nb-doped sample is not so large, high remanent magnetization makes this sample as a competent starting sample for applying the eutectic diffusion process. With further increasing Nb doping to 0.6 at.%, the coervivity further increases to 1.21 T while the remanent magnetization is reduced to 1.36 T. By co-doping of 0.2 at.% Nb and 0.2 at.% Cu, the coercivity of sample is increased to 1.24 T, while the remanent magnetization is kept almost at same value as that of Nb-free sample.

Fig. 2(a) shows the temperature dependence of coercivities in Nb-free and 0.2 at.% Nb-doped samples. It is seen in Fig. 2(a) that the coefficient of coercivity (β) measured in the temperature range of 27-227 °C is determined to be –0.456 %/°C in Nb-free sample, which is marginally improved to –0.454 %/°C by 0.2 at.% Nb doping. Fig. 2(b) shows the plots of H_c/M_s versus H_a/M_s measured from 27°C to 107°C for the Nb-free and 0.2 at.% Nb-doped hot-deformed magnets to determine the α and N_{eff}. Generally, the coercivity can be phenomenologically described by $H_c(T) = \alpha H_A(T) - N_{eff} M_s(T)$, where H_A(T) and M_s(T) are the magnetocrystalline anisotropic field and saturation magnetization at various temperatures. Thus, α and N_{eff} can be deduced by plotting H_c/M_s against H_A/M_s at various temperatures followed by fitting the data linearly. Here, α values were deduced to be 0.36 and 0.46 for Nb-free and 0.2 Nb-doped hot-deformed magnets, respectively. While N_{eff} increases from 0.92 to 1.11 by doping 0.2 at.% Nb.

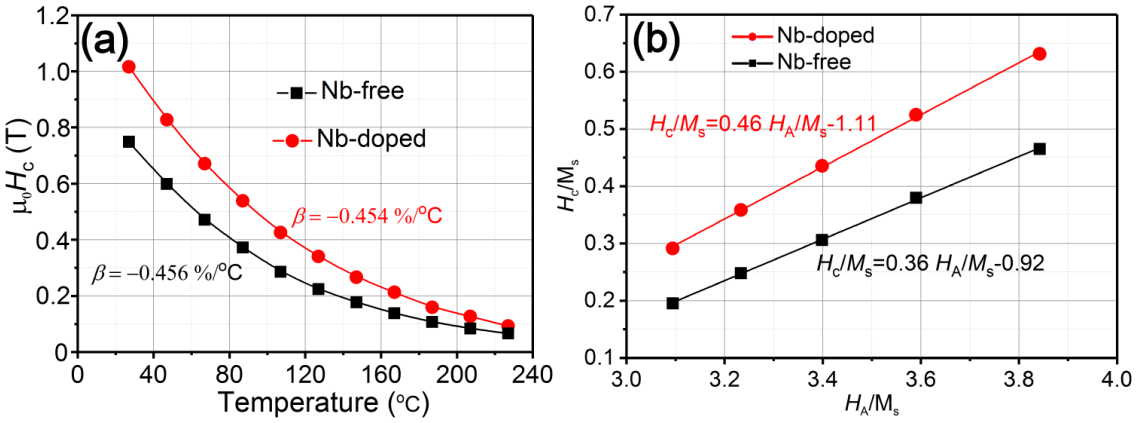

Fig. 2. (a) Temperature dependence of coercivity and (b) temperature dependence of H_c/M_s on H_a/M_s of the Nb-free and 0.2 at.% Nb-doped hot-deformed samples. The slope and intercept of linearly fitted plots are determined to be the parameters α and N_{eff}, respectively.

4.3.2 Microstructure in Nb-free and Nb-doped hot-deformed magnets

The overall microstructures of the Nb-free and Nb-doped hot-deformed magnets are shown in Fig. 3. Figs. 3(a-c) show low magnification back scattered electron (BSE) SEM images with *c*-axis in-plane for the Nb-free, 0.2 Nb-doped and 0.6 Nb-doped hot-deformed magnets, respectively. In these images, the 2:14:1 grains with grey contrast locate inside of ribbons while the grains with bright contrast are the neodymium oxide located on the surface of stacked ribbons [16,17]. Based on the different contrast, the areal fractions of NdO_x on the ribbon surface for Nb-free, 0.2 Nb-doped and 0.6 Nb-doped samples are calculated to be 0.96%, 0.65% and 0.78%, respectively. The high-magnification images taken from the inside of ribbons in Nb-free, 0.2 Nb-doped and 0.6 Nb-doped samples are presented in Fig. 3(d-f), respectively. In the inside of ribbons, the platelet-like grains are formed after hot-deformation and the $Nd_2Fe_{14}B$ grains with grey contrast are isolated by a thin grain boundary phases with a bright contrast. In the Nb-free sample, the average grain size of the samples was measured from BS-SEM images to be ~329 nm along the *c*-plane (D_c) and ~76 nm in the perpendicular direction (D_{ab}) to the *c*-plane. After doping 0.2 at.% Nb, the grain size substantially decreases to ~245 nm in width (D_c) and increases slightly to ~ 87 nm in height (D_{ab}). With increasing Nb doping to 0.6 at.%, D_c further increase to ~ 281 nm with substantial increase in D_{ab} to ~126 nm. Consequently, the aspect ratio (D_c/D_{ab}) of the grains decreases from 4.33 to 2.82 by adding 0.2 at.% Nb, which is further reduced 2.23 in 0.6 at.% Nb-doped sample, implying the grain shape in 0.6 Nb-doped sample is shown more feature of rounded shape, which can be evidenced in Fig. 3(f). The other feature is that the network of intergranular phase with bright contrast is clearer and more continuous, especially in the side plane grain boundaries of elongated grains with increasing Nb doping, suggesting that relatively more Nd is enriched in the side-plane grain boundaries. This may be because that the reduced aspect ratio can decrease the interfacial energy gap between *c*-planes and side-planes and Nd is no longer preferentially segregated in *c*-plane grain boundary phases. The high-magnification images taken from the interface of ribbons in Nb-free, 0.2 Nb-doped and 0.6 Nb-doped samples are presented in Fig. 3(g-i), respectively In the interface of ribbons, the large misaligned equiaxed grains can be observed in the Nb-free hot-deformed magnet as shown in Fig. 3(g). Those misaligned grains can be eliminated by doping 0.2 at.% Nb as shown in Fig. 2(h). With further increasing the Nb addition to 0.6 at.%, the surface

crystallites appears again. More details about the overall microstructure comparison in Nb-free and 0.2 at.% Nb-doped magnets are summarized in Table 2.

Table 2 Size and aspect ratio (AR) of grains, and areal fraction (AF) of NdO_x on the interface of ribbons in Nb-free and 0.2 at.% Nb-doped hot-deformed samples.

Samples	D_c	D_{ab}	AR	AF of NdO_x
Nb-free	329 nm	76 nm	4.33	0.96%
Nb-doped	245 nm	87 nm	2.82	0.65%

Fig. 4 shows the Lorentz TEM images of in Fresnel mode of Nb-free and 0.2 at.% Nb-doped hot-deformed magnets. It is shown in Fig. 4(a) that the Lorentz TEM image of the Nb-free hot-deformed samples at zero applied field in a thermally demagnetized state. The typical stripe-like domain patterns separated by the dark and bright contrasts of the domain walls are observed in Fig. 4(a). The different contrast results from the opposite magnetization direction. In the Nb-free sample, there are many misaligned grains observed in the sample, where the domain walls (marked by arrows) are normally interrupted by non-aligned grains on the surfaces of ribbons in the Nb-free sample as shown in Fig. 4(a). After 0.2 at.% Nb doping, the misaligned grains are significantly suppressed and continuous domain walls straightly pass through the interface of stacked ribbons in 0.2 at.% Nb-doped magnets as shown in Fig. 4(b). With further increasing Nb doping to 0.6 at.%, the misaligned grains appears again in Fig. 4(c), where the interrupted magnetic domain can be observed again. This explains why the highest remanent magnetization is achieved in the 0.2 Nb-doped hot-deformed magnets. This is consistent with the magnetic properties shown in Fig. 1.

Fig. 5 shows the STEM-HAADF and STEM-EDS analyses of Nb-free hot-deformed magnet. It is seen that the bright contrast in grain boundaries of the HAADF images indicates the heavier elements, i.e. Nd are enriched in grain boundaries, which can be further confirmed by EDS mapping of Nd, where Nd is strongly segregated with Fe depletion in grain boundaries and triple junctions. In the map of Nd and Fe, the networking is not so continuous in side-plane grain boundaries, meaning low Nd and high Fe concentration can be found in the side-plane grain boundaries. Co is found slightly segregated in triple junctions, while Ga is enriched in grain boundaries and triple junctions. It is reported that Ga enrichment in grain boundary can reduce the

melting temperature of grain boundary and increase wettability of Nd-Ga-rich intergranular phase as well as coercivity due to better exchange decoupling between 2:14:1 phases [18,19].

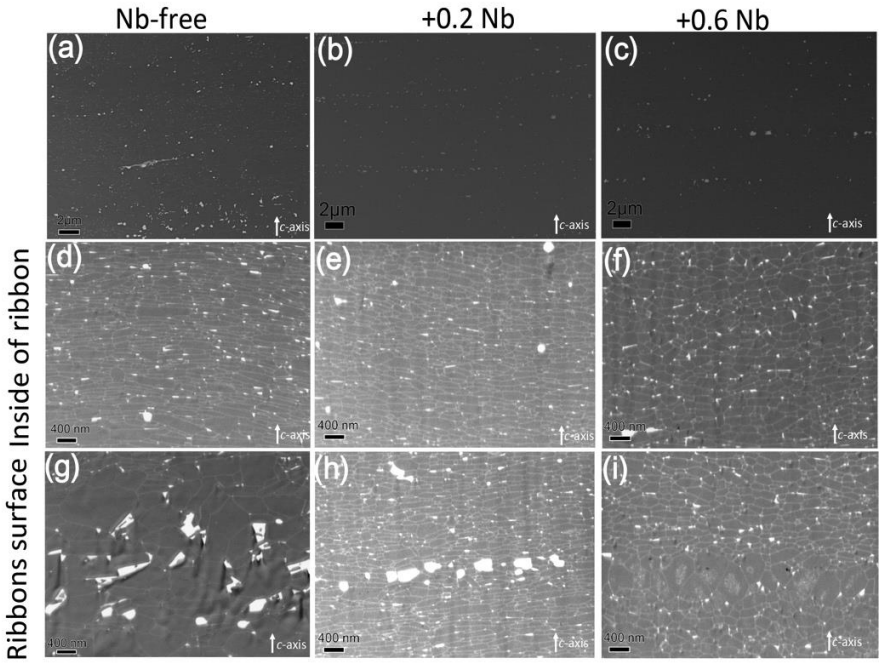

Fig. 3. Low magnification cross-sectional back scattered (BS) BS scanning electron microscopy (SEM) images of (a) Nb-free, (b) 0.2Nb-doped and (c) 0.6 Nb-doped hot-deformed magnets; high magnification cross-sectional BSE SEM images taken from inside of ribbons of (d) Nb-free, (e) 0.2 Nb-doped and (f) 0.6 Nb-doped hot-deformed magnets; high magnification cross-sectional BSE SEM images taken from interface of ribbons of (d) Nb-free, (e) 0.2 Nb-doped and (f) 0.6 Nb-doped hot-deformed magnets, *c*-axis is in-plane as the

Fig. 6 shows the STEM-HAADF and STEM-EDS analyses of Nb-doped hot-deformed magnet. It is seen in HAADF image of Fig. 6(a) that grain size is smaller as compared to that in Fig. 5. Nd and Ga is segregated in grain boundaries and triple junctions, where is depleted from Fe. Co is enriched in some cases of triple junctions. It is found in Nb map that the Nb-rich precipitates are located in the grain boundaries. With increasing Nb doping to 0.6 at.%, the grain size increases with reduction in aspect ratio of grains as shown in Fig. 6(b). In the meanwhile, the side-plane grain boundaries are more visible in the maps of Nd and Fe as compared to those in Fig. 6(a). The other noteworthy feature is that the number density of Nb-rich precipitates in Nb map is increased substantially with Nb doping increasing from 0.2 at.% to 0.6 at.%.

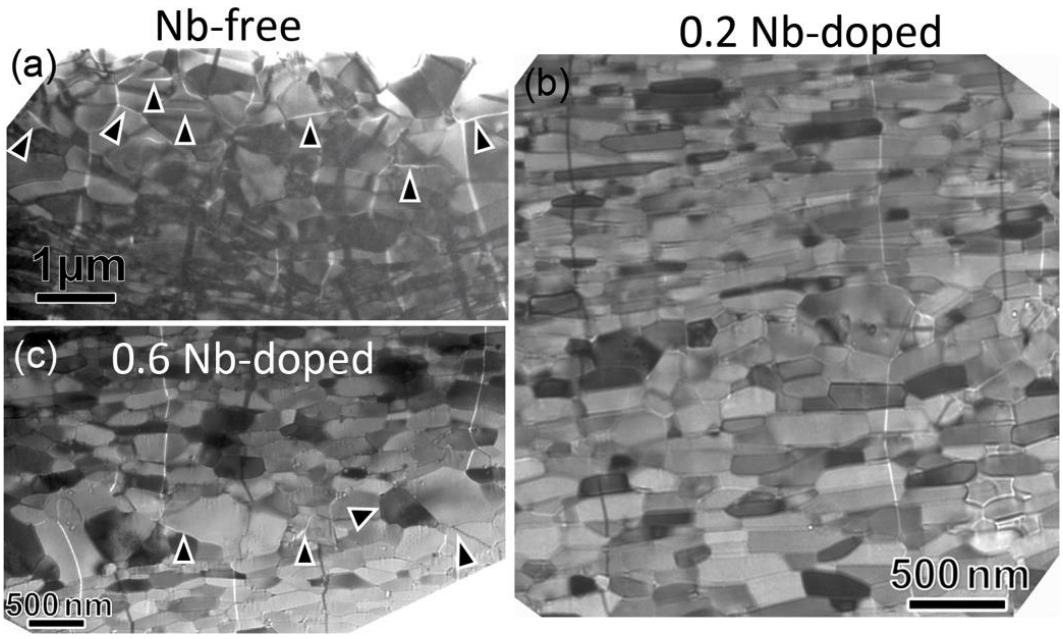

Fig. 4. Cross-sectional view Lorentz TEM images (a) of Nb-free, (b) 0.2 Nb-doped and 0.6 Nb-doped hot-deformed magnets at 0 applied magnetic field.

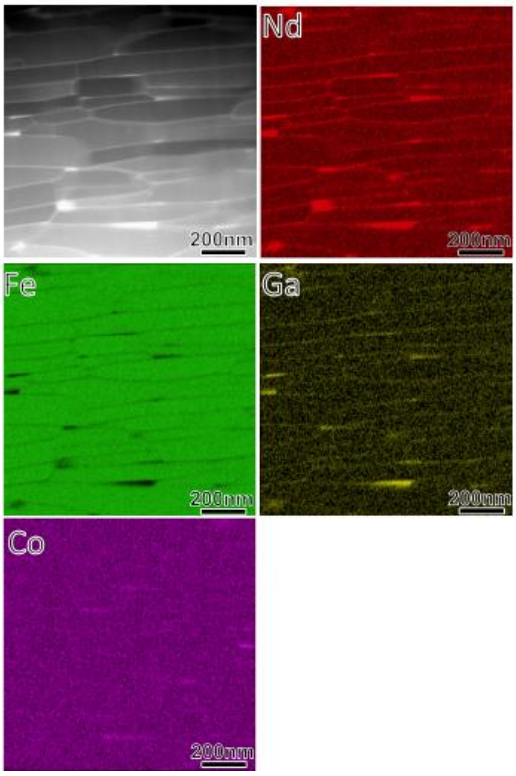

Figure 5. Low magnification HAADF image and EDS maps in Nb-free sample.

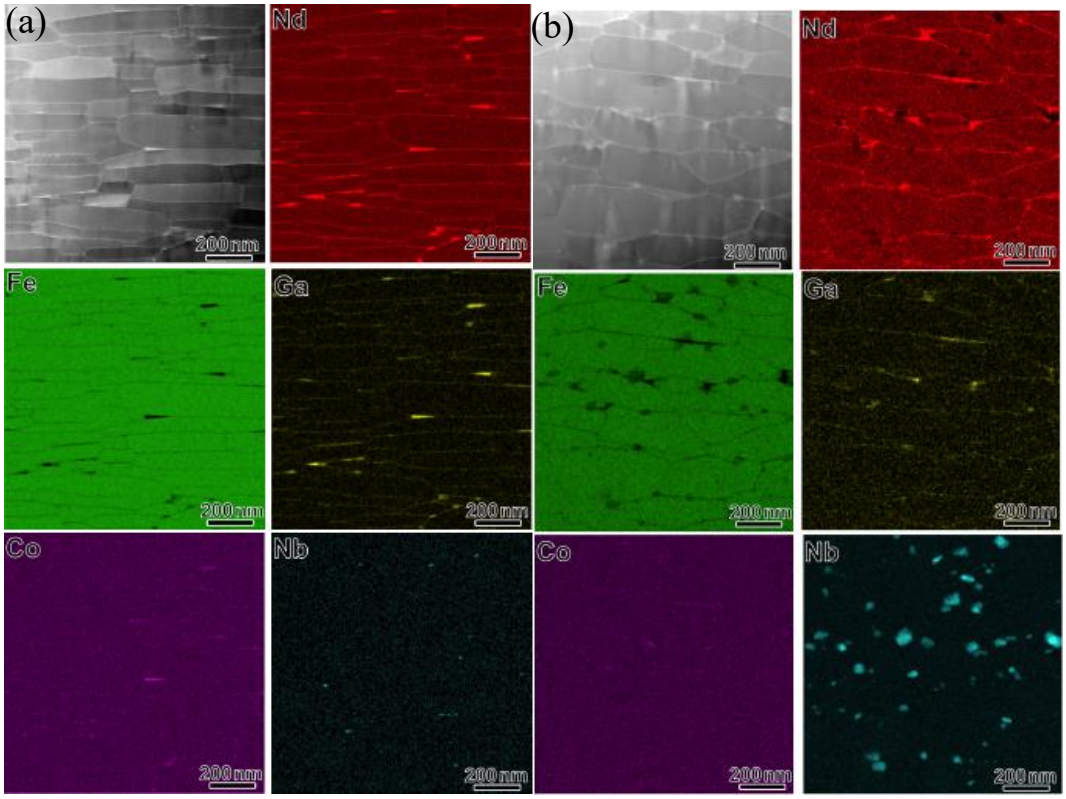

Figure 6. Low magnification HAADF image and EDS maps in 0.2 Nb-doped (a) and 0.6 Nb-doped (b) samples.

The compositions in grain boundaries phases are critically important for coercivity in hot-deformed magnets. Here, Fig. 7 shows three examples of high-resolution STEM-HAADF images taken from the *c*-plane grain boundaries between two $Nd_2Fe_{14}B$ phases in Nb-free and 0.2 Nb-doped hot-deformed magnets. The compositional profiles in Fig. 7(d-f) were obtained from superimposed EDS mappings in Figs. 7(a-c), respectively. From the inset superimposed Nd+Fe maps in Figs. 7(a-c), it shows that the Nd is enriched with depletion of Fe in those *c*-plane grain boundary phases. The periodical stacking of RE rich layers in the $Nd_2Fe_{14}B$ structure leads to the periodical compositional profiles of Nd and Fe+Co, implying the EDS analysis spatially reliable to analyze the composition in grain boundary phase within 1-2 nm. The concentrations of Nd in these three typical *c*-plane intergranular phases of Nb-free sample were calculated to be ~55.1 at.%, ~44.3 at.% and ~38.3 at.%. The concentrations of Fe+Co are accordingly measured to be, ~40.3 at.%, ~51.1 at.% and 56.7 at.% in these three grain boundaries. In contrast, In 0.2 Nb-doped hot-deformed sample, Nd concentration in these three *c*-plane grain boundary phase shown in Fig. 7(g-

i) are measured to be ~57.1 at.%, ~42.5 at.% and ~35.3 at.%, which is more or less comparable with those in *c*-plane grain boundary phases in Nb-free sample. Note that the Nb composition profile is not shown well because of too small addition of Nb. To be more accurate, at least five grain boundaries for each cases are observed to get average composition in grain boundary phase. The detailed information is summarized in table 3. One can see that the average Nd concentrations in the *c*-plane intergranular phases of Nb-free and 0.2 Nb-doped samples were determined to be ~41.1at.% and ~38.7 at.%, respectively, which are comparable with each other.

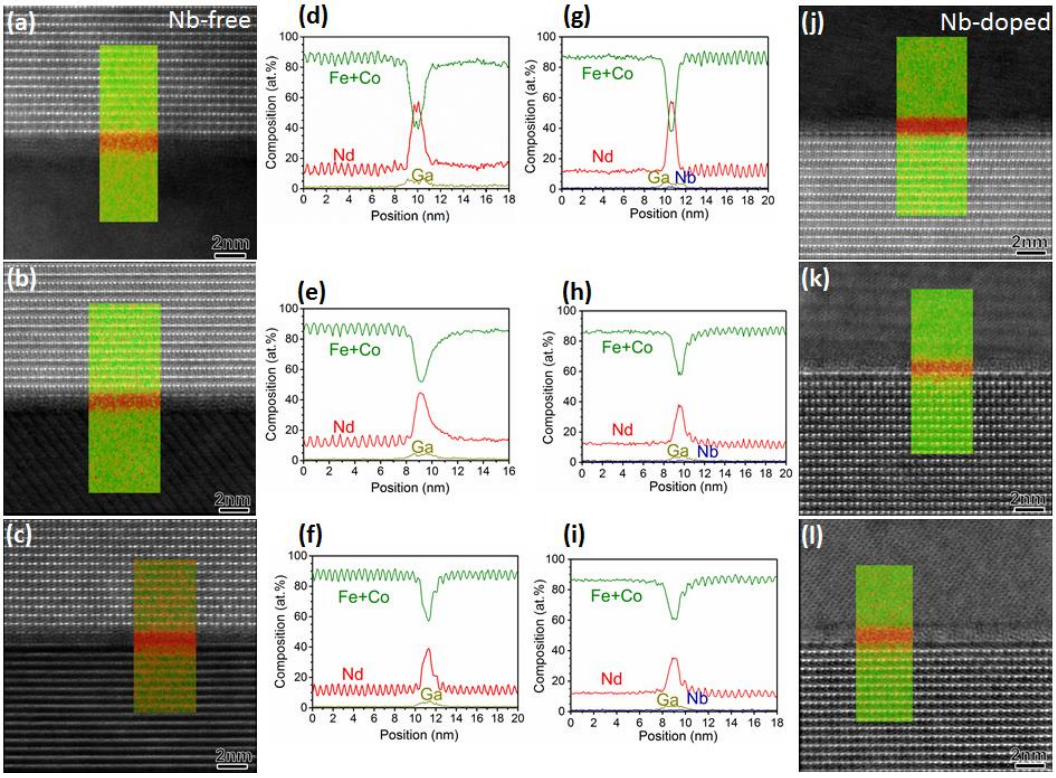

Figure 7. High-resolution (HR) HAADF-STEM images and inset EDS map of Nd+Fe obtained from *c*-plane intergranular phases in Nb-free (a-c) and 0.2 Nb-doped samples (j-l); (d-f) and (g-h) line scan profiles taken across interface of two grains in (a-c) and (j-l), respectively.

To obtain the comprehensive chemical composition in the grain boundary phases, the compositional information in side-plane intergranular phases are also investigated and shown in Fig. 8. Figs. 8(a-c) show weaker intensity from Nd in the Nd+Fe mapping as compared to those in *c*-plane intergranular phases (Figs. 7(a-c)), implying relatively less Nd concentration in side-plane

grain boundary phases. This is consistent with our previous work [17]. The EDS line compositional profiles shown in Fig. 8(d-f) were taken across typical side-plane Nd-rich grain boundary phases in Fig. 8(a-c) of Nb-free hot-deformed magnets. It is seen that the concentration of Nd and Fe+Co in these three side-plane intergranular phases of Nb-free hot-deformed magnets are close to ~28.3 at.%, ~21.5 at.%, ~18.1 at.% and ~66.9 at.%, ~74.1 at.%, ~76.9 at.%, respectively. In comparison, stronger intensity from Nd shown in Nd+Fe superimposed EDS map shown in Fig. 8(j-l), suggesting higher Nd concentration can found in the 0.2 Nb-doped samples, which can be confirmed in EDS compositional profiles shown in Fig. 8(g-i). The Nd concentration in side-plane grain boundary phases of 0.2 Nb-doped sample can be determined to be ~ 41.1 at.%, 35.1 at.% and 33. 5 at.%, which is higher than those in Nb-free sample. It is shown in table 3 that the average concentration of Nd can be increased considerably from ~ 25.4 at.% to ~ 35.1 at.% in the side-plane intergranular phases by doping 0.2 at.% Nb.

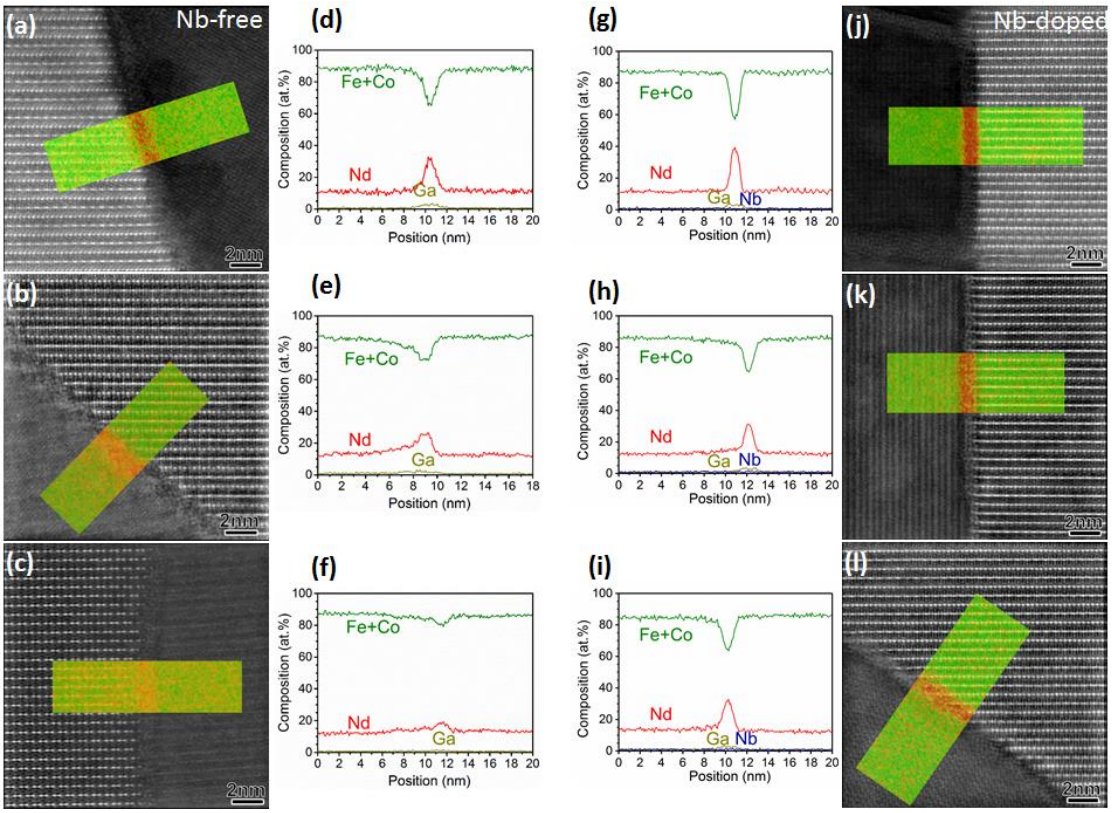

Figure 8. HR-HAADF-STEM images and inset EDS map of Nd+Fe obtained from side-plane intergranular phases in Nb-free (a-c) and 0.2 Nb-doped samples (j-l); (d-f) and (g-h) line scan profiles taken across interface of two grains in (a-c) and (j-l), respectively.

Table 3 Composition of Nd and Fe+Co in *c*-plane and side-plane grain boundary phase in Nb-free and Nb-doped hot deformed samples.

samples	*c*-Plane GB phases		side-Plane GB phases	
	Nd	Fe+Co	Nd	Fe+Co
Nb-free	41.1 at.%	51.9 at.%	25.4 at.%	67.6 at.%
Nb-doped	38.7 at.%	54.3 at.%	35.1 at.%	57.9 at.%

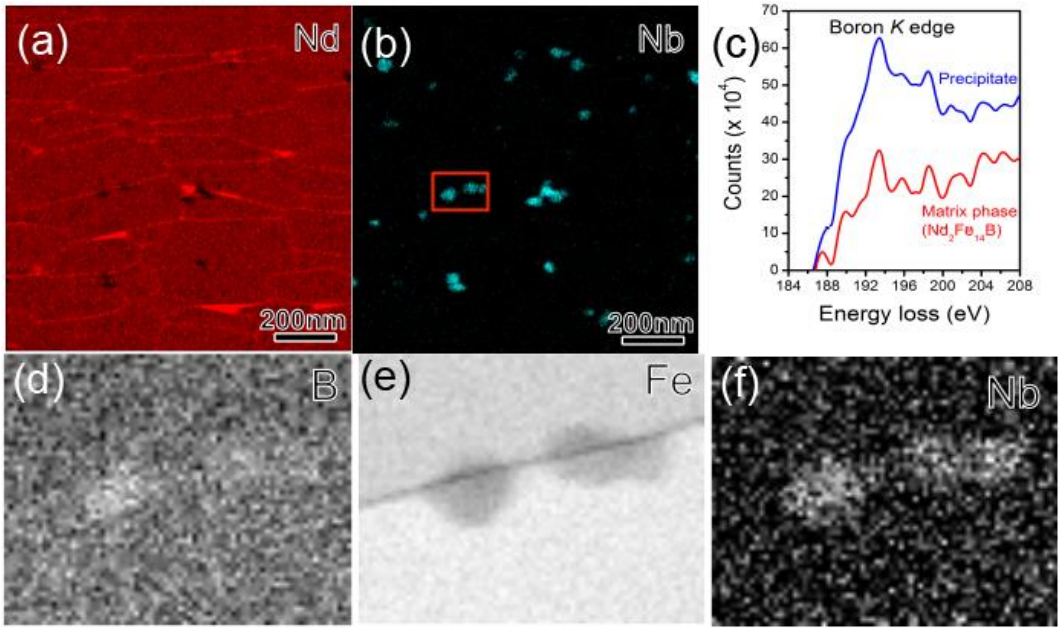

Figure 9. STEM-EDS of (a) Nd and (b) Nb, EELS study of (d) B, (e) Fe, (f) Nb and (c) energy loss spectrum obtained from Nb-rich precipitates and Nd-Fe-B matrix carried out in selected area of (b) in 0.6 Nb-doped hot-formed magnets.

4.3.3 Composition of Nb-rich phase and Nb content in grain boundary phases

As shown in Fig. 6, Nb-rich precipitates are depleted from Fe and Nd compared to Nd-Fe-B matrix. It is reported that Nb-rich precipitates are also enriched with light elements, such as carbon and boron in Nb-doped sintered magnets [11–13]. Compared to EDS analysis, EELS is more

powerful and accurate to analyze the light elements. Here, we carried out the EELS analysis in 0.6 at.% Nb-doped hot-deformed sample to check if any light elements enriched in Nb-rich precipitates. Fig. 9 shows the EELS analyses of Nb-rich phases. It is seen that the Nb-rich precipitates are enriched with Nb and depleted from Fe as compared to matrix. Fig. 9(d) shows the EELS map of B, one can see that the B is also enriched in Nb-rich precipitates, which is further confirmed by spectrum of EELS carried out in Nb-rich precipitates and Nd-Fe-B matrix as shown in Fig. 9(c). The intensity of B from the Nb-rich precipitates is higher than that from Nd-Fe-B matrix, indicating B concentration in Nb-rich precipitates should be higher than B concentration of $Nd_2Fe_{14}B$, ~6 at.%.

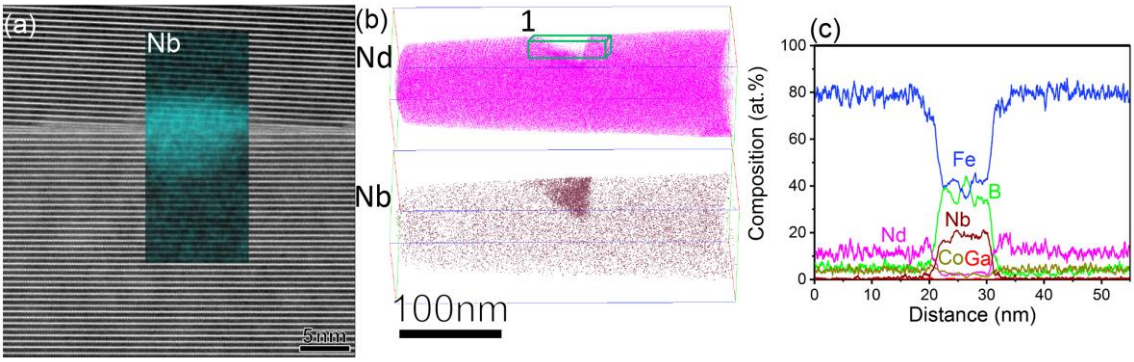

Fig. 10. High resolution HAADF image and superimposed EDS map of Nb in Nb doped sample (a), three dimension atom probe tomography of Nd and Nb obtained from Nb-rich phase in Nb-doped magnet.

To further obtain the accurate composition from Nb-rich precipitates, atom probe tomography is employed to analyze the composition of Nb-rich precipitates. Fig. 10 shows the atom probe tomography analysis results. In Fig. 10(a), a Nb-rich precipitate located in grain boundary observed in high-resolution TEM image, one can see that Nb-rich phase is too thin to get meaningful information of crystal structure. Bernardi *et al* [11,13] and Ahmed *et al* [12] reported that the Nb-rich precipitates in sintered magnets are supposed to be hexagonal ZrNiAl-type phase. Fig. 10 (b) shows the atom probe tomography Nd and Nb obtained from a Nb-rich precipitate near the grain boundaries. One can see that the Nb-rich precipitate is heavily depleted from Nd. Further compositional analysis of Nb-rich precipitate is shown in Fig. 10(c), indicating the composition of Nb-rich phase is ~$Nb_{24}Fe_{33}B_{43}$. This is consistent with our EELS analysis shown in Fig. 9.

Fig. 11 show atom probe results carried out from interface of two 2:14:1 phases. The probing direction is parallel to the *c*-axis of sample. Fig. 11(a) shows one *c*-plane grain boundary of Nb-doped sample. It is seen that grain boundary phase is enriched with Nd and slightly with Nb. Fig. 11(b) shows that three grain boundaries, which are all enriched with Nd and Nb. One of side-plane grain boundary is selected to further analyze the composition in grain boundary phase. Note that the Nb concentration is not well shown up in the EDS composition profiles as shown in Figs. 7-8. Here, from the atom probe map, we can clearly see that Nb is also segregated in *c*-plane and side-plane grain boundary phases.

To obtain the Nb composition, ladder diagrams for *c*-plane and *ab*-plane grain boundary phases obtained from selected box 1 and box 2 of Fig. 11 are shown in Fig. 12(a) and Fig. 12(b), respectively. The Nd concentrations in the *c*-plane and *ab*-plane grain boundary phases calculated from the Nd ladder diagrams in Figs.12 (c-d) were to be 38.1 at.% and 20.2 at.%, respectively. This is consistent with results in Figs. 12 (e-f). Nd concentration in *c*-plane grain boundary phase is higher than that in side-plane grain boundary phase. This is consistent with line scan compositional profiles in Figs. 7 and 8. The Nb concentrations in *c*-plane and *ab*-plane were determined to be ~0.25 and ~0.35 at.%, respectively. The segregation of Nb in the intergranular phases is considered to hinder the grain growth during the hot-deformation process, thereby reducing the grain size compared to the Nb-free sample.

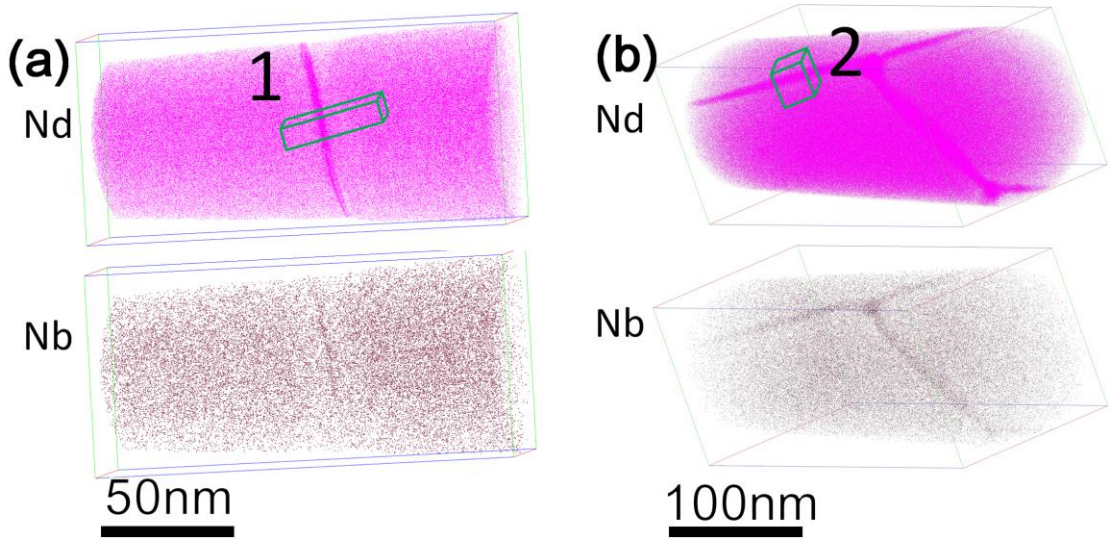

Fig. 11. 3D atom maps of Nd, Nb (a-b); *c*-axis of sample is parallel to probing direction.

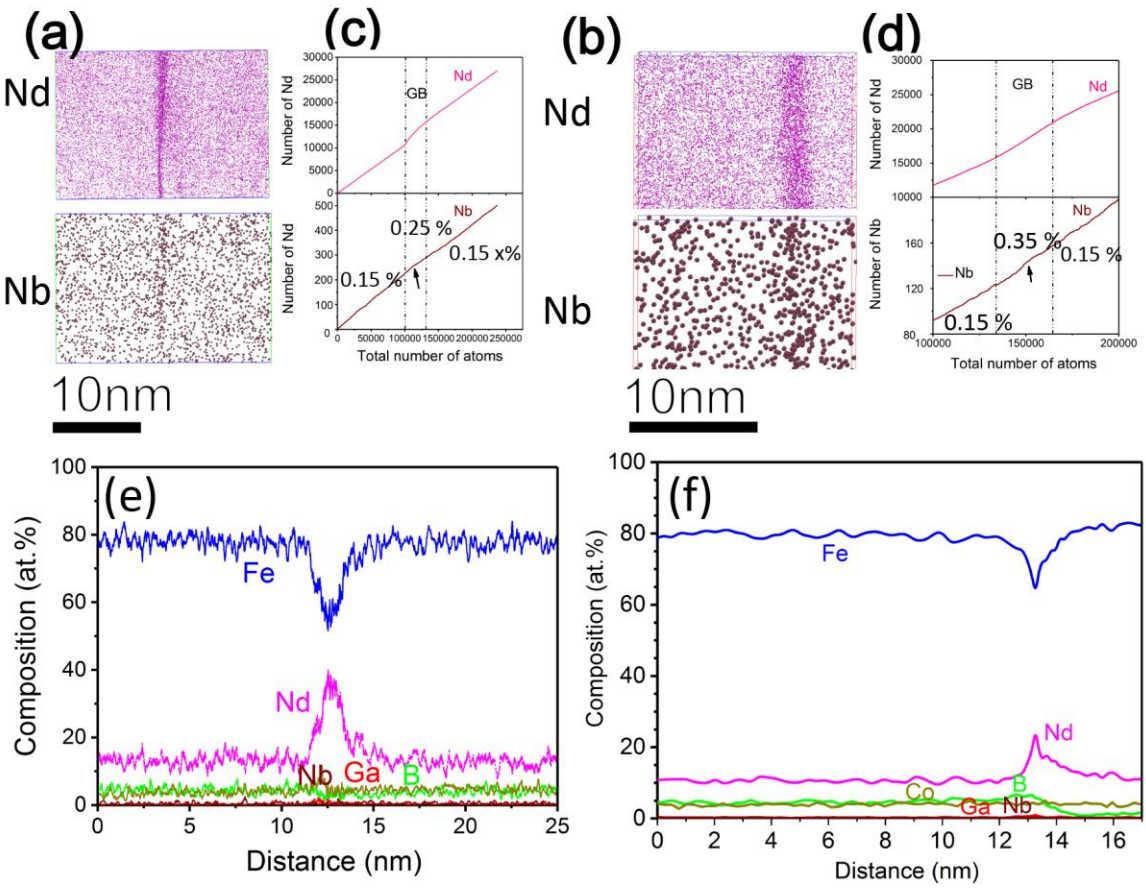

Figure 12. Atom probe of Nd and Nb obtained from selected (a) *c*-plane grain boundary phase (box1 in Fig. 11 (a)) and (b) *ab*-plane grain boundary phase (box2 in Fig. 11 (b)); ladder diagrams (c-d) and compositional profiles (e-f) obtained from box 1 and box 2, respectively.

4.3 Discussion

Since the good magnetic properties were achieved in 0.2 at.% Nb-doped hot-deformed magnets, the following discussion will be focused on Nb-free and 0.2 Nb-doped samples. In the Nb-free and 0.2 at.% Nb-doped hot-deformed samples, it is shown in Fig. 4 that the magnetic domain can pass straightly through the interface of stacked ribbons because of elimination of coarse non-aligned grains in the 0.2 at.% Nb-doped sample, meaning higher remanent magnetization can be achieved in 0.2 at.% Nb-doped sample as shown in Fig. 1. With increasing

Nb doping to 0.6 at.%, the surface crystallites appears again as shown in Fig. 3(i), resulting in reduction in remanent magnetization.

Concerning the coercivity in Nb-free and 0.2 at.% Nb-doped hot-deformed magnets, the coercivity, as extrinsic properties, is very sensitive to microstructure, which can be influenced by chemical composition of the intergranular phases. In general, higher Nd concentration in the intergranular phases strengthens pinning force against domain wall motion, leading to higher coercivity obtained in the magnet. Recent micromagnetic simulation studies have shown that the formation of nonferromagnetic grains in the side-plane boundaries are more effective in pinning the domain wall motion [5,20]. As shown in table 3, the average Nd concentrations in the *c*-plane intergranular phases of Nb-free and 0.2 at.% Nb-doped samples were determined to be ~41.1at.% and ~38.7 at.%, respectively, which are more or less comparable with each other. In contrast, the concentration of Nd can be enhanced considerably from ~ 25.4 at.% to ~ 35.1 at.% in the side-plane intergranular phases by doping 0.2 at.% Nb. The higher Nd concentration in the intergranular phases in the 0.2 at.% Nb-doped sample is not consistent with our previous report [17], in which larger grain size resulted in a higher Nd concentration in the intergranular phases. This can be explained based on our observation of the areal fraction of NdO_x that exists at the interface of original flakes. It was shown that addition of Nb optimizes the microstructure at the ribbon interfaces in the hot-deformed magnet, and the areal fraction of NdO_x was also reduced from 0.96% to 0.65% after 0.2 at.% Nb doping, which reduces the consumption of Nd on the interface of ribbons and result in higher Nd content in the grain boundaries. In addition, smaller aspect ratio in the 0.2 at.% Nb-doped hot-deformed magnet can be another reason for a higher Nd concentration in the side-plane grain boundaries of 0.2 at.% Nb-doped sample than that of Nb-free sample. This increases the pinning force against reversed magnetic domain and is beneficial to a higher coercivity in this sample.

In this work, α values were determined to be 0.36 and 0.46 for Nb-free and 0.2 Nb-doped hot-deformed magnets, respectively. Larger α is attributed to the increased Nd concentration in the side-plane intergranular phases in 0.2 at.% Nb-doped hot-deformed magnets as indicated in table 3. N_{eff} slightly increases from 0.99 to 1.11 by doping 0.2 at.% Nb. This result appears not to be consistent with the smaller aspect ratio of the grains in the Nb-doped hot-deformed magnets. The removal of equiaxed nonoriented grains at the interface of ribbons lead to the increase of the stray field in the 0.2 at.% Nb-doped sample. In addition, low Nd concentrations in intergranular phases

in both hot-deformed magnets as shown in table 3, implying the grains in the Nb-free and 0.2 at.% Nb-doped samples are strongly exchange coupled. Thus, the contribution of smaller aspect ratio to the reduced local demagnetizing constant N_{eff} was nullified.

4.4 Conclusion

In summary, the non-textured surface crystallites on the interface of ribbons in hot-deformed magnets have been successfully eliminated by trace addition of 0.2 at.% Nb, giving rise to the enhanced remanent magnetization in 0.2 at.% Nb-doped hot-deformed magnets. The coercivity was enhanced from 0.75 T to 1.04 T by 0.2 at.% Nb doping, which is attributed not only to the refined grains, but even more importantly to a considerable enhancement of Nd concentration from ~ 25.4 at.% to ~ 35.1 at.% in the side-plane intergranular phases. This is considered to contribute to the enforcement of domain wall pinning force. With further increasing Nb doping to 0.6 at.%, the aspect ratio of grains was further reduced to 2.33 with presence of coarse misaligned grains, leading to an increase in the coercivity and a reduction in remanent magnetization.

Reference

[1] K. Hono, H. Sepehri-Amin, Scr. Mater. 67 (2012) 530–535.

[2] J. Liu, H. Sepehri-Amin, T. Ohkubo, K. Hioki, A. Hattori, K. Hono, J. Appl. Phys. 115 (2014) 17A744.

[3] T. Mouri, M. Kumano, H.Y. Yasuda, T. Nagase, R. Kato, Y. Nakazawa, H. Shimizu, Scr. Mater. 78–79 (2014) 37–40.

[4] X. Zheng, M. Li, R. Chen, F. Lei, C. Jin, Z. Wang, J. Ju, W. Yin, D. Lee, A. Yan, Scr. Mater. 132 (2017) 49–52.

[5] H. Sepehri-Amin, T. Ohkubo, S. Nagashima, M. Yano, T. Shoji, A. Kato, T. Schrefl, K. Hono, Acta Mater. 61 (2013) 6622–6634.

[6] K. Loewe, D. Benke, C. Kübel, T. Lienig, K.P. Skokov, O. Gutfleisch, Acta Mater. 124 (2017) 421–429.

[7] L. Liu, H. Sepehri-Amin, T. Ohkubo, M. Yano, A. Kato, N. Sakuma, T. Shoji, K. Hono, Scr. Mater. 129 (2017) 44–47.

[8] L. Liu, H. Sepehri-Amin, T. Ohkubo, M. Yano, A. Kato, T. Shoji, K. Hono, J. Alloys Compd. 666 (2016) 432–439.

[9] U.M.R. Seelam, L. Liu, T. Akiya, H. Sepehri-Amin, T. Ohkubo, N. Sakuma, M. Yano, A. Kato, K. Hono, J. Magn. Magn. Mater. 412 (2016) 234–242.

[10] T. Akiya, J. Liu, H. Sepehri-Amin, T. Ohkubo, K. Hioki, A. Hattori, K. Hono, Scr. Mater. 81 (2014) 48–51.

[11] J. Bernardi, J. Fidler, M. Seeger, H. Kronmuller, IEEE Trans. Magn. 29 (1993) 2773–2775.

[12] F.M. Ahmed, D.S. Edgley, I.R. Harris, J. Alloys Compd. 209 (1994) 363–368.

[13] J. Bernardi, J. Fidler, J. Appl. Phys. 76 (1994) 6241–6243.

[14] D.. Ping, K. Hono, H. Kanekiyo, S. Hirosawa, Acta Mater. 47 (1999) 4641–4651.

[15] Y.Q. Wu, D.H. Ping, X.Y. Xiong, K. Hono, J. Appl. Phys. 91 (2002) 8174.

[16] J. Liu, H. Sepehri-Amin, T. Ohkubo, K. Hioki, A. Hattori, T. Schrefl, K. Hono, Acta Mater. 61 (2013) 5387–5399.

[17] X. Tang, H. Sepehri-Amin, T. Ohkubo, K. Hioki, A. Hattori, K. Hono, Acta Mater. 123 (2017) 1–10.

[18] H. Sepehri-Amin, W.F. Li, T. Ohkubo, T. Nishiuchi, S. Hirosawa, K. Hono, Acta Mater. 58 (2010) 1309–1316.

[19] I. Ahmad, H.A. Davies, R.A. Buckley, Mater. Lett. 20 (1994) 139–142.

[20] J. Fujisaki, A. Furuya, Y. Uehara, K. Shimizu, T. Ataka, T. Tanaka, H. Oshima, T. Ohkubo, S. Hirosawa, K. Hono, AIP Adv. 6 (2016) 056028.

Chapter 5: coercivity enhancemetn in Ce-Fe-B hot-deformed magnets by grain boundary infiltration of Nd-Cu

5.1 Introduction

Nd-Fe-B-based magnets are crucial materials for energy efficient technologies such as wind turbines and traction motors of (hybrid) electric vehicles [1,2]. In general, Nd-Fe-B-based magnets are comprised of ~30-33 wt.% of rare earth elements, for instance, Pr, Nd and Dy. To reduce the consumption of these critical elements, substituting Nd or Dy using low-cost rare earth elements, such as La or Ce, whose magnetic properties are in-between ferrite and sintered Nd-Fe-B magnets, has been proposed [3–6]. Yan *et al* reported that the presence of the $CeFe_2$ phase was ascribed to the abnormal jump in coercivity for x=0.24 [5]. Hard magnetic properties of the Ce-substituted sintered magnet with x=0.25 were further optimized to ~$\mu_0 H_c$=1.21 T and $\mu_0 M_r$=1.33 T by using a two alloy method [6].

Recently, hot-deformed magnets prepared by die-upsetting or hot-extruding melt-spun ribbons have drawn considerable attention because of their ultrafine-grained microstructures and their greater potential to achieve higher coercivity at elevated temperature as compared to sintered magnets [7]. Pathak *et al* and Pei *et al* [8–10] reported that there is an abnormal jump in coercivity to around ~ 1 T in melt-spun ribbon of $(Nd_{1-x}Ce_x)$-Fe-B for x= 0.25 accompanied by the formation of the $CeFe_2$ phase. A coercivity of ~1.7 T was reported for melt-spun Ce-substituted isotropic ribbons by further optimizing the composition; however, this value is deteriorated to ~0.94 T in hot-deformed anisotropic magnets. Further increase in x leads to a substantial reduction of coercivity [11], and only a very low coercivity of ~7 $\times 10^{-4}$ T was reported for hot-deformed Ce-Fe-B magnets. Given the relatively high anisotropy field of the $Ce_2Fe_{14}B$ phase (~3 T) [12], the coercivity value reported for the hot-deformed Ce-Fe-B magnet is too low. The eutectic grain boundary diffusion process has widely been applied to enhance the coercivity in HDDR, nanocomposite and hot-deformed magnets [13–20]. Recently, Ito *et al* reported that the coercivity of Ce-Fe-B hot-deformed magnets is enhanced by the infiltration of an eutectic Nd-Cu alloy [21]. In this work, we investigated the microstructure of Ce-Fe-B hot-deformed magnets and the ones

infiltrated with the Nd-Cu eutectic alloy in order to understand the origin of the coercivity enhancement by the Nd-Cu infiltration process.

5.2 Experimental procedure

The alloy ingots with the nominal composition of $Fe_{64.72}Ce_{29.8}Co_{4.0}Ga_{0.4}Cu_{0.1}Al_{0.08}B_{0.9}$ (wt.%) or $Fe_{75.61}Ce_{13.87}Co_{4.43}Ga_{0.37}Cu_{0.1}Al_{0.19}B_{5.43}$ (at.%) were prepared by induction melting high-purity constituent elements and followed by casting to a Fe book mold. The alloy was melt-spun at 20 m/s to obtain isotropic nanocrystalline ribbons. These melt-spun ribbons were crushed into small particles and then compacted by hot-pressing at 650°C under 400 MPa in vacuum, followed by die-upsetting at 750°C until their 70% height reduction were achieved. $Nd_{70}Cu_{30}$ alloy ribbons as a diffusion source were produced by the melt-spinning technique. The hot-deformed Ce-Fe-B magnets covered by the $Nd_{70}Cu_{30}$ ribbons were heat-treated at 700°C for 6 h. Ce-Fe-B magnets infiltrated with 10 wt.% and 40 wt.% $Nd_{70}Cu_{30}$ were fabricated by controlling the amount of Nd-Cu infiltration. The magnetic properties were measured using a superconducting quantum interface device vibrating sample magnetometer (SQUID-VSM). The microstructures were investigated by a scanning electron microscope (SEM) on Carl Zeiss CrossBeam1540EsB and scanning transmission electron microscope (STEM) on a Titan G^2 80–200 system with a probe aberration corrector. Three-dimension atom probe (3DAP) was performed on a locally built three-dimensional atom probe under ultrahigh vacuum in a flux range of 0.003–0.01 atom per pulse using a femtosecond Yb:KGd $(WO_4)_2$ laser with a third harmonic generator (λ = 343 nm) and a laser power of 0.1 μJ $pulse^{-1}$.

To simulate the demagnetization curves, the magnetic energy of the system was minimized in decreasing magnetic field at a field step of $\mu_0\Delta H_{ext}$ = -0.003 T. The saturation magnetization ($\mu_0 M_s$), magnetocrystalline anisotropy (K_u), and exchange stiffness (A) of the $Ce_2Fe_{14}B$ phase were chosen to be 1.21 T, 1.81 MJ/m^3, and 8 pJ/m, respectively [22]. $\mu_0 M_s$, A, and K_u values of $Nd_2Fe_{14}B$ were chosen to be 1.61 T, 4.9 MJ/m^3 and 8 pJ/m [23]. A limited memory quasi-Newton method was used for the energy minimization using "*b4vex*" simulation code.

5.3 Results

5.3.1 Magnetic properties and overall microstructure of as-deformed and diffusion processed samples

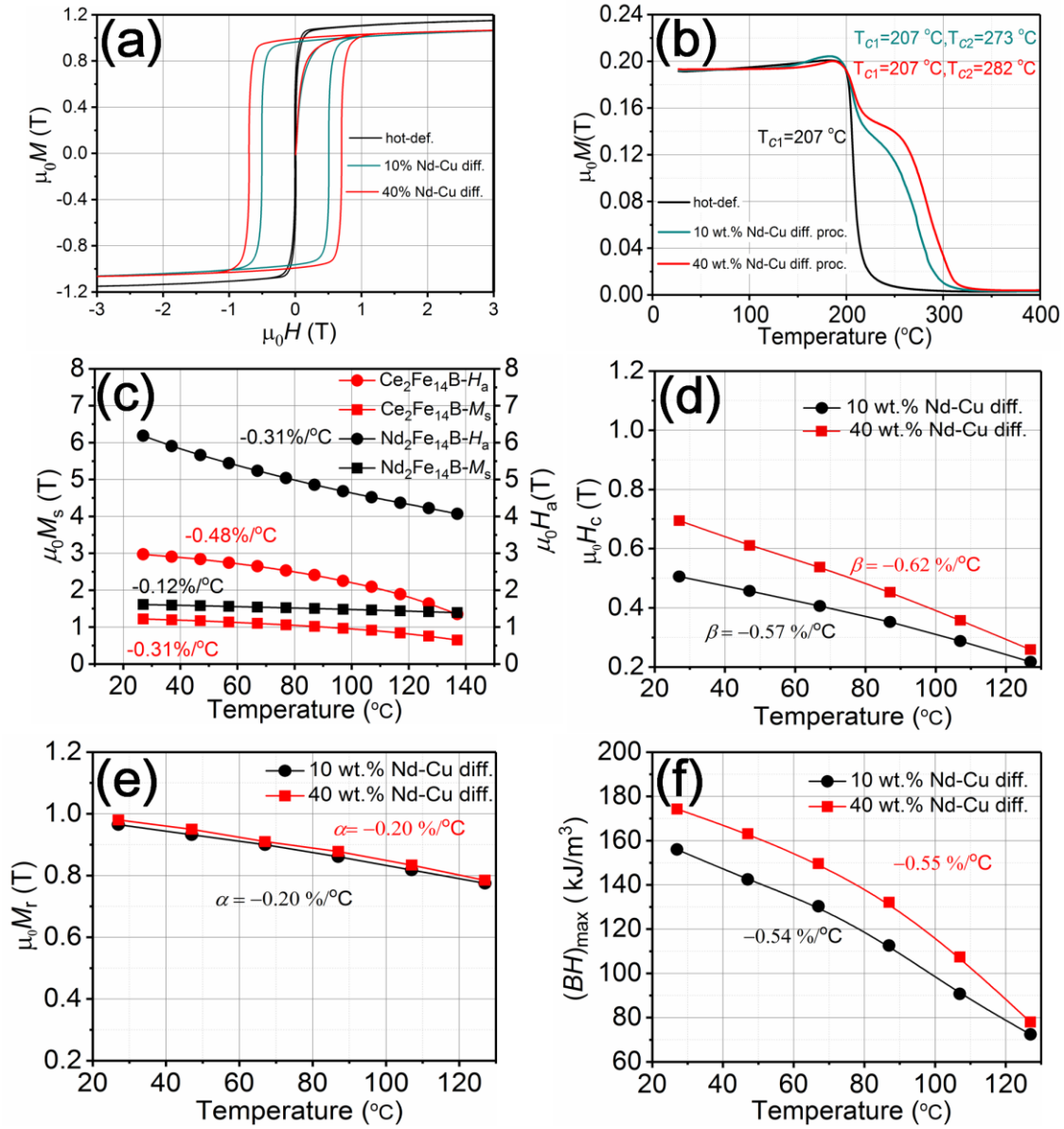

Fig. 1. Hysteresis loops (a) and M-T curves (b) for as-deformed and diffused samples, the temperature dependence of anisotropy field and saturation magnetization of $Nd_2Fe_{14}B$ and $Ce_2Fe_{14}B$ adopted from ref. [21,24] (c), and temperature dependence of coercivity (d), remanence (e) and $(BH)_{max}$ (f) in the diffused sample with 10 wt.% and 40 wt.% Nd-Cu.

Fig. 1(a) shows the hysteresis loops of Ce-Fe-B hot-deformed magnet and the ones infiltrated with Nd-Cu. After 10 wt.% Nd-Cu infiltration, the coercivity of the hot-deformed sample was dramatically increased from ~8 $\times 10^{-4}$ T to ~0.5 T; accordingly, remanent magnetization increased from ~0.61 T to ~0.96 T. With increasing diffusion of Nd-Cu to 40 wt.%, the coercivity and remanent magnetization increased to ~0.7 T and ~0.99 T, respectively. Fig. 1(b) shows *M-T* curves of the as-deformed and infiltrated samples. The Curie temperature of the hot-deformed Ce-Fe-B magnet was ~207 °C, which is higher than that of the value reported for the $Ce_2Fe_{14}B$ phase (~147 °C) [12]. This is resulted from Co doping in the $Ce_2Fe_{14}B$ phase [24]. In the infiltrated samples, two steps are observed on the *M-T* curves, indicating two Curie temperatures in the infiltrated samples, which correspond to the Curie temperatures of $Ce_2Fe_{14}B$ (~207 °C) and $(Nd_xCe_{1-x})_2Fe_{14}B$ (~273 °C) for the sample infiltrated with 10 wt.% Nd-Cu and $Ce_2Fe_{14}B$ (~207 °C) and $(Nd_xCe_{1-x})_2Fe_{14}B$ (~282 °C) for the sample infiltrated with 40 wt.% Nd-Cu, respectively. Note that with increasing infiltration of Nd-Cu, the Curie temperature for $(Nd_xCe_{1-x})_2Fe_{14}B$ shifts towards high temperature. Fig. 1(c) shows the temperature dependence of the anisotropy field ($\mu_0 H_A$) and the saturation magnetization ($\mu_0 M_s$) of $Nd_2Fe_{14}B$ and $Ce_2Fe_{14}B$ phases adopted from ref. [22,25]. The coefficient of temperature dependence of $\mu_0 H_A$ for $Nd_2Fe_{14}B$ and $Ce_2Fe_{14}B$, $(\Delta H_A/H_A\Delta T) \times 100\%$, in the temperature range of 27-137°C are –0.31%/°C and –0.48%/°C, respectively, indicating $Nd_2Fe_{14}B$ has better thermal stability of anisotropy field. In contrast, the coefficient of temperature dependence of $\mu_0 M_s$ for $Nd_2Fe_{14}B$ is –0.12%/°C, which is much larger than that for $Ce_2Fe_{14}B$, –0.31%/°C. Note that the thermal stability of saturation magnetization is superior to that of anisotropy field. Fig. 1(d) shows the temperature dependence of the coercivity of infiltrated samples. The coefficients of coercivity (β) for the samples infiltrated with 10 wt.% and 40 wt.% Nd-Cu were determined to be –0.57 %/°C and –0.62%/°C, respectively. Both of these are higher than those of the anisotropy field shown in Fig. 1 (c), suggesting microstructure gives influence on β. Note that the sample infiltrated with a smaller amount of Nd-Cu shows better thermal stability of coercivity. Figs. 1(e) and (f) show the temperature dependences of remanent magnetizations and maximum energy products of infiltrated samples, respectively. The coefficients of remanent magnetization, α, for the samples infiltrated with 10 wt.% and 40 wt.% Nd-Cu are the same, ~–0.20 %/°C, which is larger than β, resulting from better the thermal stability

of saturation magnetization as shown in Fig. 1(c). The coefficient of temperature dependence of $(BH)_{max}$ for the samples infiltrated with 10 wt.% and 40 wt.% were measured to be –0.54 %/°C and –0.55 %/°C, respectively.

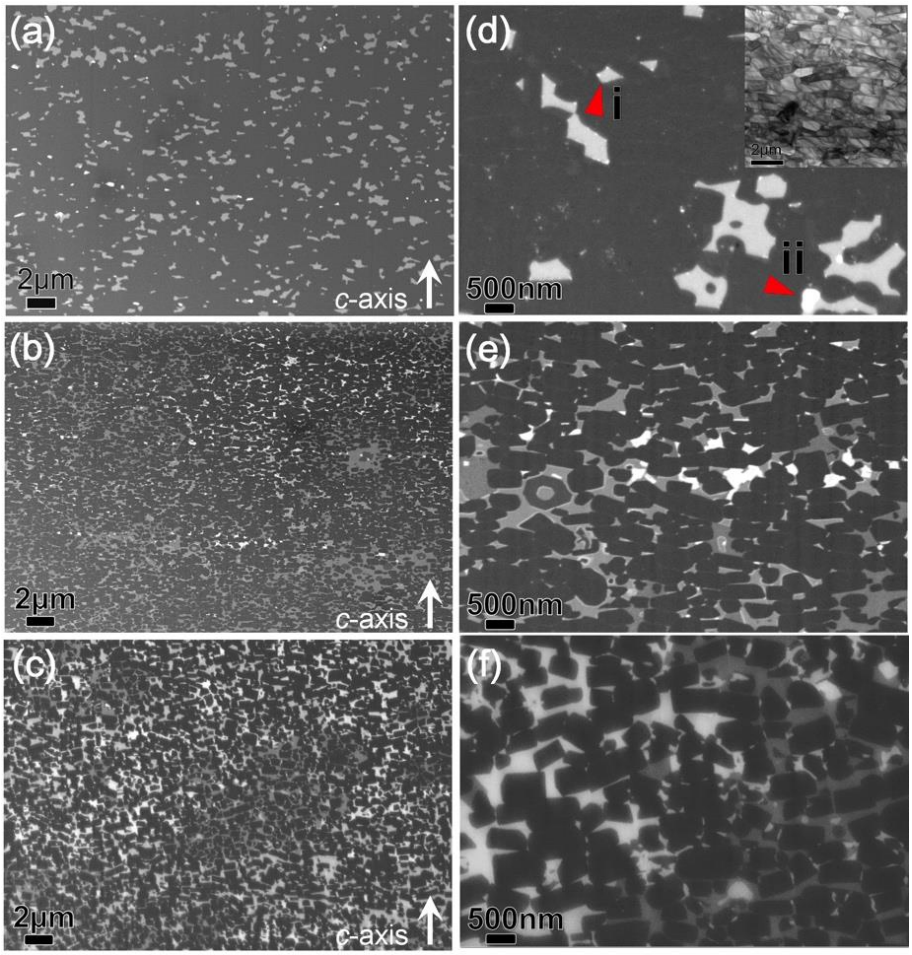

Fig. 2. Low and high magnification cross-sectional BSE SEM images of (a) and (d) as-deformed, (b) and (e) diffused sample with 10 wt.% Nd-Cu, (c) and (f) diffused sample with 40 wt.% Nd-Cu. The bright TEM of hot-deformed sample is shown in the inset of (d); *c* axis is in-plane as the arrow indicates.

Fig. 2 shows the overall microstructures of as-deformed Ce-Fe-B and the samples infiltrated with Nd-Cu. It is seen in Fig. 2(a) that the microstructure of the as-deformed Ce-Fe-B is mainly consisted of the $Ce_2Fe_{14}B$ with the dark contrast and two kinds of Ce-rich phases with the brightly grey contrast (indicated by red arrow area i and ii in Fig. 2 (d)). The overall areal fraction of the Ce-rich phases was calculated to be ~8.7%, which is significantly larger than areal fraction of Nd-

rich in as-deformed Nd-Fe-B magnet. The grain boundaries are not imaged with bright contrast even in the high magnification BSE image in Fig. 2(d), indicating that no Ce-rich grain boundary phase appears in grain boundaries. This is significantly different from the microstructure in hot-deformed Nd-Fe-B magnets, in which continuous networks of Nd-rich grain boundary phase is commonly observed in the as deformed state [26].

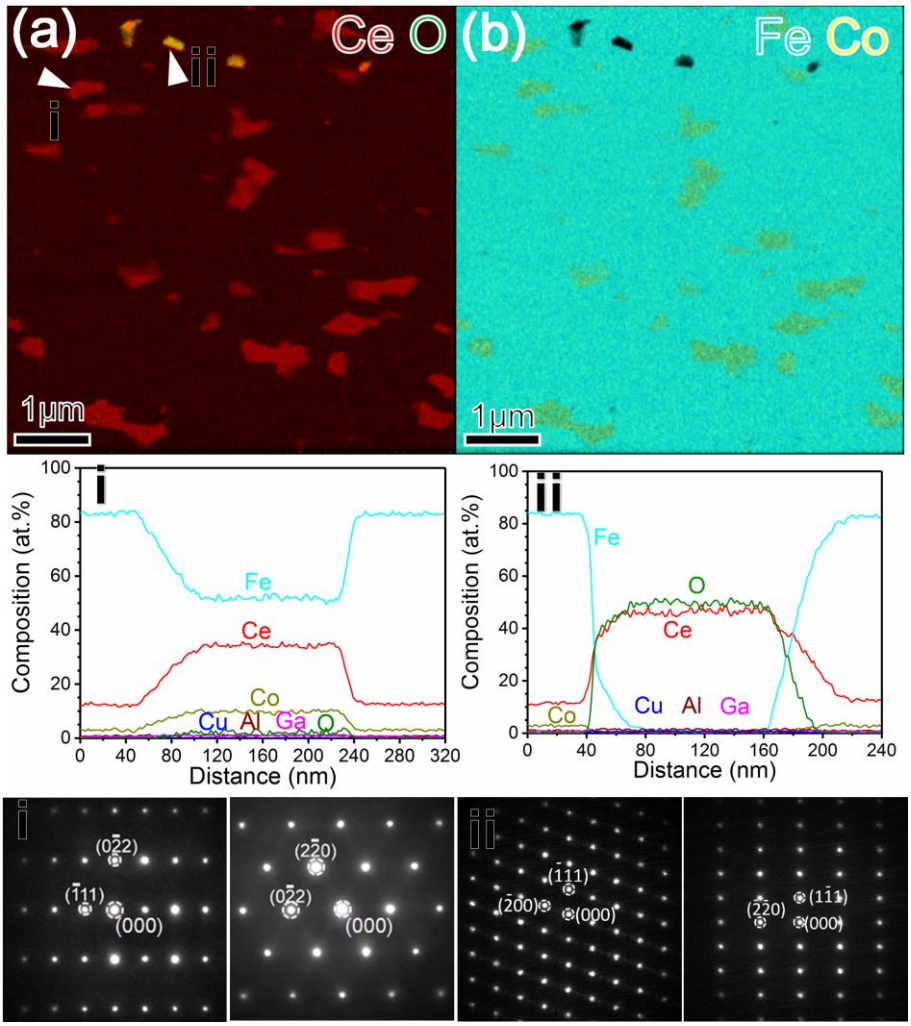

Fig. 3. STEM-EDS elemental mappings of as-deformed sample for (a) Ce+O, (b) Fe+Co. The compositional profiles and diffraction patterns taken from area i and area ii are marked as i and ii, respectively.

The inset in Fig. 2(d) shows the bright field TEM image of the as hot-deformed Ce-Fe-B magnets. $Ce_2Fe_{14}B$ grains are platelet-shaped, are similar to those in the hot-deformed Nd-Fe-B magnets. The average grain size of $Ce_2Fe_{14}B$ is ~834 nm along the *c*-plane and ~221 nm in the

perpendicular direction to the *c*-plane. Figure 2(b) shows a low magnification image of the Ce-Fe-B magnet infiltrated with 10 wt.% Nd-Cu. Three kinds of phases are observed with different contrasts; brightly-imaged regions enriched with high RE content, grey regions where relatively low RE are enriched and $Ce_2Fe_{14}B$ phase with dark contrast. The total areal fraction of the RE-rich phases was calculated to be ~19.1%, which increases to ~25.9 % after the infiltration of 40 wt.% Nd-Cu as shown in Fig. 2(c). In the meanwhile, the areal fraction of the most brightly imaged phase has increased. Figs. 2(e) and (f) show high magnification images of Ce-Fe-B magnets with 10 wt.% and 40 wt.% Nd-Cu infiltrations, respectively. Although some thick intergranular phases are observed in the infiltrated samples, the $Ce_2Fe_{14}B$ grains are not fully enveloped by the RE-rich intergranular phase. Note that the $Ce_2Fe_{14}B$ grains in Figs. 2(e-f) show more rounded shape compared to those observed in Nd-Fe-B hot-deformed magnets in ref. [14].

5.3.2 Elemental distributions and phases identification in as-deformed and diffused samples

Figure 3 shows STEM-EDS maps of Ce+O and Fe+Co obtained from the as-deformed Ce-Fe-B sample. In Fig. 3(a), no distinct contrast is observed along the grain boundaries, indicating the absence of Ce-rich intergranular phase. This is consistent with the BSE image in Fig. 2(a). Apart from the $Ce_2Fe_{14}B$ phase, we can also observe Ce-rich phases. An example of this Ce-rich phase is marked with arrow i; Co is preferentially partitioned while Fe is depleted from this phase compared to the matrix phase. The composition of the phase was estimated from compositional profiles to be around $Ce_{33}Fe_{56}Co_{10}$ (at.%). Nanobeam electron diffraction (NBED) patterns indicate that this phase is $Ce(Fe,Co)_2$ with the $MgCu_2$-type structure ($Fd\bar{3}m$). In addition to the Ce and Co rich secondary phase, CeO_x phase was also observed as marked with arrow ii in the STEM-EDS map of Ce+O. Chemical composition and NEBD patterns reveal that the minor type ii phase is $Ce_{50}O_{50}$ with the *fcc* structure.

Figure 4 shows of STEM-EDS maps in the sample infiltrated with 10 wt.% and 40 wt.% of Nd-Cu. In Fig. 4(a), it is seen that most of the thick intergranular phases are enriched with RE, Cu and in some cases Co. The Nd-rich shells are clearly observed in the $Ce_2Fe_{14}B$ grains with green contrast in the Ce+Nd+Cu map. The areal fraction of the Nd-rich shell surrounding the $Ce_2Fe_{14}B$ grains was determined to be ~4.6% for the sample infiltrated with 10 wt. % Nd-Cu. This value was increased to 13.7% after the 40wt.% Nd-Cu infiltration as shown in the Ce+Nd+Cu map of Fig. 4(b). It is noteworthy that the grains in the infiltrated samples show more rounded shape compared

to those in the hot-deformed Ce-Fe-B magnets. Grain sizes of $(Nd,Ce)_2Fe_{14}B$ were calculated to be ~540 nm and ~500 nm along the *c*-plane and ~272 nm and ~290 in the perpendicular direction to the *c*-plane for the sample with 10 wt.% and 40 wt.% Nd-Cu infiltration, respectively. More detailed comparisons between as-deformed and infiltrated samples are summarized in table 1. The aspect ratio of the grains, defined as the ratio between the size along the *c*-plane and in the perpendicular direction to the *c*-plane, is reduced from 3.75 in the as-deformed magnet to 1.72 in the sample infiltrated with 40 wt.% Nd-Cu. In the Ce+Nd+Cu map of the samples infiltrated with 10 wt.% and 40 wt.% Nd-Cu, one can know that these two sample share three types of intergranular phases; type I is Ce-rich intergranular phase enriched with Co and slight enrichment of Fe (marked with arrow I), type II is Nd-Cu-rich intergranular phase (marked with arrow II) and Nd-rich intergranular phase with slight enrichment of Cu (marked with arrow III).

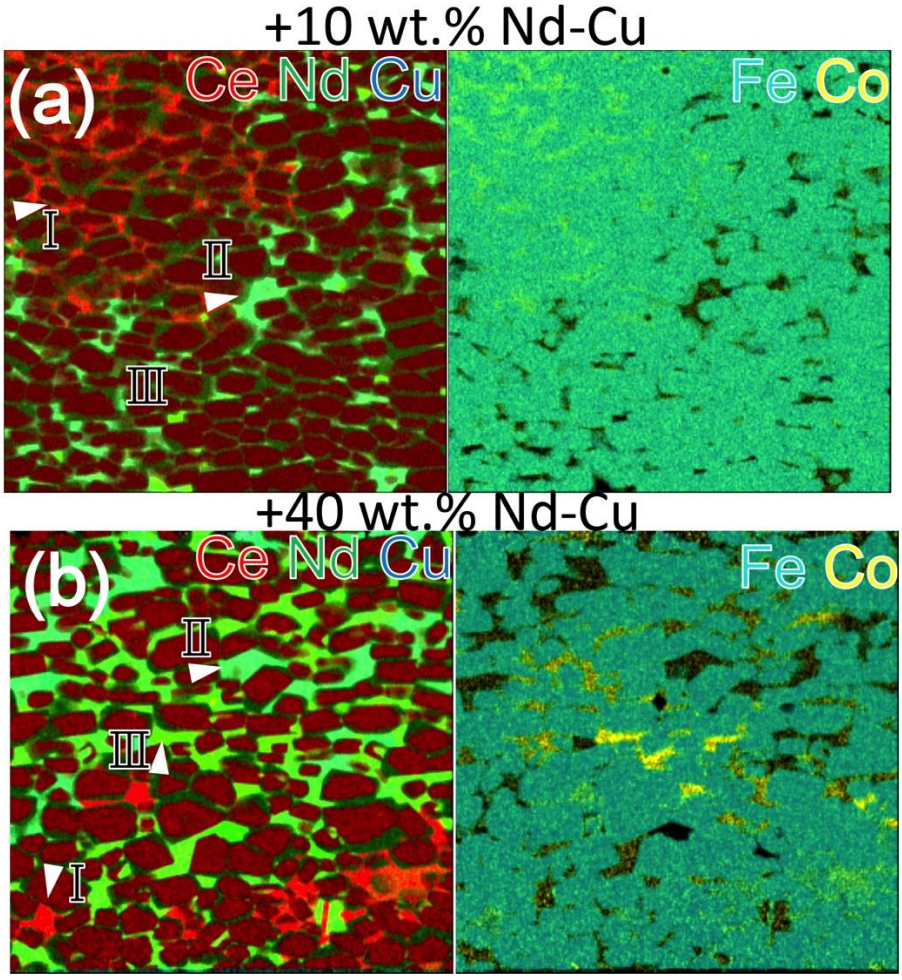

Fig. 4. Low magnification EDS maps of (a) diffused sample with 10 wt.% Nd-Cu and (b) diffused sample with 40 wt.% Nd-Cu for Ce+Nd+Cu, and Fe+Co.

Table 1 Grain size, aspect ratio (AR) of grains, areal fraction of secondary phases (AFSP) and areal fraction (AF) of Nd-rich shell in 2:14:1 grains in hot-deformed and as-diffused samples.

samples	D_c	D_{ab}	AR	AFSP	AF of Nd-rich shell
As-deformed	832 nm	222 nm	3.75	8.7%	0
+10 wt.% Nd-Cu	540 nm	272 nm	1.98	19.1%	4.6%
+40 wt.% Nd-Cu	501 nm	291 nm	1.72	25.9%	13.7%

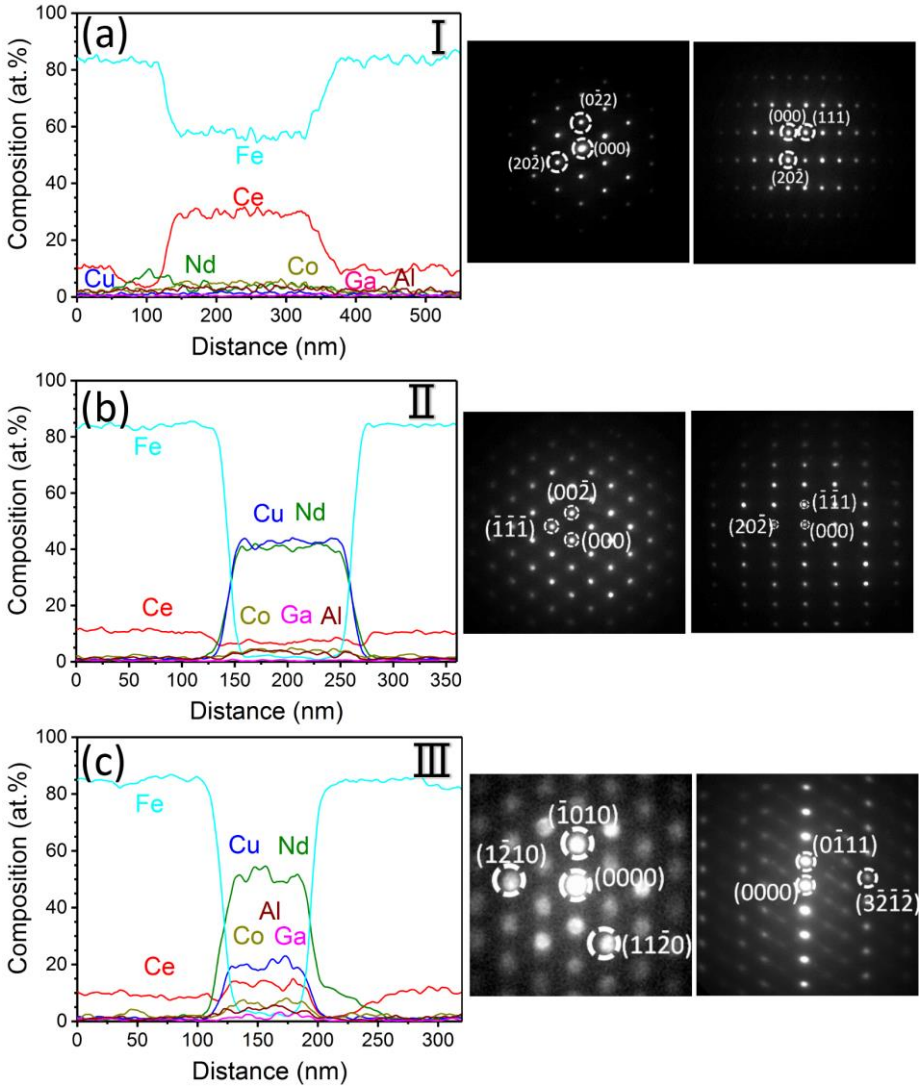

Fig. 5. The compositional profiles and diffraction patterns taken from area I (a), area II (b) and area Ⅲ(c) of Figs. 4(a-b).

Fig. 5 shows the compositions and diffraction patterns taken from region I, II, and Ⅲ. The Ce-rich type I phase has a chemical composition close to ~ $Nd_5Ce_{28}Fe_{61}Co_5$ with the $MgCu_2$-type ($Fd\bar{3}m$) structure, which is consistent with $CeFe_2$ phase. The composition and the diffraction patterns of the Nd-Cu-rich phase indicate that type II phase is $Nd_{40}Ce_{20}Cu_{40}$ with the *fcc* structure. The composition of the type Ⅲ Nd-rich phase was determined to be ~$Nd_{50}Ce_{20}Cu_{20}M_{10}$ (M=Al, Ga, Co) and the crystal structure was identified as the *dhcp* structure with a=0.365 nm and c=1.18 nm by the diffraction patterns. Based on the difference in Nd+Ce concentration among these three phases, the Nd-Cu-rich phase (type II) and Nd-rich (type III) correspond to the phase with bright contrast in Fig. 2(b), while the phase with grey contrast in BS SEM should be the $(Nd,Ce)(Fe,Co)_2$ phase (type I).

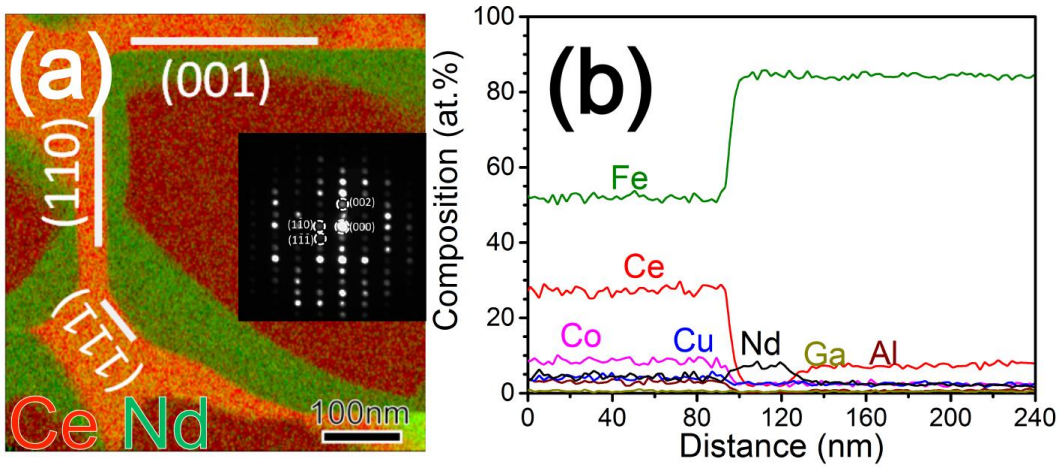

Fig. 6. Higher magnification of STEM-EDS elemental mappings of Ce+Nd and inset diffraction pattern taken from 2:14:1 phase (a) in diffused sample with 10 wt.% Nd-Cu, compositional profiles (b) taken near the shell part of 2:14:1 phase, respectively

Fig. 6 shows the higher magnification of STEM-EDS maps and EDS line profiles taken from intergranular phase to the 2:14:1 matrix in the diffused sample with 10 wt.% of Nd-Cu. A 2:14:1 grain neighboring to Ce-rich phase can be observed in Fig. 6(a). Based on the inset NBED pattern taken from 2:14:1 phase, planes of 2:14:1 grain faceted with intergranular Ce-rich phase can be determined to be ~(001), (110) and (111) planes. These facets are believed to reduce total surface energy [14]. It can be clearly seen that Ce is depleted from faceted side of the 2:14:1 grain, where is enriched by Nd. This suggests that $(Nd_xCe_{1-x})_2Fe_{14}B$ phase has formed in the shell of 2:14:1

phase. The EDS compositional profiles shown in Fig. 6(a) are taken from near 2:14:1 phase of in Fig. 6(a). Compositional profile indicated the chemical composition of this Ce-rich phase is close to $Nd_5Ce_{28}Fe_{56}Co_{10}$, should be $CeFe_2$ phase. One can also see that the Nd concentration profile increases at the shell region of 2:14:1 phase and then decreases at the core region, which further confirms the formation of core-shell structure.

5.3.3 Determination of *x* in Nd-rich $(Nd_xCe_{1-x})_2Fe_{14}B$ shell

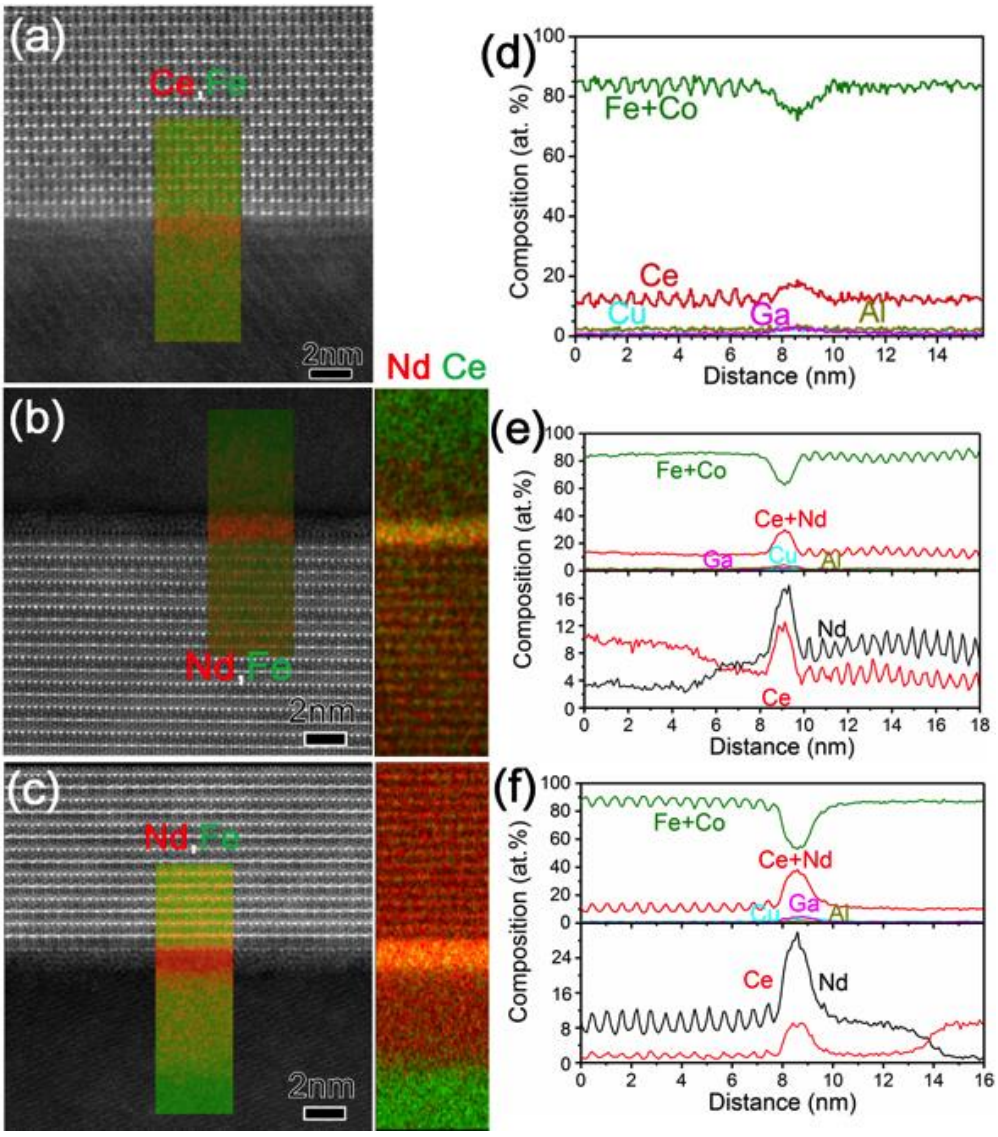

Fig. 7. High-resolution (HR) STEM images and inset EDS maps of Nd+Fe obtained from *c*-plane grain boundary phases of as-deformed (a) and the samples infiltrated with (b) 10 wt. % Nd-Cu and (c) 40 wt.%; (d-f) line scan profiles taken across interface in (a-c), respectively.

Fig. 7 presents high-resolution STEM-HAADF images obtained from the grain boundary phase along the *c*-plane interface between two 2:14:1 grains in the as-deformed and infiltrated samples. The line scan EDS profiles taken across *c*-plane grain boundaries of Fig. 7(a-c) are shown Fig. 7(d-f). In Fig. 7(a), a grain boundary phase with a thickness of ~1 nm is observed in HR-STEM-HAADF image and superimposed STEM-EDS map show a weak intensity from Ce in the grain boundary phase, indicating low Ce concentration segregated in grain boundary. This is further confirmed by the compositional profile obtained across this grain boundary phase, in which the Ce concentration is only 20 at.% and the concentration of Fe+Co is as high as 75 at.%. This indicates that the grain boundary phase in the hot-deformed Ce-Fe-B is ferromagnetic. Fig. 7(b) shows one of the typical thin grain boundary phase in the sample infiltrated with 10 wt.% Nd-Cu; the contrast from the STEM-EDS map of Nd+Ce shows the formation of a Nd-rich shell with the presence of Nd and Ce enriched grain boundary phase. Detailed compositional analysis in Fig. 7(e) shows 17.6 at.% Nd and 12.5 at.% Ce are enriched in this grain boundary phase, and the total rare earth content is 30.1 at.%, which is considerably higher than that in the as-deformed sample. The Nd concentration in the $(Nd_xCe_{1-x})_2Fe_{14}B$ shells surrounding the 2:14:1 grains is another factor to influence the coercivity. Herein, we determine *x* by averaging the Nd and Ce line scans in the EDS profiles. The wave-like EDS profiles of Nd and Ce result from the periodical stacking of RE-rich layers in the 2:14:1 structure. By averaging these periodical compositional profiles, *x* was determined to be ~0.67. This value increases to ~0.85 after the infiltration of 40 wt.% Nd-Cu as shown in Fig. 7(f). Moreover, the total rare earth content in the thin grain boundary phase of the sample infiltrated with 40 wt.% Nd-Cu is 38.1 at.%, which is consisted of 29.6 at.% Nd and 8.5.% Ce. This is noticeably lower than that in the hot-deformed Nd-Fe-B magnets infiltrated with Nd-Cu eutectic alloy [14]. Generally, after the Nd-Cu infiltration to as-deformed Nd-Fe-B magnets, the concentration of Nd can be as high as ~90 at.%.

Fig. 8 shows high-resolution STEM-HAADF images obtained from side-plane grain boundaries of 2:14:1 grains in the as-deformed and infiltrated samples and EDS line compositional profiles shown in Figs. 8(d-f) obtained from superimposed EDS maps of Figs. (a-c), respectively. The EDS compositional profiles in Fig. 8(d) shows that the side grain boundary phase in the as-deformed sample contains only 18 at.% of Ce, which is comparable to that in the *c*-plane grain boundary phase. After 10 wt.% Nd-Cu infiltration, the EDS profiles in Fig. 8(e) shows that the

concentration of rare earth elements increased to 28.2 at.% consisting of 13.1 at.% Nd and 15.1% Ce. Note that the concentration of the rare earth elements in the side-plane is more or less comparable to that in the *c*-plane grain boundary phase. With the further infiltration of 40 wt.% Nd-Cu, 20.4 at.% Nd + 5.8 at.% Ce were found in the side grain boundary as shown in Fig. 8(f). *x* of $(Nd_xCe_{1-x})_2Fe_{14}B$ shell increases from 0.55 in 10 wt.% Nd-Cu infiltrated sample to 0.84 in the 40 wt.% Nd-Cu infiltrated sample, which is comparable to that of *c*-plane shell region.

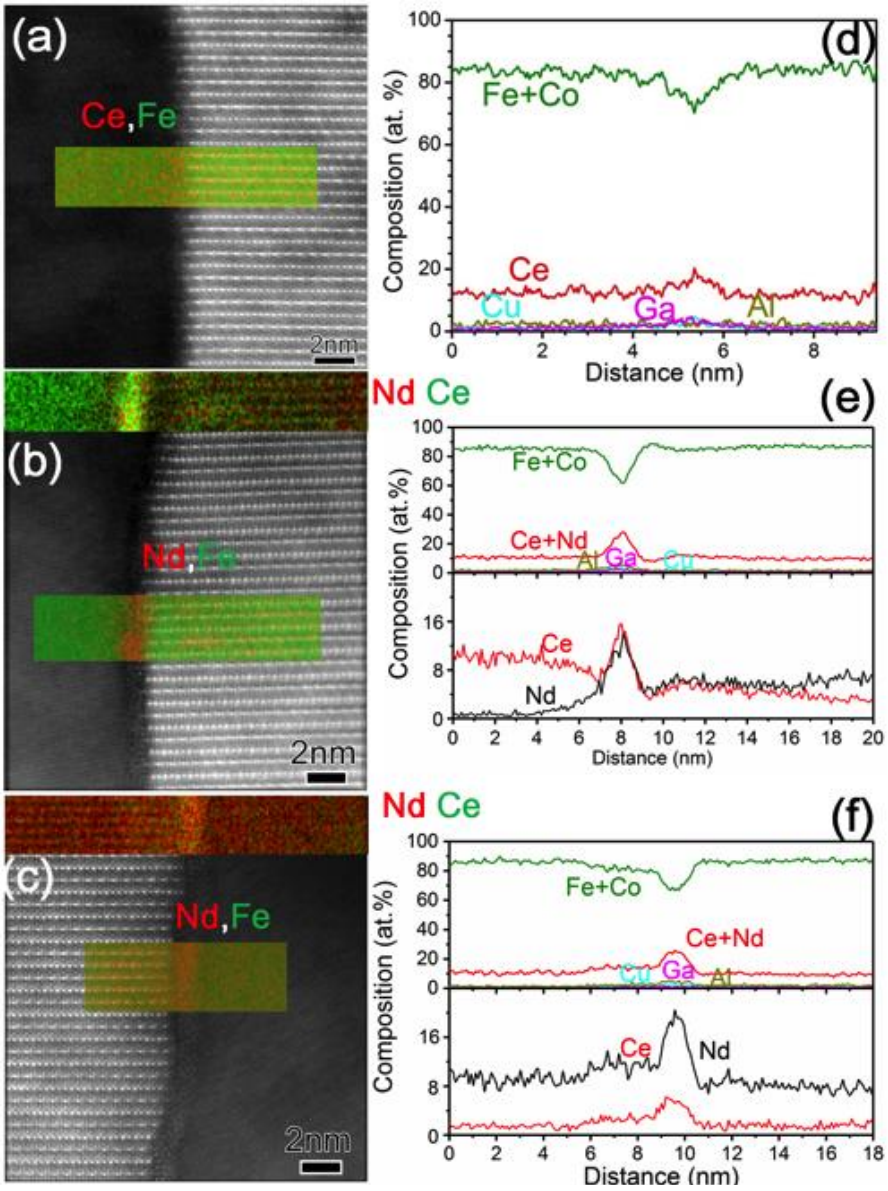

Fig. 7. HR-STEM images and inset EDS maps of Nd+Fe obtained from side-plane grain boundary phases of as-deformed (a) and the samples infiltrated with (b) 10 wt. % Nd-Cu and (c) 40 wt.%; (d-f) line scan profiles taken across interface in (a-c), respectively.

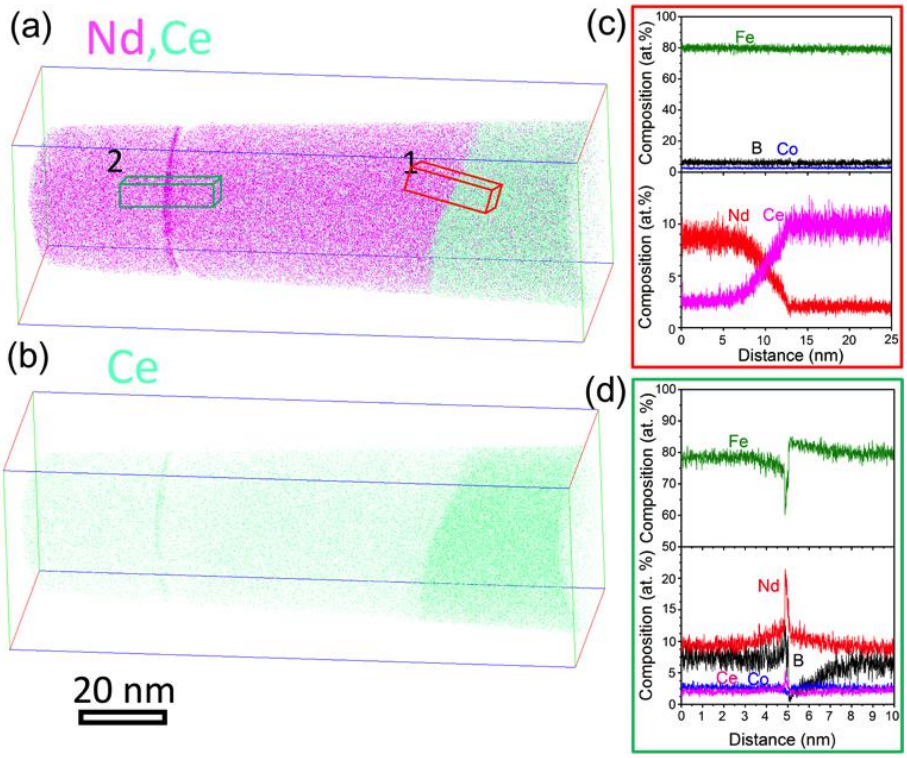

Fig. 9. Three dimension atom probe tomography of (a) Nd+Ce and (b) Ce obtained from diffused sample with 40 wt.% Nd-Cu; Compositional profiles of (c) and (d) calculated from box 1 and box 2, respectively.

To further quantify x in the $(Nd_xCe_{1-x})_2Fe_{14}B$ shell, Fig. 9 shows the atom probe tomography of Nd+Ce and Ce obtained from the sample infiltrated with 40 wt.% Nd-Cu. The *c*-axis is parallel to the probing direction. The compositional profiles were obtained from an interface of core-shell structure (box 1) and the *c*-plane intergranular phase (box 2) as shown in Fig. 9(a). The interface of core-shell structure in the 2:14:1 phase can be clearly observed. The chemical composition obtained from the interface of the core-shell structure shown in Fig. 9(c) indicates the composition in the shell of 2:14:1 phase is close to $Nd_{8.6}Ce_{2.6}Fe_{79.8}Co_{2.55}B_{6.3}$ while that in the core part is identified to be $Nd_{2.0}Ce_{9.9}Fe_{79.4}Co_{2.75}B_{5.8}$. The compositional analyses of these core-shell structure in the 2:14:1 phases are in good agreement with the stoichiometric composition of the $(Nd,Ce)_2Fe_{14}B$ phase, indicating the atom probe analysis is quantitatively reliable. x of the $(Nd_xCe_{1-x})_2Fe_{14}B$ shell was determined to be ~0.77, which is consistent with the STEM-EDS results shown in Fig. 7(f). It is shown in Figs. 9(a-b) that the *c*-plane intergranular phase is enriched considerably with Nd and slightly with Ce. The compositional profile taken across the *c*-plane

intergranular phase presented in Fig. 9(d) shows ~61.6 at.% of ferromagnetic elements (Fe+Co) and 20.8 at.% Nd+5.1 at.% Ce, which suggests this grain boundary phase should be weak ferromagnetic [27].

5.3 Discussion

Even though the $Ce_2Fe_{14}B$ phase adopts the same crystal structure (*$P4_2/mnm$*) as that of $Nd_2Fe_{14}B$, Ce is known to have different magnetism from Nd in the 2:14:1 phase, *i.e.*, Nd is trivalent in $Nd_2Fe_{14}B$, while Ce has a mixed valence state of ~3.44 in $Ce_2Fe_{14}B$ [28]. This makes the single phase unstable in the broad region in the $Nd_2Fe_{14}B$-$Ce_2Fe_{14}B$ quasi-binary system [29]. $CeFe_2$ is stably formed in the solidification process of Fe-Ce-B, whereas the $NdFe_2$ is not stable in the Nd-Fe system [30]. In the as-deformed Ce-Fe-B magnets, the $CeFe_2$ is evenly distributed in the microstructure as isolated grains (shown in Fig. 2(a)). $CeFe_2$ is a cubic Laves phase, ferromagnetic with a Curie temperature of ~235K [29], which is paramagnetic at room temperature. The formation of the $CeFe_2$ phase would lead to the excessive consumption of Ce that is required for the formation of Ce-rich grain boundary phase. This results in the formation of the ferromagnetic grain boundary phase with low concentration of Ce as shown in Fig. 7(a), which causes intergranular exchange coupling with a weak pinning force against the domain wall motion in magnetization reversals. Consequently, only a very low coercivity is obtained in the as-deformed Ce-Fe-B magnets as shown in Fig. 1(a).

After 10 wt.% Nd-Cu grain boundary infiltration, the aspect ratio of the grains is reduced from ~3.75 in the as-deformed sample to ~1.98 in the infiltrated sample (Table 1). It should be noteworthy that this result appears to be not consistent with the previous report on the Nd-Cu infiltrated Nd-Fe-B hot-deformed magnets [14], in which no noticeable change was observed in the aspect ratio of grains. The reduced aspect ratio of the grains is believed to be beneficial to reduce the effective demagnetization factor, resulting in higher coercivity [31]. More importantly, the concentration of ferromagnetic elements (Fe+Co) is reduced from ~78 at.% to ~60.2 at.% in the *c*-plane grain boundary phase and from ~ 76 at.% to ~62.2 at.% in the side-plane grain boundary phase. The dilution of ferromagnetic elements and enrichment of rare earth elements in the grain boundary phases strengthens the pinning force against the reversed magnetic domain wall displacement in process of magnetization reversal [32]. Moreover, the formation of Nd-rich shell shown in Fig. 4 in the 2:14:1 grains after the Nd-Cu infiltration leads to a strengthened

magnetocrystalline anisotropy because the $Nd_2Fe_{14}B$ has an anisotropy field higher than that of $Ce_2Fe_{14}B$. Therefore, the coercivity is enhanced drastically from ~8 $\times 10^{-4}$ T to ~0.5 T after the 10 wt.% Nd-Cu infiltration. Further increase in the amount of Nd-Cu infiltration to 40 wt.% led to only a slight increase in RE concentration from ~30.1 at.% to ~38.1 at.% while the concentration of RE in side-plane intergranular phase is almost unchanged. Therefore, the thin intergranular phases are likely to be ferromagnetic. STEM-EDS line profiles shown in Figs. 7 and 8 indicate that the composition of the Nd-rich shell in the 10 wt. % Nd-Cu infiltrated sample is ~$(Nd_{0.67}Ce_{0.33})_2Fe_{14}B$ while this shell shows a composition of ~ $(Nd_{0.85}Ce_{0.15})_2Fe_{14}B$ in the 40 wt. % infiltrated sample as shown in Table 2. Increase in Nd content in the shell leads to a larger magnetocrystalline anisotropy field in the shell region. Nevertheless, the coercivity change in the samples with 10 wt% and 40 wt.% infiltrations is very little.

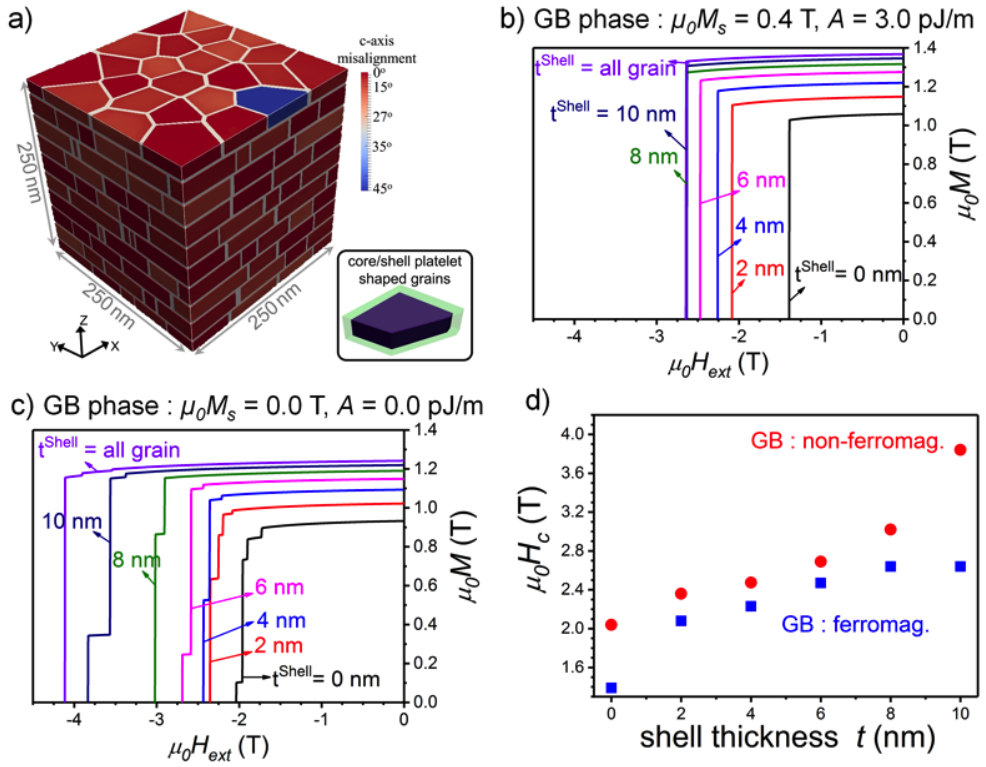

Figure 10 (a) Modeled Ce-Fe-B magnet with platelet shaped $Ce_2Fe_{14}B$ grain. Each grain shows a $Ce_2Fe_{14}B$ core/$Nd_2Fe_{14}B$ shell structure as shown in inset. One of the grains was assumed to be largely misaligned. Demagnetization curves of modeled hot-deformed magnet with different thickness of Nd-rich shell with (b) ferromagnetic grain boundary phase and (c) non-ferromagnetic grain boundary phase;(d) Dependence of coercivity on shell thickness.

In order to understand how the thickness and the composition of the $(Nd_xCe_{1-x})_2Fe_{14}B$ shell influence the coercivity of the hot-deformed magnets, micromagnetic simulations were carried out for various possible microstructures in Nd-Cu infiltrated Ce-Fe-B hot-deformed magnets. Intrinsic magnetic properties of the $(Nd_xCe_{1-x})_2Fe_{14}B$ shell was chosen by assuming a linear change of anisotropy field and saturation magnetization for $(Nd_{1-x}Ce_x)_2Fe_{14}B$ as function of x. Based on our experimental results, we assumed grain boundary phase to be weakly ferromagnetic with $\mu_0 M_s$=0.4 T, A=3 pJ/m and K_u =0.0 MJ/m^3. We also compared the result in the case of non-ferromagnetic grain boundary phase with $\mu_0 M_s$=0.00 T, A=0.00 pJ/m and K_u =0.0 MJ/m^3.

Figure 10(a) shows modeled sample with a size of 250×250×250 nm^3 containing 250 platelet shaped grains separated with a ~3-5 nm thick grain boundary phase. Tetrahedron meshes with a size of ~2 nm were applied on the model. Simulated demagnetization curves of the hot-deformed magnets with different thicknesses of the $(Nd_xCe_{1-x})_2Fe_{14}B$ shell for ferromagnetic and non-ferromagnetic grain boundary phases are shown in Fig. 10 (b) and (c). In these simulations, we assumed that the shell region is the $Nd_2Fe_{14}B$ phase and the core region is the $Ce_2Fe_{14}B$ phase. The micromagnetic simulation shows that coercivity is enhanced by increasing the thickness of the Nd-rich shell to 8 nm when the ferromagnetic grains are exchange coupled. Thereafter, no enhancement of coercivity is observed as shown in Fig. 10(d). However, if the 2:14:1 grains are exchange decoupled, thicker Nd-rich shell results in a larger coercivity as shown in Fig. 10(d). This result indicates that the increase of the thickness of Nd-rich shell in the Ce-Fe-B based hot-deformed magnet does not necessarily lead to an enhancement of coercivity as long as the grain boundary phase is ferromagnetic, which is the case for the samples in this work.

Figure 11 (a) shows simulated coercivity versus x in the $(Nd_xCe_{1-x})_2Fe_{14}B$ shell for ferromagnetic and non-ferromagnetic intergranular phase. In this simulation, we fixed the thickness of the shell to be 4 nm. It can be seen that the coercivity of the Ce-Fe-B based exchange coupled hot-deformed magnet increases almost linearly when Nd content in the shell increases to x=0.6. However, it starts to saturate for x>0.6. The green marked area and blue marked region in figure 11(a) correspond to the composition range of the $(Nd_xCe_{1-x})_2Fe_{14}B$ shell measured experimentally in the 10 wt. % and 40 wt.% Nd-Cu infiltrated Ce-Fe-B magnet, respectively. This shows that we cannot gain large enhancement in coercivity of Ce-Fe-B hot-deformed magnets by introducing more Nd in the $(Nd_xCe_{1-x})_2Fe_{14}B$ shell as long as the intergranular phase is ferromagnetic, in agreement with our experimental results. When the intergranular phase becomes

non-ferromagnetic, the absolute value of coercivity is further enhanced. However, a saturation of coercivity is also observed in the exchange decoupled model for x>0.6. This suggests that the coercivity of the Nd-Cu infiltrated Ce-Fe-B magnet does not strongly depend on the shell composition for x>0.6. The reason for this can be understood by taking a look at the magnetization configuration of the models during the demagnetization process. Fig. 11 (b) shows magnetization configurations during magnetization reversal processes of the exchange coupled models with x=0 and x=1. In the case of the exchange coupled model with x=0, magnetization reversal starts from the grain boundary phase followed by a cascade propagation reversed domains through neighboring grains. For x=1, the nucleation site changes to the $Ce_2Fe_{14}B$ phase in the core/shell interface, and the nucleated domain is pinned at grain boundaries. This suggests that the formation of Nd-rich shell changes the nucleation site to the core/shell interface. For x>0.6, coercivity is mainly controlled by the nucleation field of the $Ce_2Fe_{14}B$ phase. A similar feature was observed when the grain boundary is non-ferromagnetic as shown in Fig. 11 (c). When no Nd-rich shell exists (x=0), nucleation starts from the corner of the $Ce_2Fe_{14}B$ grains, i.e., grain boundaries. When the $(Nd_xCe_{1-x})_2Fe_{14}B$ shell is formed, for example x=0.6 as shown in Fig. 11(c), the nucleation site changes to the core/shell interface. x = 0.6 for the $(Nd_xCe_{1-x})_2Fe_{14}B$ shell is sufficient to maximize the coercivity, since the magnetization reversal is no longer controlled by the anisotropy field of the shell for x > 0.6.

Table 2 Composition of Nd+Ce and Fe+Co in *c*-plane and side-plane grain boundary phase and x in Nd-rich $(Nd_xCe_{1-x})_2Fe_{14}B$ shell near *c*-plane and side-plane grain boundary phase in as-deformed and diffused samples.

samples	*c*-Plane GB phases			side-Plane GB phases		
	Nd+Ce	Fe+Co	x	Nd+Ce	Fe+Co	x
As-deformed	19.2 at.%	71.4 at.%	0	20.1 at.%	70.9 at.%	0
+10 wt.% Nd-Cu	30.1 at.%	63.2 at.%	0.67	28.2 at.%	65.5 at.%	0.6
+40 wt.% Nd-Cu	38.1 at.%	53.4 at.%	0.85	26.2 at.%	67.5 at.%	0.84

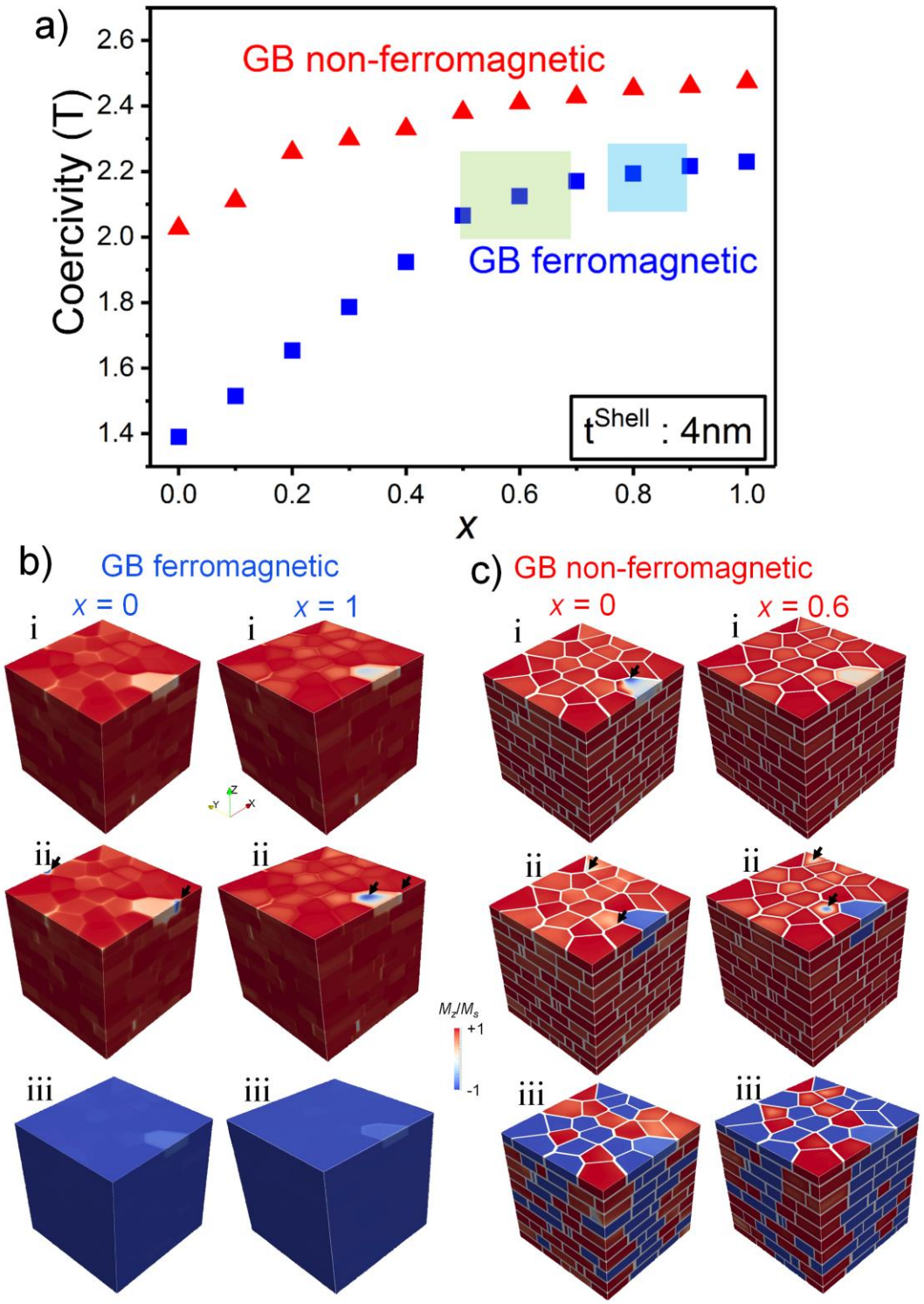

Figure 11. (a) Simulated coercivity versus x in 4nm thick $(Nd_xCe_{1-x})_2Fe_{14}B$ shell of exchange coupled and exchange decoupled models. Magnetization reversal process of models with (b)

As shown in Fig. 1(d), the temperature coefficient β is decreased from −0.57%/°C to −0.62%/°C with increasing Nd-Cu infiltration from 10 wt.% to 40 wt.%, indicating inferior thermal stability of coercivity in the sample infiltrated with 40 wt.% Nd-Cu. In general, the coercivity can be phenomenologically expressed by $H_c(T) = \alpha H_A(T) - N_{eff} M_s(T)$, where H_A(T) and M_s(T) are the anisotropy field and the saturation magnetization at various temperatures, α describes the lowered anisotropy field caused by defects at grain boundaries, and N_{eff} is the effective demagnetizing factor [33]. Even though the temperature dependence of the anisotropy field is more or less the same for $Nd_2Fe_{14}B$ and $Ce_2Fe_{14}B$, the coefficient of temperature dependence of M_s for $Nd_2Fe_{14}B$ is (−0.12%/°C), which is much larger than that for $Ce_2Fe_{14}B$ (−0.31%/°C). Based on the formula described above, a larger negative slope for temperature dependence of the saturation magnetization will be beneficial for a better thermal stability of coercivity. With increasing amount of Nd-Cu infiltration, the areal fraction of Nd-rich shell and x in Nd-rich shell increase simultaneously as shown in Tables 1 and 2, then the larger saturation magnetization and better thermal stability of saturation magnetization are reasonably expected. Therefore, the thermal stability of coercivity becomes worse in the sample infiltrated with 40 wt.% Nd-Cu.

5.4 Conclusion

The coercivity of hot-deformed Ce-Fe-B magnet was substantially increased from ~8×10^{-4} T to ~0.5 T by the grain boundary infiltration of 10 wt.% Nd-Cu. The detailed microstructure characterization using SEM, STEM/EDS and 3DAP have shown the formation of Nd-rich $(Nd_xCe_{1-x})_2Fe_{14}B$ shell in 2:14:1 grains and enriched concentration of rare earth elements in the intergranular phases. Further increase of Nd-Cu infiltration to 40 wt.% resulted in only a slight increase (~0.2 T) in coercivity. The micromagnetic simulations revealed that a further increase x in the $(Nd_xCe_{1-x})_2Fe_{14}B$ shell and increase in the areal fraction of the shell causes only a slight increase in coercivity as long as the thin intergranular phases are ferromagnetic, in agreement with the experimental observations. Besides, the thermal stability of coercivity is degraded with increasing amount of Nd-Cu infiltration because of larger stray field from the shell. For further enhancement of coercivity, exchange decoupling of the 2:14:1 grains by forming nonferromagnetic grain boundary phase is essential.

Reference

[1] O. Gutfleisch, M.A. Willard, E. Brück, C.H. Chen, S.G. Sankar, J.P. Liu, Adv. Mater. 23 (2011) 821–842.

[2] S. Sugimoto, J. Phys. Appl. Phys. 44 (2011) 064001.

[3] J.M.D. Coey, IEEE Trans. Magn. 47 (2011) 4671–4681.

[4] M. Zhang, Z. Li, B. Shen, F. Hu, J. Sun, J. Alloys Compd. 651 (2015) 144–148.

[5] C. Yan, S. Guo, R. Chen, D. Lee, A. Yan, IEEE Trans. Magn. 50 (2014) 1–5.

[6] X. Fan, S. Guo, K. Chen, R. Chen, D. Lee, C. You, A. Yan, J. Magn. Magn. Mater. 419 (2016) 394–399.

[7] K. Hono, H. Sepehri-Amin, Scr. Mater. 67 (2012) 530–535.

[8] K. Pei, X. Zhang, M. Lin, A. Yan, J. Magn. Magn. Mater. 398 (2016) 96–100.

[9] A.K. Pathak, M. Khan, K.A. Gschneidner, R.W. McCallum, L. Zhou, K. Sun, K.W. Dennis, C. Zhou, F.E. Pinkerton, M.J. Kramer, V.K. Pecharsky, Adv. Mater. 27 (2015) 2663–2667.

[10] Z. Chen, Y.K. Lim, D. Brown, IEEE Trans. Magn. 51 (2015) 1–4.

[11] R.-Q. Wang, X. Shen, Y. Liu, J. Li, IEEE Trans. Magn. 52 (2016) 1–6.

[12] J.F. Herbst, Rev. Mod. Phys. 63 (1991) 819–898.

[13] H. Sepehri-Amin, T. Ohkubo, T. Nishiuchi, S. Hirosawa, K. Hono, Scr. Mater. 63 (2010) 1124–1127.

[14] H. Sepehri-Amin, T. Ohkubo, S. Nagashima, M. Yano, T. Shoji, A. Kato, T. Schrefl, K. Hono, Acta Mater. 61 (2013) 6622–6634.

[15] T. Akiya, J. Liu, H. Sepehri-Amin, T. Ohkubo, K. Hioki, A. Hattori, K. Hono, Scr. Mater. 81 (2014) 48–51.

[16] L. Liu, H. Sepehri-Amin, T. Ohkubo, M. Yano, A. Kato, T. Shoji, K. Hono, J. Alloys Compd. 666 (2016) 432–439.

[17] L. Liu, H. Sepehri-Amin, T. Ohkubo, M. Yano, A. Kato, N. Sakuma, T. Shoji, K. Hono, Scr. Mater. 129 (2017) 44–47.

[18] K. Loewe, D. Benke, C. Kübel, T. Lienig, K.P. Skokov, O. Gutfleisch, Acta Mater. 124 (2017) 421–429.

[19] X. Tang, R. Chen, W. Yin, J. Wang, X. Tang, D. Lee, A. Yan, Appl. Phys. Lett. 102 (2013) 072409.

[20] X. Tang, R. Chen, W. Yin, J. Wang, X. Tang, D. Lee, A. Yan, Scr. Mater. 88 (2014) 49–52.
[21] M. Ito, M. Yano, N. Sakuma, H. Kishimoto, A. Manabe, T. Shoji, A. Kato, N.M. Dempsey, D. Givord, G.T. Zimanyi, AIP Adv. 6 (2016) 056029.
[22] S. Hirosawa, Y. Matsuura, H. Yamamoto, S. Fujimura, M. Sagawa, H. Yamauchi, J. Appl. Phys. 59 (1986) 873–879.
[23] J.M.D. Coey, Magnetism and Magnetic Materials, Cambridge University Press, 2010.
[24] A.K. Pathak, M. Khan, K.A. Gschneidner, R.W. McCallum, L. Zhou, K. Sun, M.J. Kramer, V.K. Pecharsky, Acta Mater. 103 (2016) 211–216.
[25] S. Hock, Max-Planck-Institute for metals research, PhD Thesis, Inst. Phys. (1988) 118..
[26] X. Tang, H. Sepehri-Amin, T. Ohkubo, K. Hioki, A. Hattori, K. Hono, Acta Mater. 123 (2017) 1–10.
[27] A. Sakuma, T. Suzuki, T. Furuuchi, T. Shima, K. Hono, Appl. Phys. Express 9 (2016) 013002.
[28] T.W. Capehart, R.K. Mishra, G.P. Meisner, C.D. Fuerst, J.F. Herbst, Appl. Phys. Lett. 63 (1993) 3642–3644.
[29] A. Alam, M. Khan, R.W. McCallum, D.D. Johnson, Appl. Phys. Lett. 102 (2013) 042402.
[30] R. Marazza, P. Riani, G. Cacciamani, Inorganica Chim. Acta 361 (2008) 3800–3806.
[31] H. Sepehri-Amin, T. Ohkubo, K. Hono, Mater. Trans. 57 (2016) 1221–1229.
[32] J. Liu, H. Sepehri-Amin, T. Ohkubo, K. Hioki, A. Hattori, T. Schrefl, K. Hono, Acta Mater. 61 (2013) 5387–5399.
[33] H. Kronmüller, Phys. Status Solidi B 130 (1985) 197–203.

Chapter 6: High performance of Ce-substituted hot-deformed Nd-Fe-B magnets

6.1 Introduction

Nd-Fe-B-based magnets are critical components for energy efficient technologies such as wind turbines and traction motors of (hybrid) electric vehicles [1,2]. In general, 30-33 wt.% of rare earth elements (Nd, Dy) were consumed to produce Nd-Fe-B-based magnets. With increasing demand for Nd-Fe-B-based magnets, the potential for rising cost of critical elements (Nd, Dy) has been strengthened. Recently, Ce-substituted Nd-Fe-B magnets have attracted considerable interests for its potential to be a low cost permanent magnet because Ce is as cheap as 12% of Nd [3]. However, the intrinsic hard magnetic properties of $Ce_2Fe_{14}B$, $\mu_0 M_s$=1.17 T and $\mu_0 H_A$=3 T, much inferior to those of $Nd_2Fe_{14}B$ [4], dwarf its competence to replace the Nd-Fe-B counterparts. This is evidenced in some reports on sintered Ce-substituted (Ce_xNd_{1-x})-Fe-B magnets, in which with increasing Ce substitution, the coercivity was degraded with a small abnormal jump in coercivity at x=0.25 [5]. Hard magnetic properties of the Ce-substituted sintered magnet with x=0.25 can be further optimized to ~$\mu_0 H_c$=1.21 T and $\mu_0 M_r$=1.33 T using a dual alloy method [6], which are still inferior to those of the Nd-Fe-B-based magnets. Up to dates, there is no reports on magnetic properties of Ce-substituted magnets are comparable with those of Nd-Fe-B-based counterparts.

Hot-deformed magnets firstly proposed by Lee [7,8] comprising of ultrafine grains have drawn considerable interests because of their greater potential to achieve higher coercivity at elevated temperature as compared to sintered magnets [9]. Pathak *et al* [10] reported an optimized coercivity ~0.94 T in hot-deformed magnets with x=20 at.% Ce substituted magnets and further increase in x leads to a substantial reduction of coercivity [11], and only a very low coercivity of ~8×10^{-4} T was reported for hot-deformed Ce-Fe-B magnets. Given the relatively high anisotropy field of the $Ce_2Fe_{14}B$ phase (~3 T), the coercivity value reported for the hot-deformed Ce-Fe-B magnet is too low. Recently, the eutectic grain boundary diffusion process has widely been applied

to enhance the coercivity in HDDR, nanocomposite and hot-deformed magnets [12–17]. Ito *et al* and Tang *et al* reported that the coercivity of Ce-Fe-B hot-deformed magnets could be enhanced by the infiltration of an eutectic $Nd_{70}Cu_{30}$ alloy [18,19]. However, only ~ 7 kOe coercivity was obtained in diffused sample with 40 wt.% Nd-Cu diffusion because of formation of ferromagnetic intergranular phases. Further micromagnetic simulations demonstrated that formation of non-ferromagnetic intergranular phases is essential to develop high-coercivity Ce-containing 2:14:1 magnets. To explore the potential application of Ce-substituted magnets, the hard magnetic properties of Ce-substituted magnets should be superior or at least comparable to Nd-Fe-B counterparts. Up to dates, there are no reports on Ce-substituted magnets with comparable magnetic properties of Nd-Fe-B magents. Recent investigations on Ce-substituted Nd-Fe-B single crystals have shown that the intrinsic properties can be well preserved with up to ~15 at.% Ce substitution for Nd [20,21], indicating it is possible to produce high performance of Ce-substituted Nd-Fe-B magnets by controlling the microstructure. In this work, we produced high magnetic performance Ce-substituted hot-deformed magnets by varying x from 0 to 0.4. With 10 at.% Ce substitution, the magnetic properties of Ce-substituted magnets were superior to those of Nd-(Fe,Co)-B counterparts. Moreover, Co-free Ce-substituted hot-deformed magnets were also prepared to systematically investigate the role of Co.

6.2 Experimental procedure

The alloy ingots with the nominal composition of $(Ce_xNd_{1-x})_{13.4}Fe_{76.29}Co_{4.51}Ga_{0.50}B_{5.3}$ (at.%) (x=0, 0.1, 0.2, 0.3, 0.4) and $(Ce_xNd_{1-x})_{13.4}Fe_{80.8}Ga_{0.50}B_{5.3}$ (at.%) (x=0, 0.1, 0.2, 0.3) were prepared by induction melting high-purity constituent elements and casting to a Fe book mold. The ingots were melt-spun at 30 m/s to obtain ribbons. Hereafter, the as-melt-spun ribbons were compacted by hot-pressing at 650 °C under 380 MPa in vacuum, followed by die-upsetting at 850°C until their 75% height reduction were achieved. The magnetic properties were measured using SQUID-VSM. The microstructures were studied by a scanning electron microscope (SEM) on Carl Zeiss CrossBeam1540EsB and scanning transmission electron microscope (STEM) on a Titan G^2 80–200 system with a probe aberration corrector.

6.3 Results

6.3.1 Magnetic properties of Ce-substituted Co-doped magnets

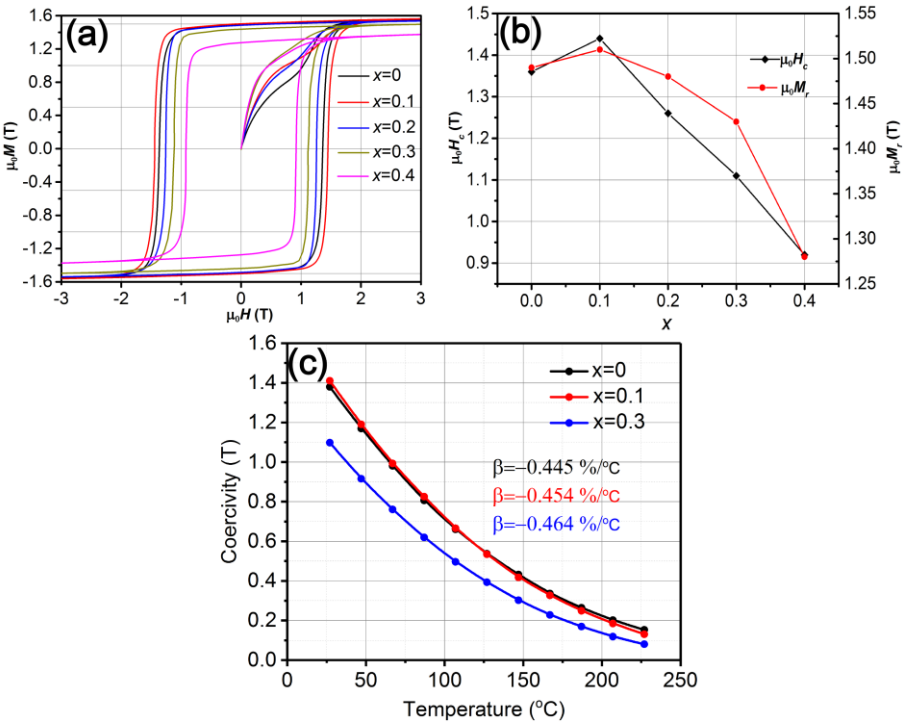

Fig. 1. (a) Hysteresis loops of Ce-substituted $(Ce_xNd_{1-x})_2(FeCo)_{14}B$ hot-deformed magnets (b) plots of magnetic properties against Ce substitution x and (c) temperature dependences of coercivities in Ce-substituted $(Ce_xNd_{1-x})_2(FeCo)_{14}B$ hot-deformed magnets with x=0, 0.1, 0.3.

Table 1. Magnetic properties of Co-doped Ce-substituted $(Ce_xNd_{1-x})_2(FeCo)_{14}B$ hot-deformed magnets.

Samples	$\mu_0 H_c$ (T)	$\mu_0 M_r$ (T)	$\mu_0 M_s$ (T)	$\mu_0 M_r/\mu_0 M_s$
x=0	1.36	1.49	1.59	0.94
x=0.1	1.45	1.50	1.60	0.94
x=0.2	1.26	1.46	1.56	0.93
x=0.3	1.11	1.42	1.54	0.92
x=0.4	0.92	1.28	1.43	0.89

Fig. 1(a) shows the hysteresis loops of Ce-substituted Nd-(FeCo)-B hot-deformed magnets with x from 0 to 0.4. It is seen that with 10 at.% Ce substitution, coercivity increased from 1.36 to

1.45 T as well as the remanence from 1.49 to 1.50 T. Further substitution of Ce for Nd led to degradations of magnetic properties. These trends are more visible in Fig. 1(b), which shows the coercivity and remanent magnetization peak at x=0.1 in a range of 0-0.4. Magnetic properties of these magnets is also included in table 1. As for thermal stability of coercivities, the plots of coercivities against temperatures (27-227°C) of Ce-substituted magnets with x=0, 0.1, 0.3 were shown in Fig. 1(c). It is seen that the coefficient of coercivity (β) was marginally degraded from -0.445 %/°C to -0.454 %/°C with increasing x from 0 to 0.1 and β further decreases to -0.464 %/°C in Ce-substituted magnets with x=0.3. It should be noted that thermal stabilities of coercivity in Ce-substituted samples is much better than that of Nd-Cu diffusion-processed hot-deformed Ce-Fe-B magnets reported in ref. [19].

6.3.2 Microstructure of Ce-substituted Co-doped magnets

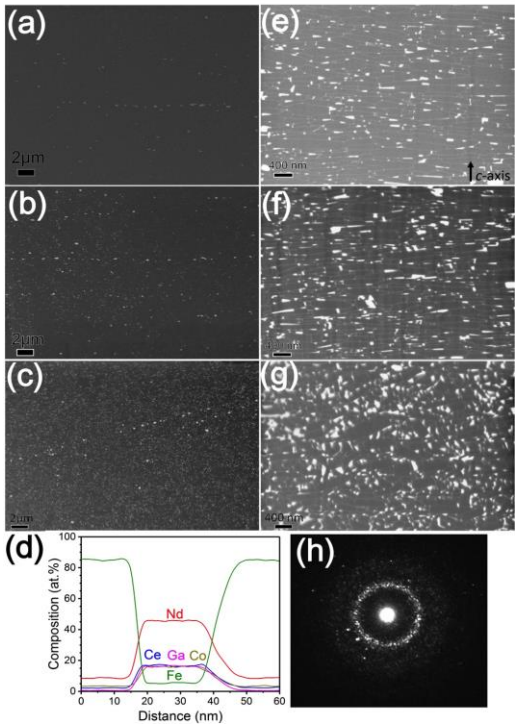

Fig. 2. Low magnification cross-sectional back scattered (BS) scanning electron microscopy (SEM) images of $(Ce_xNd_{1-x})_2(FeCo)_{14}B$ hot-deformed magnets with x=0 (a), x=0.1 (b) and x=0.3 (c); high magnification cross-sectional BSE SEM images taken from $(Ce_xNd_{1-x})_2(FeCo)_{14}B$ hot-deformed magnets with x=0 (e), x=0.1 (f) and x=0.3 (g); compositional profiles (d) and nanobeam electron diffraction pattern (h) taken from the one of typical secondary phase marked by arrow in image (g) in the $(Ce_xNd_{1-x})_2(FeCo)_{14}B$ hot-deformed magnets with x=0.3; c-axis is in-plane as the arrow indicates.

Fig. 2 shows overall microstructure of hot-deformed magnets with x=0, 0.1 and 0.3. Fig. 2(a-b) shows low magnification image of the Ce-free hot-deformed Nd-Fe-B magnets, there are some REO_x lined up on the interface of ribbons. Further high magnification BS SEM iamges shown in Figs. 2(e-f) indicates that platelet-like grains with c axis parallel to pressure direction can be formed after hot-deformation. For detailed comparison, the grain sizes of Ce-free and Ce-substituted magnets with x=0.1 were statistically calculated from Figs. 2(e-f). The average grain size of the Ce-free sample was measured as ~402 nm along the c-plane (D_c) and ~96 nm in the perpendicular direction (D_{ab}) to the c-plane. After 10 at.% Ce substitution, the grain size slightly decreases to ~393 nm in width (D_c) and to ~ 89 nm in height (D_{ab}), respectively. Further substitution with Ce for Nd leads to pronounced presence of grey-contrast secondary phase. Further high magnification BS SEM taken from 30 at.% Ce-substituted magnets presented in Fig. 2(g) shows that the large fraction of triple junction of RE-rich phase. The compositional analysis and nanobeam diffraction pattern taken from one of these typical RE-rich are shown in Fig. 2(d) and Fig. 2(h), respectively. It indicates this phase has an amorphous structure with chemical composition of ~$Nd_{45}Ce_{16}Fe_6Co_{16}Ga_{17}$. In addition, weak contrast from the grain boundary phase and a recognizable misalignment of grains can be observed in Fig. 2(g).

Figure 3 and Figure 4 show the STEM-HAADF images and STEM-EDS maps of Nd, Ce, Fe, Co, Ga in Ce-free and 10 at.% Ce substituted magnets. In Fig. 3, one can see that the white contrast from triple junction and grain boundaries in STEM-HAADF images implying heavier elements (i.e. rare earth element) segregate in these areas, which is confirmed by EDS map of Nd. It is shown that Nd was enriched in triple junction and grain boundaries where were depleted from Fe. Note that Co is preferentially segregated in some triple junction. Ga is found enriched with Nd in triple junction and grain boundaries to improve the wettability of grain boundary phases. In contrast, the EDS maps of Nd, Fe, Co and Ga in 10 at.% Ce-substituted magnets shown in Fig. 4 reveal the similar distribution behaviors with those in Ce-free magnets, implying that Ce substitution for Nd has a negligible influence on elemental distribution. In the map of Ce, Ce is enriched in the triple junction and grain boundaries, which shows the similar distribution with that of Nd. It should be noted here that instead of core-shell-structured 2:14:1 phases in Nd-Cu processed Ce-Fe-B magnets [19], Nd and Ce are uniformly distributed in 2:14:1 phases in 10 at.% Ce-substituted hot-deformed sample.

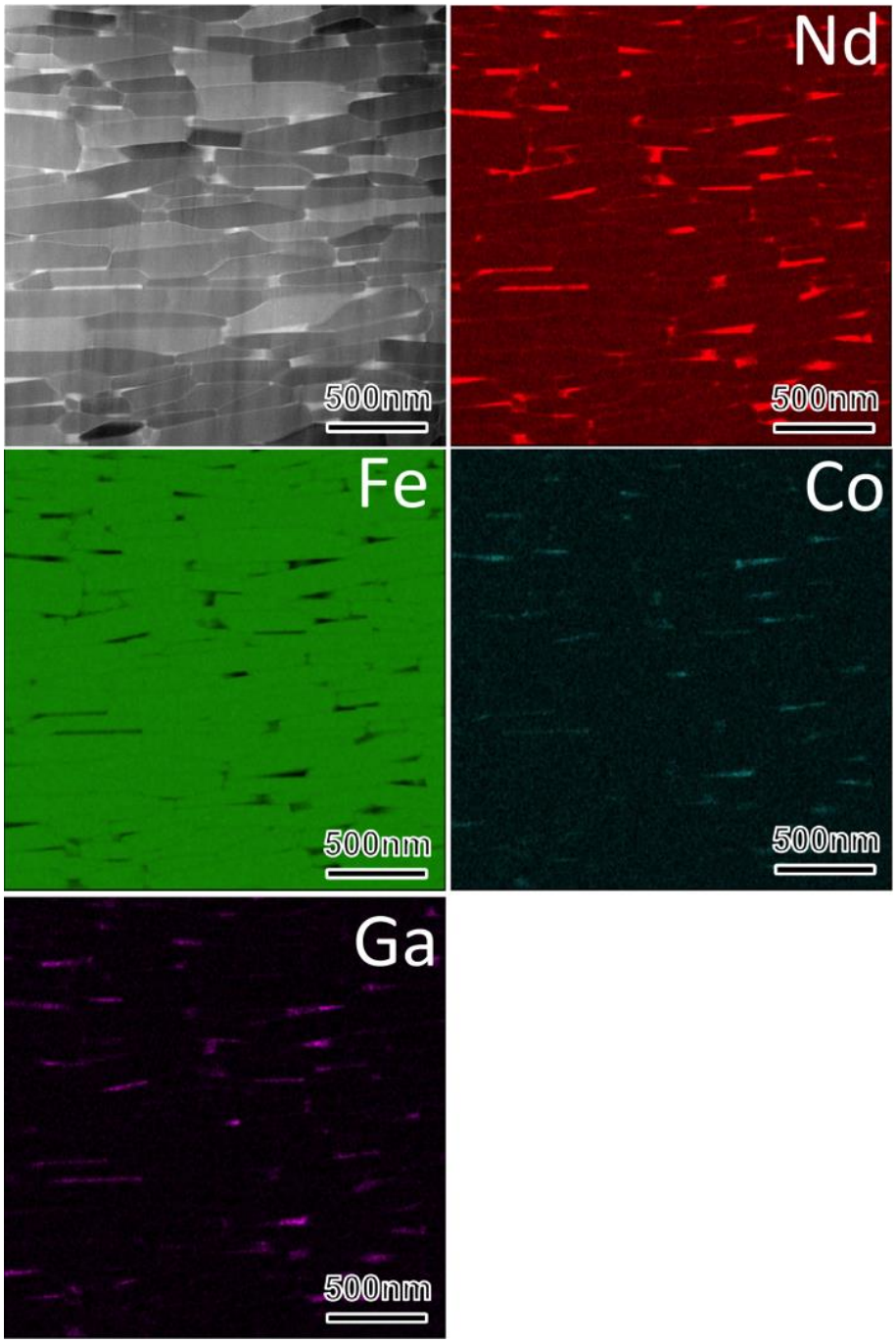

Fig. 3 HAADF images and STEM-EDS elemental mappings of Nd, Fe, Co, Ga, and Ce in $(Ce_xNd_{1-x})_2(FeCo)_{14}B$ hot-deformed magnets with x=0.

Fig. 5 presents high-resolution STEM-HAADF images obtained from the *c*-plane intergranular phase of two 2:14:1 grains in the Ce-substituted magnets with x=0, 0.1, and 0.3. The line scan EDS profiles taken across *c*-plane grain boundaries in Fig. 5(a-c) are shown Fig. 5(d-f),

respectively. In Fig. 5(a), a grain boundary phase with a thickness of ~1-2 nm is observed in high-resolution STEM-HAADF image. The inset STEM-EDS map of Nd+Fe shows a strong

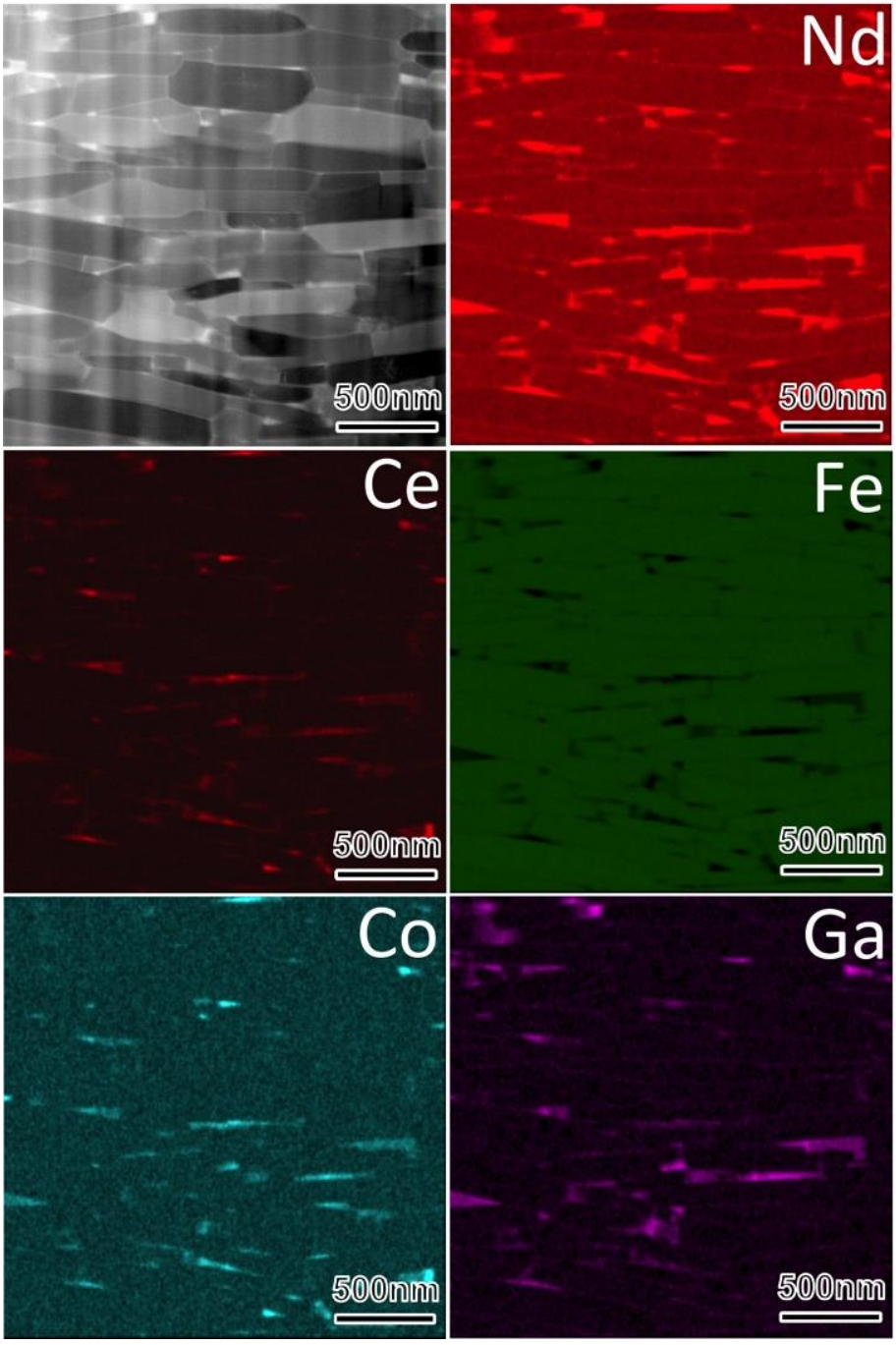

Fig. 4 HAADF images and STEM-EDS elemental mappings of Nd, Fe, Co, Ga, and Ce in $(Ce_xNd_{1-x})_2(FeCo)_{14}B$ hot-deformed magnets with x=0.1.

enrichment of Nd with depletion of Fe in this grain boundary phase. Further compositional profile taken across this grain boundary phase shown in Fig. 5(d) reveals that 54.2 at.% of Nd enrichment is found in grain boundary phase. Fig. 5(b) shows one of the typical grain boundary phase

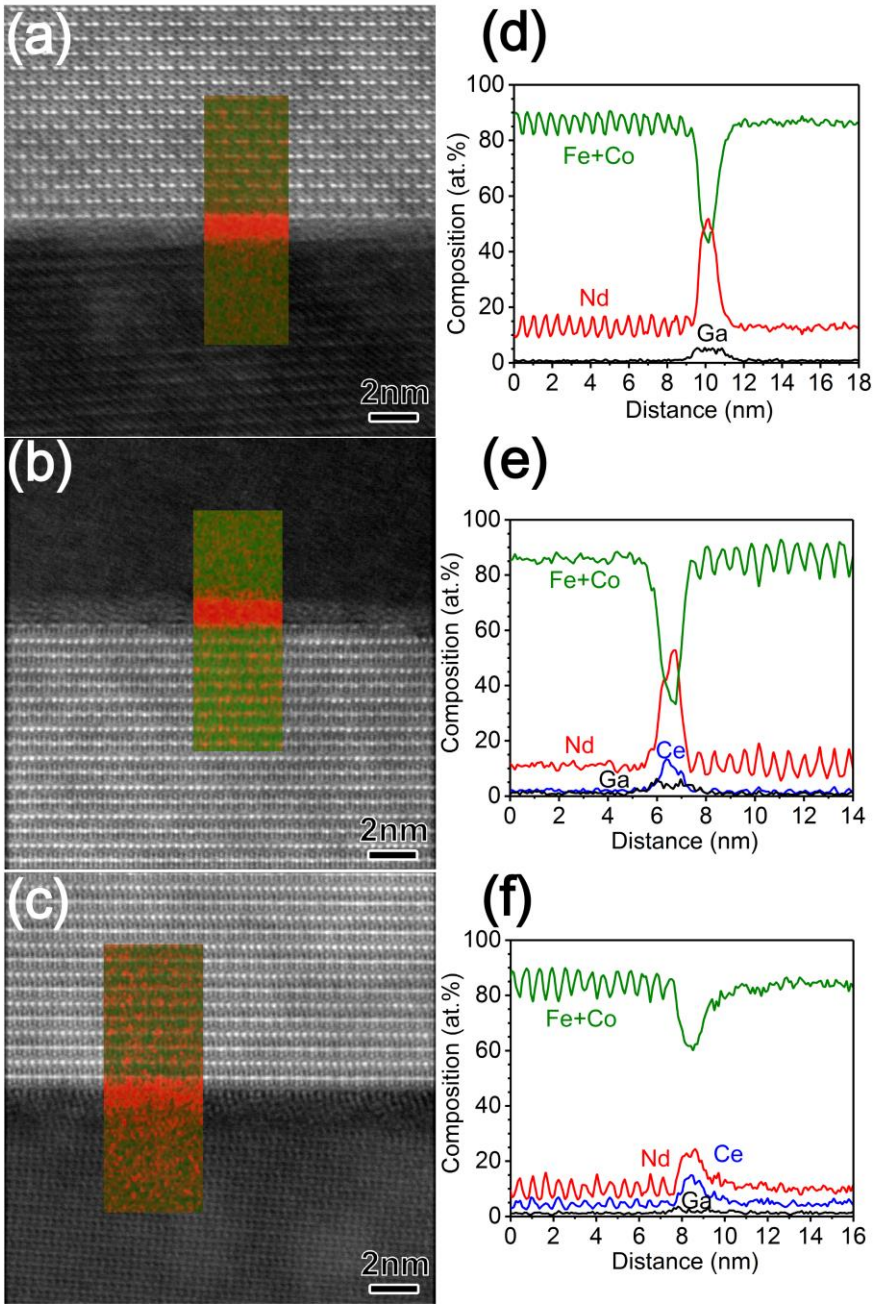

Fig. 5. High-resolution (HR) STEM images and inset of EDS maps of Nd+Fe obtained from *c*-plane grain boundary phases in $(Ce_xNd_{1-x})_2(FeCo)_{14}B$ hot-deformed magnets with x=0 (a), x=0.1 (b) and x=0.3 (c); (d-f) line scan profile taken across the interfaces in (a-c), respectively.

in the sample with 10 at.% Ce substitution for Nd; the contrast from the STEM-EDS map of Nd+Fe shows a uniform distribution of Nd in the 2:14:1 phase meaning no core-shell structure is formed in matrix phase. This is further confirmed by the compositional profile obtained across

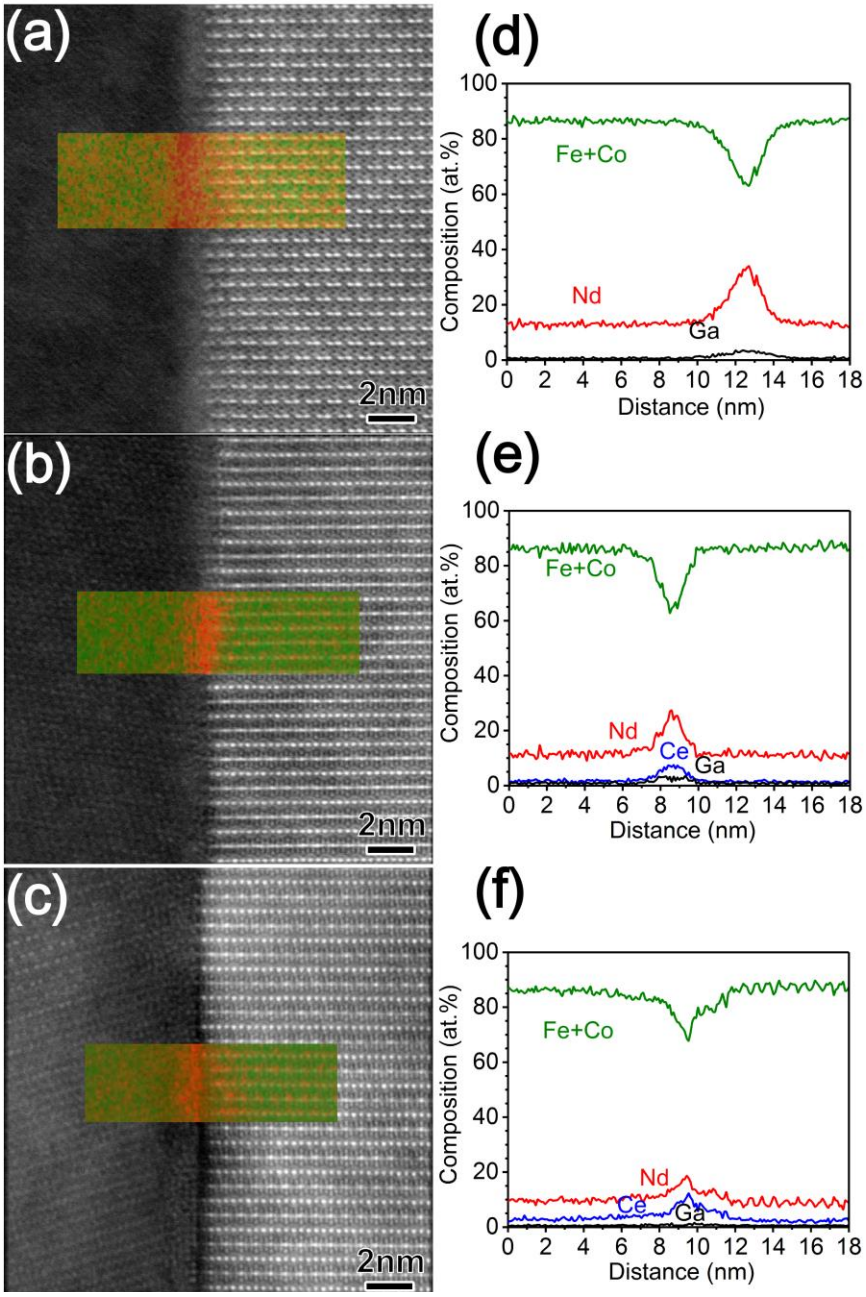

Fig. 6. HR-STEM images and inset of EDS maps of Nd+Fe obtained from side-plane grain boundary phases in $(Ce_xNd_{1-x})_2(FeCo)_{14}B$ hot-deformed magnets with x=0 (a), x=0.1 (b) and x=0.3 (c); (d-f) line scan profile taken across the interfaces in (a-c), respectively.

this grain boundary phase shown in Fig. 5(e), in which the RE concentration is consisted of 51.1 at.% of Nd and 10. 2 at.% of Ce. The total RE concentration is slightly higher than that in Ce-free magnets as shown in Fig. 5(d). By averaging the Ce line scan profile in 2:14:1 phase in EDS profiles of Fig. 5(e), 1.5 at.% of Ce concentration is found in matrix phase. With Ce substitution up to 30 at.%, a thinner grain boundary phase with weaker contrast can be found in high resolution HAADF image as shown in Fig. 5(c), which can be further confirmed by inset EDS map of Nd+Fe. By taking compositional analysis across this grain boundary phase, a total RE concentration of 39.3 at.% consisting of 24.1 at.% of Nd and 15.2 at.% of Ce is found in this thin *c*-plane intergranular phase. This is considerably lower than those in Ce-free and 10 at.% Ce-substituted magnets. As a result, very weak contrast from grain boundary was documented in Fig. 2(e).

Fig. 6 shows high-resolution STEM-HAADF images obtained from side-plane grain boundaries of 2:14:1 grains and EDS line scan compositional profiles taken from intergranular phases in the Ce-substituted magnets with x=0, 0.1, and 0.3. The compositional profile in Fig. 6(d) indicates that 33.8 at.% of Nd is segregated in this side-plane grain boundary, which is much lower than that in *c*-plane grain boundary as shown in Fig. 5(d). This is consistent with our previous results [22]. With 10 at.% Ce substitution for Nd, RE concentration in side-plane grain boundary phase is almost kept unchanged, comprising of 25.1 at.% of Nd and 7.5 at.% of Ce. Further increase x to 0.3, leads to presence of large areal fraction of secondary phase. As a result, the concentration of rare earth elements declines to 27.1 at.% consisting of 16.3 at.% Nd and 10.8 at.% Ce as shown in Fig. 6(f).

6.3.3 Magnetic properties of Ce-substituted Co-free magnets

To investigate the influence of Co on magnetic properties, Co-free Ce-substituted $(Nd_{1-x}Ce_x)_2Fe_{14}B$ magnets were also prepared. Fig. 7(a) shows the hysteresis loops of Co-free Ce-substituted $(Nd_{1-x}Ce_x)_2Fe_{14}B$ magnets. In the Ce-Co-free hot-deformed magnet, a coercivity of 1.35 T with remanent magnetization of 1.51 T was obtained, after 10 at.% Ce substitution, the coercivity is substantially degraded to 0.94 T accompanied with a small degradation to 1.48 T in remanent magnetization. With increasing x to 0.2, coercivity is slightly recovered to 1.06 T with a reduction of 0.04 T in remanent magnetization. Further increase of x leads to a simultaneous deterioration of coercivity and remanent magnetization. Consequently, a downward trend in

remanent magnetization with increasing x is shown in Fig. 7(b). It is seen in Fig. 7(b) that the coercivity decreases substantially firstly and increases slightly to 1.06 T at x=0.2 followed by a downward tendency with further increasing x. Table 2 summarizes all the magnetic properties in Co-free Ce-substituted magnets. The trends of magnetic properties are consistent with other reports on Co-free Ce-substituted magnets [5].

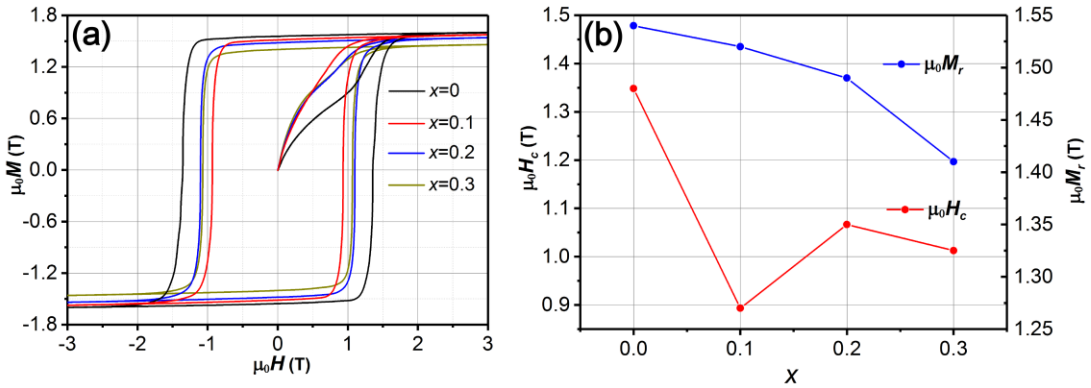

Fig. 7. (a) Hysteresis loops of Co-free Ce-substituted $(Ce_xNd_{1-x})_2Fe_{14}B$ hot-deformed magnets and (b) plots of magnetic properties against Ce substitution x.

Table 2. Magnetic properties of Co-free Ce-substituted $(Ce_xNd_{1-x})_2Fe_{14}B$ hot-deformed magnets.

Samples	μ_0H_c (T)	μ_0M_r (T)	μ_0M_s (T)	μ_0M_r/μ_0M_s
x=0	1.35	1.51	1.60	0.94
x=0.1	0.94	1.48	1.58	0.94
x=0.2	1.06	1.44	1.54	0.93
x=0.3	1.05	1.36	1.46	0.93

6.3.4 Microstructure of Ce-substituted Co-free magnets

Fig. 8 shows the overall microstructure of Co-free Ce-substituted hot-deformed magnets with x=0.1 and 0.2. In Fig. 8(a), the low magnification of BS SEM in hot-deformed with x=0.1 shows that instead of NdO_x phase with bright contrast on the interface of ribbons [12,22,23], there is a phase with grey contrast marked by arrow appears on the interfaces of ribbons. To identify this phase, EDS compositional profiles and nanobeam diffraction patterns taken from this area are shown in Fig. 8(c) and (f), respectively. By indexing the diffraction patterns, the crystal structure of this phase is consistent with $(Nd,Ce)_6Fe_{13}Ga$ (*I4/mcm*). This is further confirmed by

compositional analysis indicated in Fig. 8(c). Due to presence of this $(NdCe)_6Fe_{13}Ga$, grain boundary phase with low RE concentration shows a weak contrast, which can be evidenced by high magnification of BS SEM image shown in Fig. 8(d). With increase x to 0.2, the formation of $(NdCe)_6Fe_{13}Ga$ phase is suppressed and a few of REO_x phases are observed on the interface of ribbons as shown in low magnification BS SEM image of Fig. 8(b). Moreover, with suppression of $(NdCe)_6Fe_{13}Ga$, the grain boundary phase can be more clearly imaged out in high magnification BS SEM of Fig. 8(d).

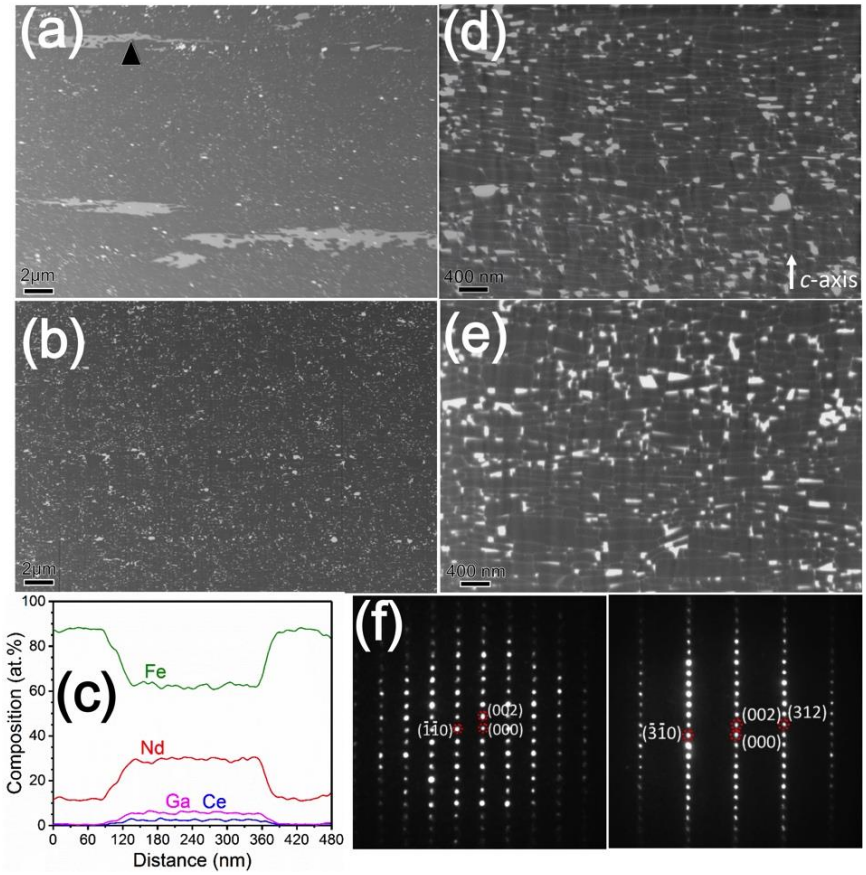

Fig. 8. Low magnification cross-sectional back scattered (BS) scanning electron microscopy (SEM) images of Co-free $(Ce_xNd_{1-x})_2Fe_{14}B$ hot-deformed magnets with x=0.1 (a) and x=0.2 (b); high magnification cross-sectional BSE SEM images taken from $(Ce_xNd_{1-x})_2Fe_{14}B$ hot-deformed magnets with x=0.1 (d), x=0.2 (e); compositional profiles (c) and nanobeam electron diffraction pattern (f) taken from the one of typical secondary phase marked by arrow in image (a) in the $(Ce_xNd_{1-x})_2(FeCo)_{14}B$ hot-deformed magnets with x=0.1; c-axis is in-plane as the arrow indicates.

Figure 9 and 10 show the STEM-HAADF images and STEM-EDS maps of Nd, Ce, Fe, Ga in Co-free Ce-substituted hot-deformed magnets with x=0.1 and 0.2. In STEM-HAADF images of Fig. 9, platelet-like 2:14:1 grains with gray contrast and brightly imaged RE-rich phase are clearly observed in STEM-HAADF images. It should be noted that contrast from grain boundary phase in the STEM-HAADF image of Fig. 10 is much clearer and brighter than that in Fig. 9, implying higher RE concentration in grain boundary phase can be obtained in hot-deformed sample with x=0.2. This is further confirmed by taking EDS map Fe shown in Fig. 10. In the map of Fe of Fig. 10, the networking of grain boundaries can be well formed and recognized, where is depleted from Fe and enriched with Nd and Ce. Ce has a similar distribution behavior with Nd in both samples and Ga is founded segregated in triple junction and grain boundaries. There is no core-shell structure can be found in 2:14:1 phases based on distributions of Nd, Fe and Ce in Figs. 9-10.

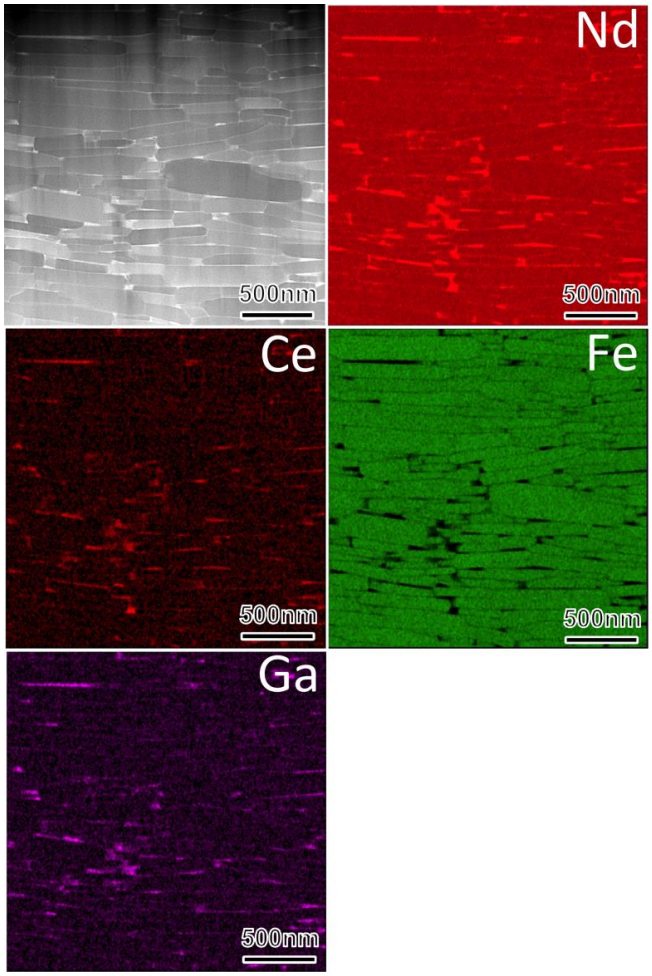

Fig. 9 HAADF images and STEM-EDS elemental mappings of Nd, Fe, Ga, and Ce in Co-free $(Ce_xNd_{1-x})_2Fe_{14}B$ hot-deformed magnets with x=0.1.

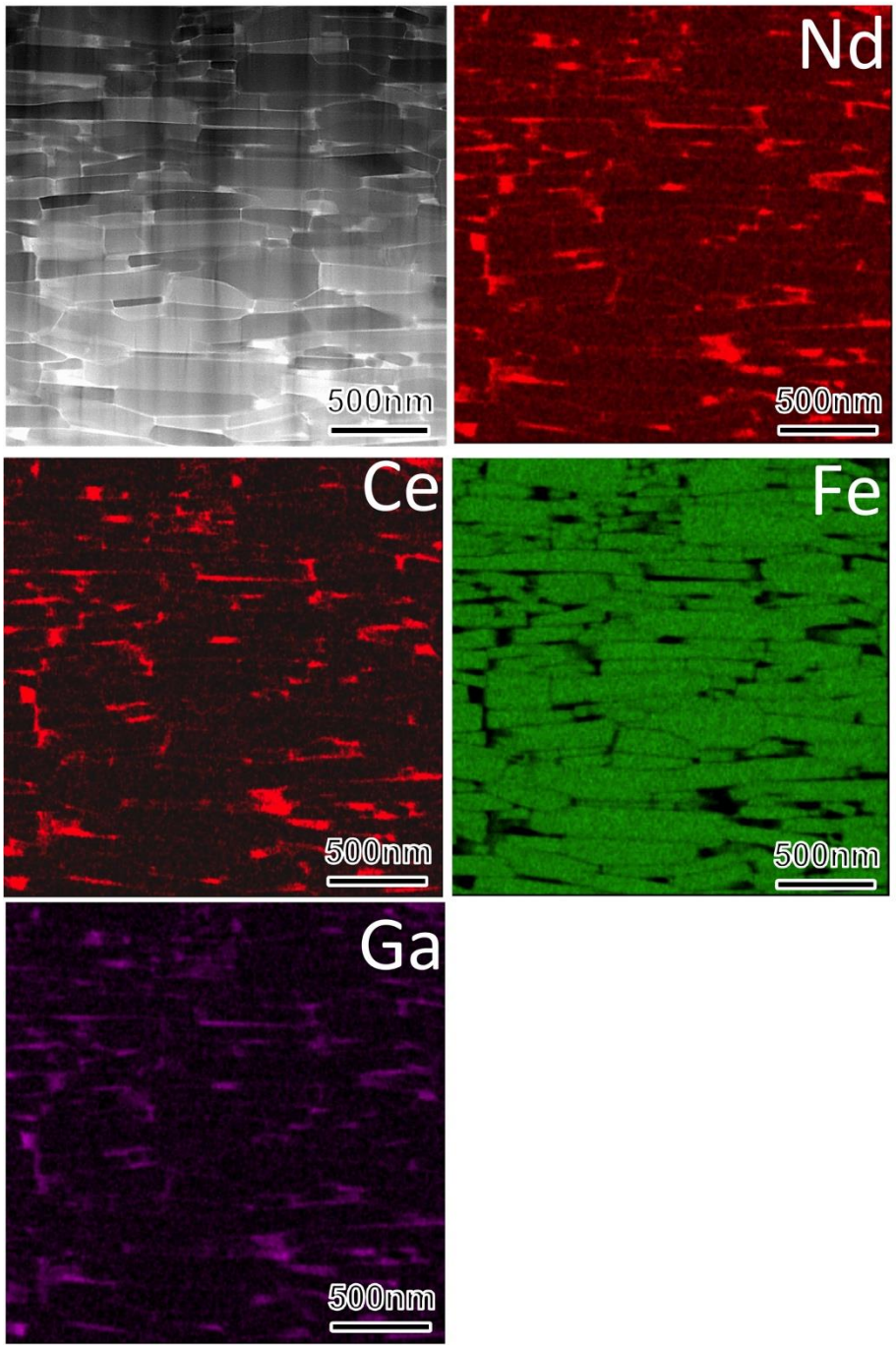

Fig. 10 HAADF images and STEM-EDS elemental mappings of Nd, Fe, Ga, and Ce in Co-free $(Ce_xNd_{1-x})_2Fe_{14}B$ hot-deformed magnets with x=0.2.

Fig. 11 shows the HR-STEM images obtained from the *c*-plane interfaces between two 2:14:1 grains in Co-free Ce-substituted hot-deformed magnets with x=0.1 and 0.2. The compositional profiles taken across *c*-plane grain boundaries in Ce-substituted magnets in Fig.

11(c-d) were obtained from inset EDS maps in Figs. 11(a-b), respectively. In Fig. 11(a), a thin grain boundary phase with thickness of 1 nm shows a weak contrast in the inset superimposed Nd+Fe EDS map, indicating a relatively low Nd concentration is segregated in this grain boundary phase, which is confirmed by taking a line scan composition across this grain boundary phase as shown in Fig. 11(c). The total RE concentration in this grain boundary phase is 40.2 at.%, comprising 33.9 at.% of Nd and 6.3 at. % of Ce. With x increase up to 0.2, a relatively thicker grain boundary phase with clearer contrast is shown in Fig. 11(b). Further compositional profiles shown in Fig. 11(d) indicate that Nd and Ce are strongly enriched in the intergranular phase. The concentrations of RE in this c-plane intergranular phase were determined to be ~64.3 at.%, consisting of 42.4 at.% of Nd and 21.9 at.% of Ce, considerably richer in RE compared to that in Ce-substituted sample with x=0.1. This is consistent with result shown in Fig. 10.

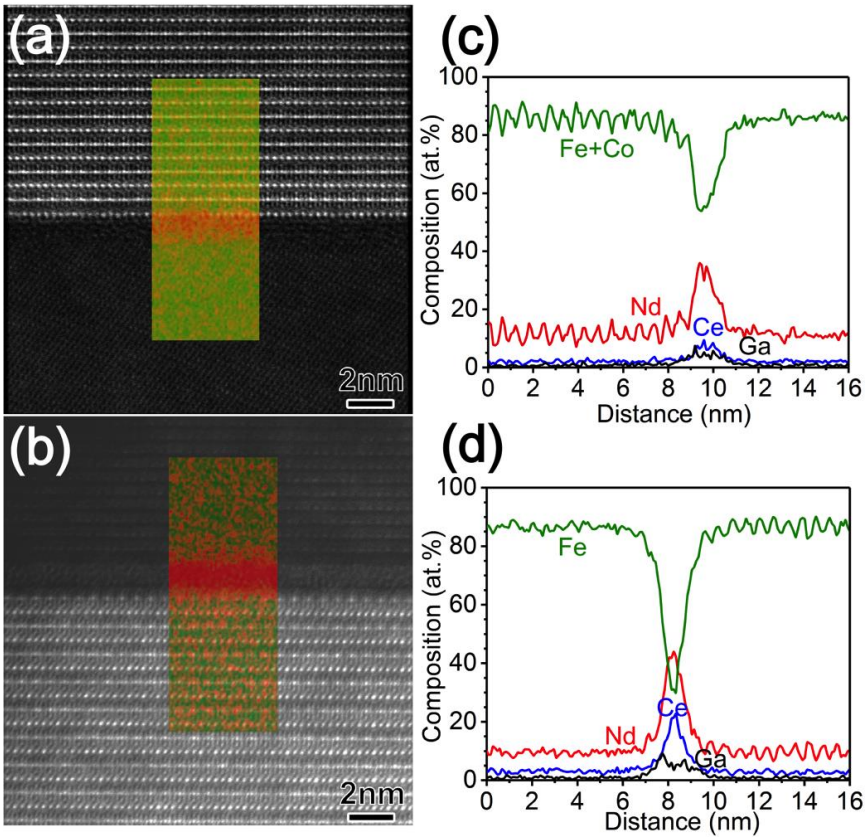

Fig. 11. High-resolution HAADF-STEM images and superimposed EDS mappings of typical RE-rich grain boundary phases in c-plane of Co-free $(Ce_xNd_{1-x})_2Fe_{14}B$ hot-deformed magnets with x=0.1 (a) and x=0.2 (b); (c-d) compositional profiles across the RE-rich grain boundary phase in (a-b), respectively.

Fig. 12 presents the HR-STEM-HAADF images taken in the side-plane interface of two 2:14:1 grains and EDS line scan compositional profiles taken across typical RE-rich intergranular phases in Co-free Ce-substituted hot-deformed samples with x=0.1 and 0.2. In Fig. 12(a), a thin intergranular phase are observed in side-plane grain boundary of sample with x=0.1, which is enriched with Nd and depleted from Fe as shown in inset image of Fig. 12(a). In comparison, the contrast from the intergranular phase in the side-plane grain boundary in Fig. 12(b) shows stronger intensity in the Nd+Fe mapping as compared to that in side-plane intergranular phases in Fig. 12(a), suggesting relatively higher Nd concentration in the side-plane intergranular phase with increasing x from 0.1 to 0.2. The total RE concentrations in these two side grain boundary phases are further determined by compositional profiles shown in Fig. 12(c-d), respectively. It is seen that RE concentration in side-plane grain boundary phase of sample with x=0.1 is determined to be 32.2 at.%, consisting of 25.3 at. % Nd and 6.9 at.% Ce, which is increased to 46.1 at.%, comprising of 27.4 at.% Nd and 18.7 at.% Ce in hot-deformed sample with x=0.2.

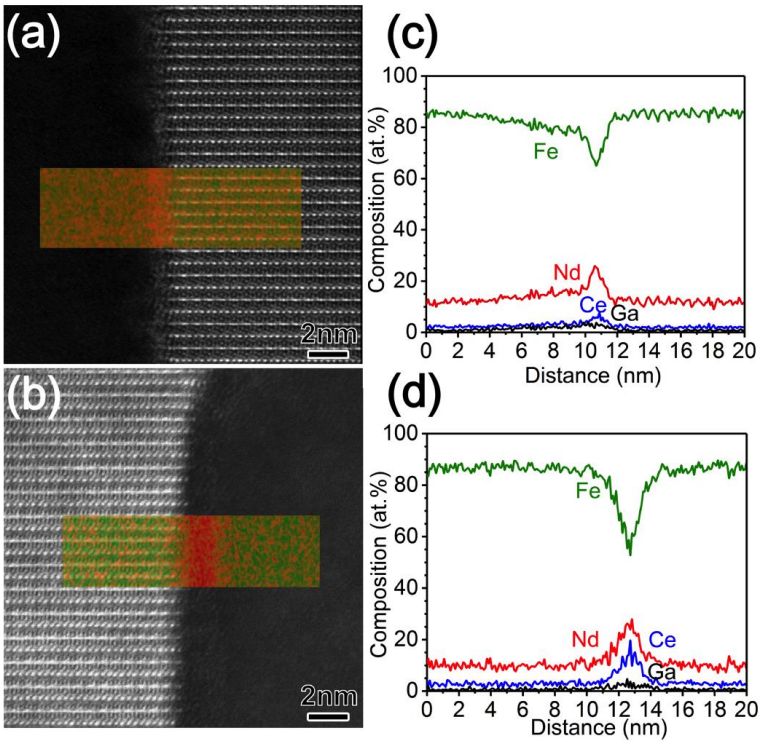

Fig. 12 High-resolution HAADF-STEM images and superimposed EDS mappings of typical RE-rich grain boundary phases in side-plane of Co-free $(Ce_xNd_{1-x})_2Fe_{14}B$ hot-deformed magnets with x=0.1 (a) and x=0.2 (b); (c-d) compositional profiles across the RE-rich grain boundary phase in (a-b), respectively.

6.4 Discussion

Table 3 Grain size (D_c, D_{ab}), coercivity ($\mu_0 H_c$), remanent magnetization ($\mu_0 M_r$), saturation magnetization ($\mu_0 M_s$) measured at 7 T and ratio between remanent magnetization and saturation magnetization in the co-doped Ce-free and Ce-substituted hot-deformed magnet with x=0.1.

Samples	D_c(nm)	D_{ab}(nm)	$\mu_0 H_c$ (T)	$\mu_0 M_r$ (T)	$\mu_0 M_s$ (T)	$\mu_0 M_r/\mu_0 M_s$
$Nd_2(FeCo)_{14}B$	402	96	1.36	1.49	1.50	0.94
$(Ce_{0.1}Nd_{0.9})_2(FeCo)_{14}B$	393	89	1.45	1.50	1.60	0.94

To exploit the potential application of Ce-substituted magnets, the hard magnetic properties of $(Ce_xNd_{1-x})_2(FeCo)_{14}B$ are required to be superior or at least comparable to those of $Nd_2(FeCo)_{14}B$ counterparts. Here we reported the high performance Ce-substituted Co-containing hot-deformed magnet with x=0.1, whose magnetic properties are superior to those of $Nd_2(FeCo)_{14}B$ counterparts. To investigate the origin of the enhancement of extrinsic properties by 10 at.% Ce substitution for Nd, the microstructures of $(Ce_{0.1}Nd_{0.9})_2(FeCo)_{14}B$ and $Nd_2(FeCo)_{14}B$ hot-deformed magnets are systematically compared. As shown in table 3, grain sizes of $Nd_2(FeCo)_{14}B$ hot-deformed magnets were statistically calculated from Fig. 2(e) to be D_{ab}=96 nm and D_c=402, which are slightly reduced to D_{ab}=89 nm and D_c=393 nm in $(Ce_{0.1}Nd_{0.9})_2(FeCo)_{14}B$, respectively. Chemistry of grain boundary phases is another important factor to influence the coercivity. ~54.2 at.% of Nd is found enriched in *c*-plane grain boundary phase in $Nd_2(FeCo)_{14}B$ hot-deformed magnets determined from Fig. 5(c), after 10 at.% Ce substitution, ~51.1 at.% of Nd alongside with 10. 2 at.% of Ce are segregated in *c*-plane grain boundary phases. The total rare earth concentration in *c*-plane grain boundary phase is slightly increased by 7.1 at.% after 10 at.% Ce substitution while the total rare earth concentration in side-plane grain boundary is almost same in these two sample. Ce is known to have different magnetism from Nd in the 2:14:1 phase, *i.e.*, Nd is trivalent in $Nd_2Fe_{14}B$, while Ce has a mixed valence state of ~3.44 in $Ce_2Fe_{14}B$ [24], giving rise to presence of secondary phase, *i.e.* $CeFe_2$ [5,19]. Here, no $CeFe_2$ phase can be observed in Ce-substituted hot-deformed magnets with x=0.1, which can be evidenced by microstructural observation shown in Fig. 2(b) and Fig. 4(b). With only 10 at.% Ce

substitution, the microstructure can be preserved intactly. Surprisingly, the enhancement of remanent magnetization was also observed in Fig. 1(b). Given the same microstructure as shown in Fig. 2, the enhancement of remanent magnetization in sample with x=0.1 is originated from slightly strengthened saturation magnetization. Hence, given the similar microstructure in these two samples, the enhancement of extrinsic properties in Ce-substituted Co-containing sample with x=0.1 may be stemmed from strengthened intrinsic properties. Recently, Susner *et al* [21] reported that the intrinsic properties can be preserved up to ~30 at.% Ce substitution in Co-free single crystals, but no reports on influence of intrinsic properties on Ce substitution in Co-doped single crystals. Further studies need to be done on intrinsic properties of Ce-substituted Co-containing single crystals. Upon increasing x to 0.3, there is a large areal fraction of Nd-Ce-Ga-rich phase with amorphous structure appears in the hot-deformed magnets as shown in Fig. 2(c). As a result, the coercivity and remenanet magnetization simultaneously drop to 1.11 T and 1.40 T, respectively. Good thermal stability is another criteria for high temperature applications, β is employed to characterize thermal stability of coercivity. As seen in Fig. 1(c), with 10 at.% Ce substitution for Nd, β marginally deteriorates from -0.445 %/°C to -0.454 %/°C and further decreases to -0.464 %/°C in Ce-substituted sample with x=0.3, suggesting influence of Ce substitution on thermal stability of coercivity in Co-doped samples is quite limited.

To examine the influence of Co on Ce-substituted magnets, the Co-free Ce-substituted hot-deformed magnets was also fabricated by varying x from 0 to 0.3. With 10 at.% substitution of Ce for Nd in Co-free sample, the coercivity was degraded substantially from 1.36 T to 0.94 T, which ascribed to presence of $(NdCe)_6Fe_{13}Ga$ shown in Fig. 8(a), which causes excessive consumption of RE required to form RE-rich grain boundary phases. Consequently, the resultant RE-lean grain boundary phases were formed as shown in Fig. 9(c) and Fig. 11(c). Further increasing x to 20 at.% in Co-free sample, the formation of $(NdCe)_6Fe_{13}Ga$ was effectively suppressed, leading to a significant increase in RE concentration in grain boundary phases as shown in Figs. 11(d) and 12(d), which is supposed to strengthen the pinning force against reversed magnetic domain propagation, resulting in an enhancement in coercivity. On the other hand, an increase in x may give rise to an increase in concentration of Ce in the 2:14:1 phase as shown in line scanning compositional profiles of Figs. 11-12, leading to inferior intrinsic properties as well as extrinsic properties in Co-free samples. Here, a degradation of coercivity caused by inferior intrinsic properties with increasing x from 0.1 to 0.2 was compensated by an enhanced coercivity resulted

from strengthened pinning force against reversed magnetic domains induced by an increase in RE concentration in grain boundary phases. As a result, a slightly higher coercivity can be obtained in Co-free Ce-substituted magnets with x=0.2. Further increase of x leads to a simultaneous deterioration of coercivity and remanent magnetization. As for comparison between $(Ce_{0.1}Nd_{0.9})_2(FeCo)_{14}B$ and $(Ce_{0.1}Nd_{0.9})_2Fe_{14}B$ magnets, with doping of Co, the formation $(NdCe)_6Fe_{13}Ga$ is significantly suppressed. The microstructure can be thus preserved intactly in $(Ce_{0.1}Nd_{0.9})_2(FeCo)_{14}B$ samples as shown in Figs. 2(b) and (f), as a result, a higher coercivity is achieved in $(Ce_{0.1}Nd_{0.9})_2(FeCo)_{14}B$.

6.5 Conclusion

The Co-doped and Co-free Ce-substituted hot-deformed magnets have been successfully fabricated to investigate role of Co in Ce substitution behaviors. In the Co-doped $(Ce_xNd_{1-x})_2(FeCo)_{14}B$ hot-deformed magnets, with x increasing to 0.1, the coercivity and remanent magnetization were simultaneously increased from 1.36 to 1.45 T and from 1.49 to 1.50 T, respectively. The coefficient of coercivity (β) was marginally degraded from -0.445 %/°C to -0.454 %/°C after 10 at.% Ce substitution. Further microstructure characterizations showed the microstructure and chemical compositions in the intergranular phases in 10 at.% Ce substituted hot-deformed magnet are similar to those in Ce-free hot-deformed magnet, indicating that the improved extrinsic properties in Ce-substituted hot-deformed magnet with x=0.1 may be stemmed from strengthened intrinsic properties. In Co-free Ce-substituted $(Ce_xNd_{1-x})_2Fe_{14}B$ magnets, downward tendencies in the coercivity and remanent magnetization can be obtained with a small jump in coercivity at x=0.2. This abnormal jump in the coercivity was attributed to suppression of $(CeNd)_6Fe_{13}Ga$ and resultant increased Nd content in grain boundary phases as well as strengthened pinning force against reversed magnetic domain wall motion obtained in Co-free Ce-substituted hot-deformed magnet with x=0.2. As for comparison between Co-doped $(Ce_{0.1}Nd_{0.9})_2(FeCo)_{14}B$ and Co-free $(Ce_{0.1}Nd_{0.9})_2Fe_{14}B$ magnets, the formation $(NdCe)_6Fe_{13}Ga$ is significantly suppressed and microstructure can be well preserved by doping Co. Higher coercivity can be thus obtained in Co-doped $(Ce_{0.1}Nd_{0.9})_2(FeCo)_{14}B$ hot-deformed magnets.

Reference

[1] O. Gutfleisch, M.A. Willard, E. Brück, C.H. Chen, S.G. Sankar, J.P. Liu, Adv. Mater. 23 (2011) 821–842.

[2] S. Sugimoto, J. Phys. Appl. Phys. 44 (2011) 064001.

[3] D.N. Brown, D. Lau, Z. Chen, AIP Adv. 6 (2016) 056019.

[4] J.F. Herbst, Rev. Mod. Phys. 63 (1991) 819–898.

[5] C. Yan, S. Guo, R. Chen, D. Lee, A. Yan, IEEE Trans. Magn. 50 (2014) 1–5.

[6] X. Fan, S. Guo, K. Chen, R. Chen, D. Lee, C. You, A. Yan, J. Magn. Magn. Mater. 419 (2016) 394–399.

[7] R. Lee, E. Brewer, N. Schaffel, IEEE Trans. Magn. 21 (1985) 1958–1963.

[8] R.W. Lee, Appl. Phys. Lett. 46 (1985) 790–791.

[9] K. Hono, H. Sepehri-Amin, Scr. Mater. 67 (2012) 530–535.

[10] A.K. Pathak, M. Khan, K.A. Gschneidner, R.W. McCallum, L. Zhou, K. Sun, K.W. Dennis, C. Zhou, F.E. Pinkerton, M.J. Kramer, V.K. Pecharsky, Adv. Mater. 27 (2015) 2663–2667.

[11] R.-Q. Wang, X. Shen, Y. Liu, J. Li, IEEE Trans. Magn. 52 (2016) 1–6.

[12] H. Sepehri-Amin, T. Ohkubo, S. Nagashima, M. Yano, T. Shoji, A. Kato, T. Schrefl, K. Hono, Acta Mater. 61 (2013) 6622–6634.

[13] H. Sepehri-Amin, T. Ohkubo, T. Nishiuchi, S. Hirosawa, K. Hono, Scr. Mater. 63 (2010) 1124–1127.

[14] K. Loewe, D. Benke, C. Kübel, T. Lienig, K.P. Skokov, O. Gutfleisch, Acta Mater. 124 (2017) 421–429.

[15] L. Liu, H. Sepehri-Amin, T. Ohkubo, M. Yano, A. Kato, N. Sakuma, T. Shoji, K. Hono, Scr. Mater. 129 (2017) 44–47.

[16] X. Tang, R. Chen, W. Yin, J. Wang, X. Tang, D. Lee, A. Yan, Appl. Phys. Lett. 102 (2013) 072409.

[17] X. Tang, R. Chen, W. Yin, J. Wang, X. Tang, D. Lee, A. Yan, Scr. Mater. 88 (2014) 49–52.

[18] M. Ito, M. Yano, N. Sakuma, H. Kishimoto, A. Manabe, T. Shoji, A. Kato, N.M. Dempsey, D. Givord, G.T. Zimanyi, AIP Adv. 6 (2016) 056029.

[19] X. Tang, H. Sepehri-Amin, T. Ohkubo, M. Yano, M. Ito, A. Kato, N. Sakuma, T. Shoji, T. Schrefl, K. Hono, Acta Mater. (2017).

[20] A. Alam, M. Khan, R.W. McCallum, D.D. Johnson, Appl. Phys. Lett. 102 (2013) 042402.

[21] M.A. Susner, B.S. Conner, B.I. Saparov, M.A. McGuire, E.J. Crumlin, G.M. Veith, H. Cao, K.V. Shanavas, D.S. Parker, B.C. Chakoumakos, B.C. Sales, J. Magn. Magn. Mater. 434 (2017) 1–9.

[22] X. Tang, H. Sepehri-Amin, T. Ohkubo, K. Hioki, A. Hattori, K. Hono, Acta Mater. 123 (2017) 1–10.

[23] J. Liu, H. Sepehri-Amin, T. Ohkubo, K. Hioki, A. Hattori, K. Hono, J. Appl. Phys. 115 (2014) 17A744.

[24] T.W. Capehart, R.K. Mishra, G.P. Meisner, C.D. Fuerst, J.F. Herbst, Appl. Phys. Lett. 63 (1993) 3642–3644.

Summary and Future work

7.1 Summary

Hot-deformed magnets prepared from melt-spun Nd-Fe-B ribbon have drawn considerable interests, because of much smaller grain size as compared to that of sintered magnets. Hence, hot-deformed magnets have greater potential to achieve higher coercivity as compared to sintered magnets. However, the magnetic properties are not as high as expected, indicating that there is room to further optimize the processing conditions. This thesis contains optimization of processing conditions and composition of melt-spun ribbons to achieve high magnetic performance in hot-deformed magnets, and then focuses on fabrication of low-cost $RE_2Fe_{14}B$ magnets, whose magnetic properties are comparable to those of $Nd_2Fe_{14}B$ counterparts.

In chapter 3, the enhanced coercivity of hot-deformed magnets by processing from amorphous precursors is reported. The amorphous and nanocrystalline melt-spun ribbons were prepared from different wheel speeds during melt-spinning process. The coercivity in hot-deformed magnets can be enhanced from 1.28 T to 1.40 T by processing from amorphous precursors, while keep the remanent magnetization at same value (1.42 T). These magnetic properties are superior to those of commercial N50 sintered magnets. Detailed microstructure characterization showed that coarse grains could be obtained in hot-pressed magnets processed from amorphous powders, because of small number density of nucleus in the amorphous melt-spun precursors. The coarse grains in hot-pressed magnets lead to larger grains with smaller aspect ratio and smaller areal fraction of grain boundaries in hot-deformed magnets processed from amorphous melt-spun ribbons. As a result, the enhanced concentration of Nd was found in *c*-plane and *ab*-plane grain boundaries because of smaller areal fraction of grain boundaries in hot-deformed magnets processed from amorphous ribbons, which results in stronger pinning force against reversed magnetic domains and higher coercivity can be yielded in hot-deformed magnets processed from amorphous precursors. This work has successfully demonstrated a simple method to achieve higher coercivity in hot-deformed magnets without sacrificing remanent magnetization.

Chapter 4 reported on suppression of non-oriented grains at ribbons surface by trace doping of Nb, in which the role of Nb in refining the microstructure has been studied. In the typical microstructure of the hot-deformed magnets, coarse non-oriented grains (surface crystallites) always appear at the interface of stacked ribbons, which causes reduced remanent magnetization and lower nucleation field. In this chapter, it has been successfully demonstrated that the non-textured grain in the interface of ribbon has been suppressed significantly by trace doping of Nb. As a result, a very high remanent magnetization of ~1.54 T could be achieved in as-deformed magnets. The other merit of Nb-doped sample is smaller grain size (around 250 nm) with small aspect ratio, which recommends it as a competent starting sampler for grain boundary diffusion to achieve high-coercivity in diffusion processed hot-deformed magnets with ultra-fine grained structure.

To develop low-cost high performance Ce-substituted hot-deformed magnets, the fundamental research on Ce-containing hot-deformed magnets was carried out in Chapter 5. In this work, the as-deformed Ce-Fe-B magnets were fabricated followed by grain boundary diffusion of Nd-Cu. After 10wt.% Nd-Cu infiltration, the coercivity of the hot-deformed sample was enhanced substantially from ~8 $\times 10^{-4}$T to ~0.5 T. With increasing the amount of the infiltration of Nd-Cu to 40 wt.%, the coercivity was marginally improved to ~0.7 T. Further compositional analysis on grain boundary phase showed that the total rare earth content in the thin grain boundary phases of the sample infiltrated with 40 wt.% Nd-Cu is 38.1 at.% for *c*-plane and 26.2 at.% for *ab*-plane grain boundary phase, respectively. It suggests that grain boundary phases are likely to be ferromagnetic one even after 40 wt.% Nd-Cu infiltration. The micromagnetic simulation indicates that coercivity can not be remarkably enhanced by formation core-shell structure in 2:14:1 phase when grain boundary phase are ferromagnetic, which explains that coercivity is only increased by 0.2 T even after further increasing Nd-Cu diffusion to 40 wt.%. This work has demonstrated that the non-ferromagnetic grain boundary phase is essential for development of high-coercivity Ce-containing sample.

Based on fundamental research on Ce-containing low-cost $RE_2Fe_{14}B$ carried out in Chapter 5, Chapter 6 reported that fabrication of high performance low cost Ce-substituted Nd-Fe-B hot-deformed magnets, in which magnetic properties of 10 at.% Ce-substituted Nd-(Fe,Co)-B magnet are superior to those of Nd-(Fe,Co)-B has successfully demonstrated. Besides, the role of Co will be investigated as well. In Ce-substituted Nd-(Fe,Co)-B hot-deformed magnets, the coerciviy and

remanent magnetization can be simultaneously increased to ~1.45 T and ~1.50 T, respectively. Further microstructure characterization showed that the grain size and chemical compositions in Ce-free and 10 at.% Ce-substituted hot-deformed magnets are comparable with each other, indicating the enhancement in magnetic properties are resulted from enhanced intrinsic properties. To understand the role of Co, the Co-free hot-deformed samples were also produced. By comparing the Co-free and Co-doped 10 at.% Ce-substituted hot-deformed magnets, the Co was found as role in keeping microstructure intactly. In this work, the potential of replacing Nd by Ce has been exploited by producing high performance Ce-substituted hot-deformed magnets.

7.2 Future work

Followed by summary of this thesis detailed as above, the future work is proposed for several aspects. The magnetic simulations has revealed the coercivity can not be enhanced to above ~ 2.5 T in Nd-Cu diffusion-processed Nd-Fe-B hot-deformed magnets because of ferromagnetic (high concentration of Fe) side-plane grain boundary phase, which was possibly resulted from anisotropic shape (large aspect ratio) of 2:14:1 grains. In the Nb-doped sample, the grain size and aspect ratio could be reduced and the concentration of Fe in side-plane grain boundary phases can be lowered as compared to Nb-free sample, implying that applying the grain boundary diffusion of Nd-Cu on Nb-doped hot-deformed magnets could further reduce Fe concentration in side-plan grain boundary while keeping the same aspect ratio of grains. Therefore, future work will focus on applying diffusion process on Nb-doped hot-deformed magnets to achieve high coercivity and high energy density of Nd-Fe-B hot-deformed magnets.

The other work need to be done is to further reduce the cost of RE-Fe-B magnets while keeping comparable magnetic properties. It is reported that La is likely to enter into the intergranular phase rather than 2:14:1 phase, indicating that the anisotropy field of 2:14:1 phase could be well preserved and exchange decoupling could be strengthened with enrichment of La in grain boundary phase, this would improve the coercivity. Hence, La-substituted Nd-Fe-B or NdCe-Fe-B hot-deformed magnets will be produced to study influence of La on magnetic properties and microstructure.

Acknowledgements

First of all, I would like to acknowledge my supervisor, Prof. Kazuhiro Hono, for accepting me as his PhD student of joint program of University of Tsukuba and National Institute for Materials Science. I am really appreciated for his advice, support and help.

I respect and thank the committee members of my thesis defense: Prof. S. Mitani, Prof. Yanagiha and Prof. S. Takashi.

I would like to express my special thanks of gratitude to Dr. Tadakatsu Ohkubo, Dr. T. Sasaki for the training of facilities, fruitful discussion. I heartily thank Dr. Sepehri Amin Hossein for giving me a lot of constructive suggestion on my experiments and helped me a lot in finalizing PhD project.

I would also acknowledge the members of Nanostructure Analysis Group for the fruitful discussion and friendly interaction.

I am also indebted to my friends, who always encourage me when I felt frustrated and stressed.

I owe my deep gratitude to my wife, Wenting He, for sharing the stress and happiness with me. My sincere acknowledgement is also extended to my parents, for their any supports and sacrifices.

I also acknowledge my collaborators from Daido Special Steel and Research Department of Toyota Company.

Finally, I am thankful to the financial supports during my PhD candidateship from Junior Assistantship Program of National Institute for Materials Sciences and Japan Society for the Promotion of Science.

Publications

1. Xin Tang, H. Sepehri-Amin, T. Ohkubo, K. Hioki, A. Hattori and K. Hono, “Coercivities of hot-deformed magnets processed from amorphous and nanocrystalline precursors”, Acta Materialia. vol. 123, pp. 1-10, January 2017.

2. Xin Tang, H. Sepehri-Amin, T. Ohkubo, M. Yano, M. Ito, A. Kato, N. Sakuma, T. Schrefl and K. Hono, “Coercivity enhancement of hot-deformed Ce-Fe-B magnets by grain boundary infiltration of Nd-Cu eutectic alloy”, Acta Materialia, vol. 144, pp. 884-895, February 2018.

3. Xin Tang, H. Sepehri-Amin, T. Ohkubo and K. Hono, “Suppression of non-oriented grains in Nd-Fe-B hot-deformed magnets by Nb” Scripta Materialia. Accepted.